



Shortcuts to adiabaticity and heat transport in trapped ions

Miguel Ángel Simón Martínez

Supervisors:

Prof. Juan Gonzalo Muga Francisco

Prof. María Luisa Pons Barba

Departamento de Química-Física
Facultad de Ciencia y Tecnología
Universidad del País Vasco/Euskal Herriko Unibertsitatea
(UPV/EHU)

Leioa, Febrero 2021

“Insert deep/meaningful/clever quote by someone who you admire or hate”

Someone who you admire or hate

Acknowledgements

Do not forget about the people that has been by your side and supported you.

Esta Tesis ha sido financiada a través de una beca predoctoral concedida por el Gobierno Vasco/Eusko Jaurlaritza

Contents

Acknowledgements	v
List of Figures	xi
List of publications	xix
Introduction	1
1 Asymmetric scattering with NH Potential	3
1.1 Introduction	4
1.2 Generalized symmetries	6
1.3 Designing potentials for asymmetric devices	10
1.4 Extending the scattering asymmetry to a broad incident-momentum domain	13
1.5 Discussion	14
2 Symmetries and Invariants for Non-Hermitian Hamiltonians	17
2.1 Introduction	18
2.2 Dual character of H and H^\dagger	19
2.3 Time evolution for normalized states.	20
2.3.1 Expectation Values	21
2.3.2 Lower Bound on the Norm of the Wave Function	21
2.4 Generic symmetries	22
2.5 Example of physical relevance of the relations $AH = HA$ or $AH = H^\dagger A$ as symmetries	23
2.6 Discussion	25
3 Real Eigenvalues of complex potentials	27
3.1 Introduction	28
3.2 Hamiltonian Symmetries	30
3.2.1 Basic concepts and terminology	30
3.2.2 Superoperator formalism	33
3.3 S-matrix pole structure	35
3.4 Separable Potentials	37
3.4.1 Time-reversal symmetric potential	38
3.4.2 Parity pseudohermitian potential	40

3.5	Conclusion	41
.1	Review of scattering theory formalism	42
.2	Alternative formulation of A -pseudohermitian symmetries as ordinary (commuting) symmetries	46
.2.1	Pseudohermicity with linear operators	47
.2.2	Pseudohermicity with antilinear operators	49
.2.2.1	PT Symmetry	50
.2.2.2	Time-Reversal Symmetry	51
.3	Properties of separable potentials	52
.3.1	Transition operator	52
.3.2	S -matrix eigenvalues	52
.3.3	Uniqueness of bound state	53
A	Local rectification of heat flux	59
A.1	Introduction	60
A.2	Homogeneous one-dimensional chain	61
A.3	Impurity-based thermal rectifier	65
A.4	Discussion	66
B	Chain of Ions	71
B.1	Introduction	72
B.2	Physical System	74
B.3	Calculation of the stationary heat currents	76
B.3.1	Algebraic, small-oscillations approach to calculate the steady state	78
B.4	Numerical Results	80
B.4.1	Evolution to steady state	81
B.4.2	Rectification in frequency graded chains	82
B.4.3	Same bath temperatures, different bath couplings	83
B.4.4	Dependence with ion number	83
B.4.5	Graded versus segmented	84
B.5	Summary and discussion	84
C	Rectification in a toy model	93
C.1	Introduction	94
C.2	Physical Model	95
C.3	Covariance matrix in the steady state	97
C.4	Solutions	99
C.5	Relation of the Model to a trapped ion set-up	101
C.5.1	Collective trap	101
C.5.2	Individual on-site traps	102
C.5.3	Optical molasses and Langevin baths	103
C.6	Looking for rectification	104
C.6.1	Parametric exploration	106
C.6.2	Spectral match/mismatch approach to rectification	108
C.7	Conclusions	111
C.8	acknowledgements	112

.1	Full set of steady-state equations for the components of $\mathbb{C}^{s,s}$	113
.2	Complete expressions for the Spectral Density Matrix	113
Conclusions		115
 A Interaction versus asymmetry for adiabatic following		 119
Bibliography		121

List of Figures

- 1.1 (Color online) Devices with asymmetric scattering (limited to scattering coefficients being 0 or 1). The dashed and continuous lines represent respectively zero or one for the moduli of the scattering amplitudes; the bended lines are for reflection amplitudes, and the straight lines for transmission: (a) One-way mirror ($\mathcal{T}\mathcal{R}/\mathcal{A}$); (b) One-way barrier (\mathcal{T}/\mathcal{R}); (c) One-Way T-filter (\mathcal{T}/\mathcal{A}); (d) Mirror & 1-way transmitter ($\mathcal{T}\mathcal{R}/\mathcal{R}$); (e) One-way R-filter (\mathcal{R}/\mathcal{A}); (f) Transparent, one-way reflector ($\mathcal{T}\mathcal{R}/\mathcal{T}$). The letter codes summarize the effect of left and right incidence, separated by a slash “/”. \mathcal{T} or \mathcal{R} on one side of the slash indicate a unit transmission or reflection coefficient for incidence from that side, whereas the absence of one or the other letter corresponds to zero coefficients. An \mathcal{A} denotes “full absorption”, i.e., both moduli of reflection and transmission amplitudes are zero for incidence from one side. For example, $\mathcal{T}\mathcal{R}/\mathcal{A}$ means unit modulus transmission and reflection from the left and total absorption from the right.

1.2 (Color online) One-way T-filter (\mathcal{T}/\mathcal{A} , $|T^l| = 1, T^r = R^l = R^r = 0$) with potential $V(x, y) = |V(x, y)|e^{i\phi(x, y)}$ set for $k_0 = 1/d$. (a) Absolute value $|V(x, y)|$; (b) Argument $\phi(x, y)$; (c) Transmission and reflection coefficients: $|R^l|^2$ (black, solid line), $|T^l|^2$ (green, solid line), $|R^r|^2$ (blue, tick, dashed line), $|T^r|^2$ (red, dotted line). $V_0 = \hbar^2/(2md^3)$

1.3 (Color online) Transparent 1-way reflector with a local PT potential: (a) Approximation of the potential (1.8), real part (green solid line), imaginary part (blue dashed line). (b,c) Transmission and reflection coefficients versus momentum kd ; left incidence: $|R^l|^2$ (black, solid line), $|T^l|^2$ (green, solid line); right incidence: $|R^r|^2$ (blue, tick, dashed line), $|T^r|^2$ (red, dotted line, coincides with green, solid line). $\epsilon/d = 10^{-4}$. (b) $\alpha = 1.0\hbar^2/(4\pi m)$ (c) $\alpha = 1.225\hbar^2/(4\pi m)$ (the black, solid line coincides here mostly with the red, dotted and green, solid lines).

3.1	Example of configuration of poles (filled circles) and zeros (empty circles) of the S -matrix eigenvalues in the complex momentum plane for hermitian Hamiltonians. Poles in the upper half plane ($\text{Im}(p) > 0$) correspond to bound eigenstates of the Hamiltonian, i.e. localized states with negative energy. Poles in the lower half plane correspond to virtual states ($\text{Re}(p) = 0$), resonances ($\text{Re}(p) > 0$) and antiresonances ($\text{Re}(p) < 0$). The singularities with negative imaginary part correspond to states that do not belong to the Hilbert space since they are not normalizable. However, they can produce observable effects in the scattering amplitudes, in particular when they approach the real axis. The pole structure of symmetries IV, V, and VII, see Table I, is similar, but pole pairs are also possible in the upper half-plane.	30
3.2	(Color online) Poles and pole trajectories of time-reversal symmetric potential (3.24) for (a) varying V_0 with $a = 2b$; (b) varying a with $b = 0.5 p_0$, $V_0 > 0$; and (c) varying b with $a = p_0$, $V_0 > 0$. At pole collisions we connect each of the incoming trajectories with a different emerging trajectory but the choice of outgoing branch is arbitrary since the two colliding poles lose their identity.	54
3.3	(Color online) Transmission and reflection coefficients of the time-reversal symmetric potential (3.24) with $a = p_0$, $b = 0.5 p_0$ and $V_0 > 0$	55
3.4	(Color online) Poles and pole trajectories for the parity pseudohermitian potential (3.28) (a) varying V_0 with $a = b$; (b) varying a with $b = p_0$, $V_0 > 0$; (c) varying b with $a = 0.5 p_0$, $V_0 > 0$	56
3.5	(Color online) Transmission and reflection coefficients for $a = b = 0.5 p_0$ and $V_0 > 0$	57
A.1	(Color online) (a) On-site potentials: harmonic potential centered at the equilibrium position of each atom (dashed blue line) as a function of the displacement from this position $x_i = y_i - y_{i0}$ in a -units, and the on-site potential for the impurity, $i = N/2 + 1$ (N even, red solid line). (b) Interaction potentials as a function of the distance between nearest neighbors: Morse potential (blue dashed line) valid for all atoms except for $i = N/2 + 1$, N even, where the modified potential (red solid line) is used. The harmonic approximation of the Morse potential is also depicted (eq. (A.5), black dots, only used for fig. 5, below). Parameters: $D = 0.5$, $g = 1$, $\gamma = 45$, $d = 100$ and $b = 105$, used throughout the paper.	63
A.2	(Color online) Symmetric temperature profiles for a homogeneous chain, without impurity. For $T_h = T_L$, $T_c = T_R$ (red solid dots) the (absolute value of) the heat flux is $J_{L \rightarrow R}$, equal to $J_{R \rightarrow L}$ for the reverse configuration of the bath temperatures, $T_h = T_R$, $T_c = T_L$ (black empty squares). Parameters as in fig. 1.	63

A.3 (Color online) Temperature profile along the homogeneous chain for different number of atoms: 100 (dotted black line), 125 (dashed blue line) and 150 (solid red line). The atom sites have been rescaled with the total number of atoms. The time averages have been carried over a time interval of $\approx 2 \times 10^6$ after a transient of $\approx 1 \times 10^5$. In the inset (a), the product JN vs. N demonstrates that for long chains JN is independent of N . In (b) the linear dependence of J with ΔT for a fixed number of atoms, $N = 100$, is shown. Parameters as in fig. 1.	65
A.4 (Color online) Temperature profile for the chain of $N = 20$ atoms, with an impurity in the $N/2+1$ position, with $T_L = T_h$ and $T_R = T_c$ (circles) and with the thermostat baths switched (squares). Parameters as in fig. 1. (a) $T_c = 0.15$, $T_h = 0.2$. $J_{L \rightarrow R} = 0.00769$ vs $J_{R \rightarrow L} = 0.00581$, with gives a rectification $R = 31\%$; (b) $T_c = 0.025$, $T_h = 0.325$. $J_{L \rightarrow R} = 0.0499$ vs $J_{R \rightarrow L} = 0.0140$, with $R = 256\%$	67
A.5 (Color online) Rectification factor R as a function of the temperature difference between ends of the chain of atoms, ΔT . We have changed both T_h and T_c according to $T_c = 0.15 - (\Delta T - 0.05)/2$ and $T_h = 0.2 + (\Delta T - 0.05)/2$, with $N = 20$, keeping the rest of parameters as in fig. A.1. Interatomic potentials: Morse potential, eq. (A.4) (black line with circles, see the temperature profiles of extreme points in fig. 4); harmonic potential, eq. (A.5) (red line with squares).	67
A.6 (Color online) Temperature profile for a harmonic interacting chain of $N = 20$ atoms, with an impurity in the $N/2 + 1$ position, with $T_L = T_h$ and $T_R = T_c$ (circles) and with the thermostat baths switched (squares), for (a) $\Delta T = 0.05$ and (b) $\Delta T = 0.3$. The corresponding rectification factors are (a) $R = 18\%$ and (b) $R = 85\%$. Parameters regarding the impurity are the same as in fig. 1.	69
B.1 Schematic representation of the frequency-graded chain of trapped ions proposed as a thermal rectifier. The left and right ends of the chain are in contact with optical molasses at temperatures T_L and T_R (green and grey boxes respectively). Each ion is in an individual trap. The (angular) frequencies of the traps increase homogeneously from left to right, starting from ω_1 and ending at $\omega_1 + \Delta\omega$. The ions interact through the Coulomb force, which is long range, and therefore all the ions interact among them, even distant neighbors. By default we use 15 ions.	72

B.2 (a) Temperatures of the ions in the stationary state for a graded chain with the parameters described in section B.4.1. The temperature profiles found with the algebraic method (Eq. (B.17)) are indistinguishable from the ones found solving the Langevin equation (Eq. (B.3)). Empty triangles (squares) correspond to $T_L = T_H$ ($T_L = T_C$) and $T_R = T_C$ ($T_R = T_H$). (b) Heat currents as a function of time for $T_L = T_H$ and $T_R = T_C$, see Eq. (B.9): $J_L(t)$ (solid green line) from the left reservoir into the chain; $J_R(t)$ (dotted grey line) from the right reservoir into the chain (negative except at very short times); $J_L(t) + J_R(t)$ (dotted-dashed black line), which must go to zero in the steady state. The three lines tend to stationary values marked by horizontal lines. Parameters: $\omega_1 = 2\pi \times 50$ kHz, $a = 50 \mu\text{m}$, $\delta_H = -0.02 \Gamma$, and $\delta_C = -0.1 \Gamma$, which gives temperatures $T_H \approx 12$ mK and $T_C \approx 3$ mK. $\Delta\omega = 0.5 \omega_1$. In all figures $\Gamma = 2\pi \times 41.3$ MHz.	86
B.3 Graded chain of $N = 15$ $^{24}\text{Mg}^+$ ions. (a) Stationary fluxes for different frequency increments: J_\rightarrow (for $T_L = T_H$ and $T_R = T_C$, dashed line); J_\leftarrow (for $T_L = T_C$ and $T_R = T_H$, solid line) (b) Rectification factor. Parameters: $\omega_1 = 2\pi \times 1$ MHz, $l = 5.25 \mu\text{m}$, $a = 4.76 l$ ($25 \mu\text{m}$), $\delta_H = -0.02 \Gamma$, and $\delta_C = -0.1 \Gamma$	87
B.4 Rectification factor in a graded chain of $N = 15$ $^{24}\text{Mg}^+$ ions for different trap distances and frequency increment. The dashed lines are for $R = 0$ and delimit the regions $J_\rightarrow > J_\leftarrow$ and $J_\rightarrow < J_\leftarrow$. The parameters are $\omega_1 = 2\pi \times 1$ MHz, $l = 5.25 \mu\text{m}$, $\delta_H = -0.02 \Gamma$, and $\delta_C = -0.1 \Gamma$	88
B.5 (a) Friction coefficient defined in Eq. (B.4). (b) Bath temperature defined in Eq. (B.5). (c) Rectification as a function of the temperature difference between the hot and cold baths $T_H - T_C$ for δ_H below (dashed black line) and above (solid blue line) the Doppler limit, and $\delta_C = \delta_D$ (Doppler limit). Parameters: $\omega_1 = 2\pi \times 1$ MHz, $\Delta\omega = 0.15 \omega_1$, $l = 5.25 \mu\text{m}$, $a = 4.76 l$	89
B.6 Rectification factor for different bath temperature differences ΔT as the number of ions is increased. The detuning of the cold bath laser is set to the Doppler limit $\delta_C = -\Gamma/2$. $\omega_1 = 2\pi \times 1$ MHz, $\Delta\omega = 0.15 \omega_1$, $l = 5.25 \mu\text{m}$, $a = 4.76 l$	90
B.7 Comparison of graded and segmented chains with $N = 15$ $^{24}\text{Mg}^+$ ions. (a) Maximum of J_\rightarrow and J_\leftarrow for the graded and segmented chain for different frequency increments. (b) Rectification factor: graded chain (dashed lines); segmented chain (solid lines). Parameters: $\omega_1 = 2\pi \times 1$ MHz, $l = 5.25 \mu\text{m}$, $a = 4.76 l$, $\delta_H = -0.02 \Gamma$, and $\delta_C = -0.1 \Gamma$	91
B.8 Thermal conductivity through the chain for $T_L > T_R$ (empty squares), and $T_L < T_R$ (filled triangles). $\omega_1 = 2\pi \times 1$ MHz, $\Delta\omega = 0.15 \omega_1$, $l = 5.25 \mu\text{m}$, $a = 4.76 l$, $\delta_H = -0.02 \Gamma$ and $\delta_C = -0.1 \Gamma$	92

C.1	Diagram of the model described in Section C.2. Two ions coupled to each other through a spring constant k . Each ion is harmonically trapped and connected to a bath characterized by its temperature T_i and its friction coefficient γ_i .	95
C.2	Rectification, R , in the $k_L k_R$ plane for $k = 1.17 \times 10^{-22}$ fN/m, $\gamma_L = 6.75 \times 10^{-22}$ kg/s, and $\gamma_R = 4.64\gamma_L$.	105
C.3	Rectification factor, R , given by Eq. (C.32).	108
C.4	Rectification for different values of $c = m_2/m_1 = \gamma_R/\gamma_L$ when the maximum condition in the $k_L k_R$ plane is satisfied (Eq. (C.31)).	109
C.5	Spectral densities of the velocities of the ions (r_3 and r_4) corresponding to different values of c in Fig. C.4: (a), (b) for $c = 1$ and (c), (d) for $c = 10$. Solid, black lines correspond to the left ion velocity spectral density $\mathbb{S}_{3,3}(\omega)$ and dashed, blue lines correspond to the right ion velocity spectral density $\mathbb{S}_{4,4}(\omega)$. (a) and (b) correspond to $R = 0$: the overlap between the phonon bands is the same in the forward and reversed configurations. (c) and (d) correspond to $R \approx 0.8$: in the forward configuration (c) the phonons match better than in the reversed configuration (d).	110

dedicatory here

List of publications

I) The results of this Thesis are based on the following articles

Published Articles

1. M. Pons, Y. Y. Cui, A. Ruschhaupt, **M. A. Simón** and J. G. Muga
Local rectification of heat flux
[EPL 119, 64001 \(2017\)](#).
2. A. Ruschhaupt, T. Dowdall, **M. A. Simón** and J. G. Muga
Asymmetric scattering by non-Hermitian potentials
[EPL 120, 20001 \(2017\)](#).
3. **M. A. Simón**, A. Buendía and J. G. Muga
Symmetries and Invariants for Non-Hermitian Hamiltonians
[Mathematics 6, 111 \(2018\)](#).
4. **M. A. Simón**, A. Buendía, A. Kiely, A. Mostafazadeh and J. G. Muga
S-matrix pole symmetries for non-Hermitian scattering Hamiltonians
[Phys. Rev. A 99, 052110 \(2019\)](#).
5. **M. A. Simón**, S. Martínez-Garaot, M. Pons and J. G. Muga
Asymmetric heat transport in ion crystals
[Phys. Rev. E 100, 032109 \(2019\)](#).
6. A. Alaña, S. Martínez-Garaot, **M. A. Simón** and J. G. Muga
Symmetries of ($N \times N$) non-Hermitian Hamiltonian matrices
[J. Phys. A: Math. Theor. 53, 135304 \(2020\)](#).

Preprints

1. A. Ruschhaupt, A. Kiely, **M. A. Simón** and J. G. Muga
Quantum-optical implementation of non-Hermitian potentials for asymmetric scattering
[arXiv:2008.01702 \[quant-ph\]](#) (2020)
(Accepted for publication in Phys. Rev. A)
2. **M. A. Simón**, A. Alaña, M. Pons, A. Ruiz-García and J. G. Muga
Heat rectification with a minimal model of two harmonic oscillators
[arXiv:2010.10432 \[cond-mat.stat-mech\]](#) (2020)

II) Other articles produced during the Thesis period

Published Articles not included in this Thesis

1. M. Palmero, **M. A. Simón** and D. Poletti
Towards Generation of Cat States in Trapped Ions Set-Ups via FAQUAD Protocols and Dynamical Decoupling
[Entropy 21, 1207](#) (2019)
2. **M. A. Simón**, M. Palmero, S. Martínez-Garaot and J. G. Muga
Trapped-ion Fock-state preparation by potential deformation
[Phys. Rev. Research 2, 023372](#) (2020)

Introduction

Todo fuego que se precie empieza con una pequeña chispa.

Chapter 1

Asymmetric scattering with NH Potential

The scattering of quantum particles by non-hermitian (generally nonlocal) potentials in one dimension may result in asymmetric transmission and/or reflection from left and right incidence. After extending the concept of symmetry for non-hermitian potentials, eight generalized symmetries based on the discrete Klein's four-group (formed by parity, time reversal, their product, and unity) are found. Together with generalized unitarity relations they determine selection rules for the possible and/or forbidden scattering asymmetries. Six basic device types are identified when the scattering coefficients (squared moduli of scattering amplitudes) adopt zero/one values, and transmission and/or reflection are asymmetric. They can pictorially be described as a one-way mirror, a one-way barrier (a Maxwell pressure demon), one-way (transmission or reflection) filters, a mirror with unidirectional transmission, and a transparent, one-way reflector. We design potentials for these devices and also demonstrate that the behavior of the scattering coefficients can be extended to a broad range of incident momenta.

1.1 Introduction

The current interest to develop new quantum technologies is boosting applied and fundamental research on quantum phenomena and on systems with potential applications in logic circuits, metrology, communications or sensors. Robust basic devices performing elementary operations are needed to perform complex tasks when combined in a circuit.

In this paper we investigate the properties of potentials with asymmetric transmission or reflection for a quantum, spinless particle of mass m satisfying a one-dimensional (1D) Schrödinger equation. If we restrict the analysis to transmission and reflection coefficients (squared moduli of the scattering complex amplitudes) being either zero or one, a useful simplification for quantum logic operations, there are six types of asymmetric devices, see fig. 1.1. These devices cannot be constructed with Hermitian potentials. In fact for all device types with transmission asymmetries, which are four of the six possible devices, the potentials have to be also nonlocal. Therefore, nonlocal potentials play a major role in this paper. They appear naturally when applying partitioning techniques under similar conditions to the ones leading to non-hermitian potentials, namely, as effective interactions for a subsystem or component of the full wave-function, even if the interactions for the large system are hermitian and local [1].

Symmetries can be used, similarly to their standard application in atomic physics to determine selection rules for allowed/forbidden transitions, to predict whether a certain potential may or may not lead to asymmetric scattering. The concept of symmetry, however, must be generalized when dealing with non-hermitian potentials.

The theory in this paper is worked out for particles and the Schrödinger equation but it is clearly of relevance for optical devices due to the much exploited analogies and connections between Maxwell's equations and the Schrödinger equation, which were used, e.g., to propose the realization of PT-symmetric potentials in optics [2].

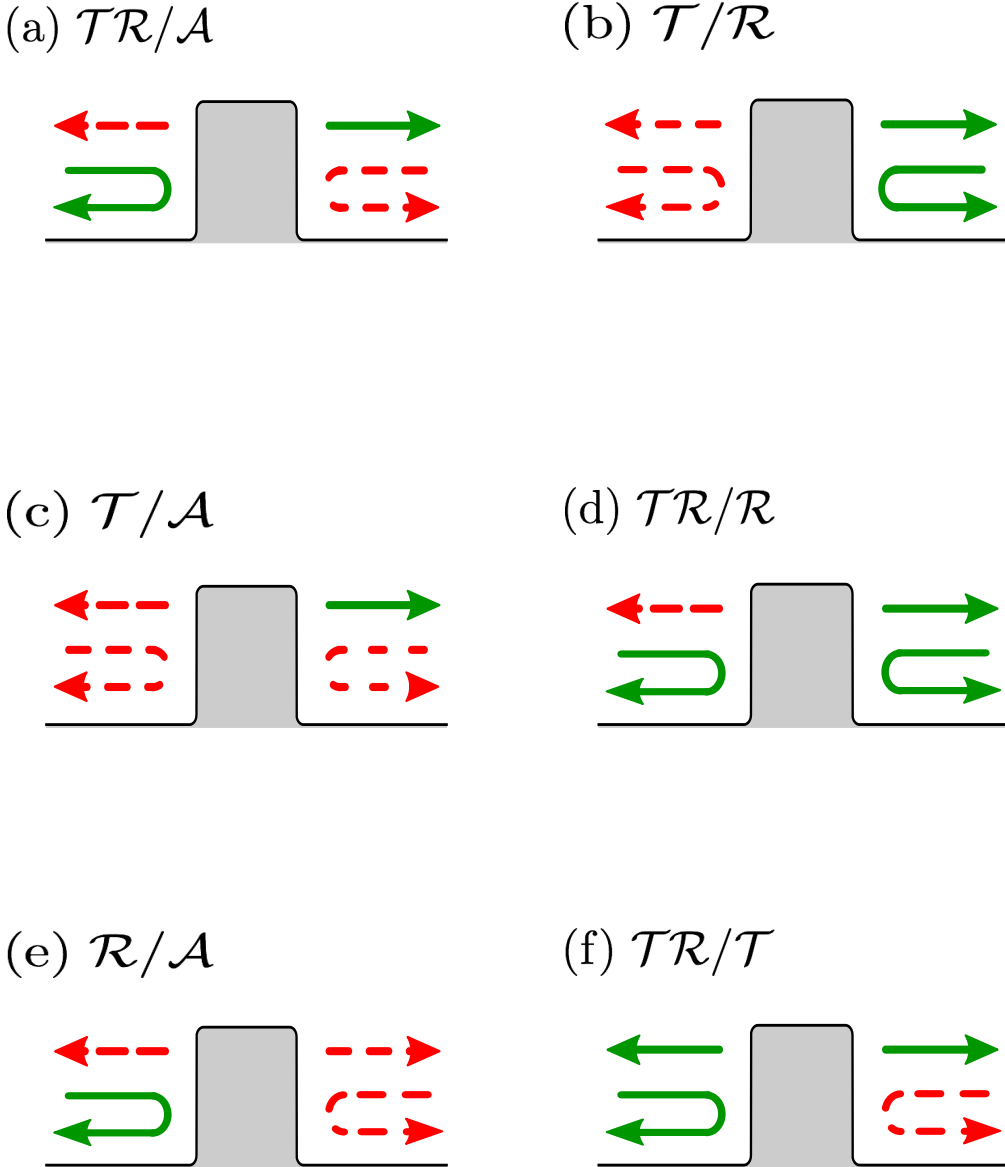


FIGURE 1.1: (Color online) Devices with asymmetric scattering (limited to scattering coefficients being 0 or 1). The dashed and continuous lines represent respectively zero or one for the moduli of the scattering amplitudes; the bended lines are for reflection amplitudes, and the straight lines for transmission: (a) One-way mirror ($\mathcal{T}\mathcal{R}/\mathcal{A}$); (b) One-way barrier (\mathcal{T}/\mathcal{R}); (c) One-Way T-filter (\mathcal{T}/\mathcal{A}); (d) Mirror & 1-way transmitter ($\mathcal{T}\mathcal{R}/\mathcal{R}$); (e) One-way R-filter (\mathcal{R}/\mathcal{A}); (f) Transparent, one-way reflector ($\mathcal{T}\mathcal{R}/\mathcal{T}$). The letter codes summarize the effect of left and right incidence, separated by a slash “/”. \mathcal{T} or \mathcal{R} on one side of the slash indicate a unit transmission or reflection coefficient for incidence from that side, whereas the absence of one or the other letter corresponds to zero coefficients. An \mathcal{A} denotes “full absorption”, i.e., both moduli of reflection and transmission amplitudes are zero for incidence from one side. For example, $\mathcal{T}\mathcal{R}/\mathcal{A}$ means unit modulus transmission and reflection from the left and total absorption from the right.

TABLE 1.1: Symmetries of the potential classified in terms of the commutativity or pseudo-hermiticity of H with the elements of Klein’s 4-group $\{1, \Pi, \theta, \Pi\theta\}$ (second column). The first column sets a simplifying roman-number code for each symmetry. The relations among potential matrix elements are given in coordinate and momentum representations in the third and fourth columns. The fifth column gives the relations they imply in the matrix elements of S and/or \widehat{S} matrices (S is for scattering by H and \widehat{S} for scattering by H^\dagger). From them the next four columns set the relations implied on scattering amplitudes. Together with generalized unitarity relations (1.3) they also imply relations for the moduli (tenth column), and phases (not shown). The last two columns indicate the possibility to achieve perfect asymmetric transmission or reflection: “ P ” means possible (but not necessary), “No” means impossible. In some cases “ P ” is accompanied by a condition that must be satisfied.

Code	Symmetry	$\langle x V y\rangle =$	$\langle p V p'\rangle =$	$\langle p S p'\rangle =$	$T^l =$	$T^r =$	$R^l =$	$R^r =$	from eq. (1.3)	$ T^l =1$ $ T^r =0$
I	$1H = H1$	$\langle x V y\rangle$	$\langle p V p'\rangle$	$\langle p S p'\rangle$	T^l	T^r	R^l	R^r		P
II	$1H = H^\dagger 1$	$\langle y V x\rangle^*$	$\langle p' V p\rangle^*$	$\langle p \widehat{S} p'\rangle$	\widehat{T}^l	\widehat{T}^r	\widehat{R}^l	\widehat{R}^r	$ T^l = T^r , R^l = R^r $	No
III	$\Pi H = H\Pi$	$\langle -x V - y\rangle$	$\langle -p V - p'\rangle$	$\langle -p S - p'\rangle$	T^r	T^l	R^r	R^l	$ T^l = T^r , R^l = R^r $	No
IV	$\Pi H = H^\dagger \Pi$	$\langle -y V - x\rangle^*$	$\langle -p' V - p\rangle^*$	$\langle -p \widehat{S} - p'\rangle$	\widehat{T}^r	\widehat{T}^l	\widehat{R}^r	\widehat{R}^l		$P, R^r R^{l*} = 1$
V	$\Theta H = H\Theta$	$\langle x V y\rangle^*$	$\langle -p V - p'\rangle^*$	$\langle -p' \widehat{S} - p\rangle$	\widehat{T}^r	\widehat{T}^l	\widehat{R}^l	\widehat{R}^r	$ R^l = R^r $	$P, R^{r,l} =1$
VI	$\Theta H = H^\dagger \Theta$	$\langle y V x\rangle$	$\langle -p' V - p\rangle$	$\langle -p' S - p\rangle$	T^r	T^l	R^l	R^r	$ T^l = T^r $	No
VII	$\Theta\Pi H = H\Theta\Pi$	$\langle -x V - y\rangle^*$	$\langle p V p'\rangle^*$	$\langle p' \widehat{S} p\rangle$	\widehat{T}^l	\widehat{T}^r	\widehat{R}^r	\widehat{R}^l	$ T^l = T^r $	No
VIII	$\Theta\Pi H = H^\dagger \Theta\Pi$	$\langle -y V - x\rangle$	$\langle p' V p\rangle$	$\langle p' S p\rangle$	T^l	T^r	R^r	R^l	$ R^l = R^r $	P

1.2 Generalized symmetries

The detailed technical and formal background for the following can be found in a previous review on 1D scattering by complex potentials [1], a companion to this article for those readers willing to reproduce the calculations in detail. The Supplemental Material (Sec. I) provides also a minimal kit of scattering theory formulae that may be read first to set basic concepts and notation. The notation is essentially as in [1], but it proves convenient to use for the potential matrix (or kernel function) in coordinate representation two different forms, namely $\langle x|V|y\rangle = V(x, y)$. “Local” potentials are those for which $V(x, y) = V(x)\delta(x - y)$.

For hermitian Hamiltonians, symmetries are represented by the commutation of a symmetry operator with the Hamiltonian. In scattering theory, symmetry plays an important role as it implies relations among the S-matrix elements beyond those implied by its unitarity, see e.g. [3] and, for scattering in one dimension, Sec. 2.6 in [1].

Symmetries are also useful for non-hermitian Hamiltonians, but the mathematical and conceptual framework must be generalized. We consider that a unitary or antiunitary operator A represents a symmetry of H if it satisfies at least one of

these relations,

$$AH = HA, \quad (1.1)$$

$$AH = H^\dagger A. \quad (1.2)$$

For a right eigenstate of H , $|\psi\rangle$, with eigenvalue E , eq. (1.1) implies that $A|\psi\rangle$ is also a right eigenstate of H , with the same eigenvalue if A is unitary, and with the complex conjugate eigenvalue E^* if A is antiunitary. Equation (1.2) implies that $A|\psi\rangle$ is a right eigenstate of H^\dagger with eigenvalue E for A unitary or E^* for A antiunitary, or a left eigenstate of H with eigenvalue E^* for A unitary, or E for A antiunitary. For real-energy scattering eigenfunctions in the continuum, the ones we are interested in here, $E^* = E$. When eq. (1.2) holds we say that H is A -pseudohermitian [4]. Parity-pseudohermiticity has played an important role as being equivalent to space-time reflection (PT) symmetry for *local* potentials [4, 5]. A large set of these equivalences will be discussed below. A relation of the form (1.2) has been also used with differential operators to get real spectra beyond PT-symmetry for local potentials [6, 7].

Here we consider A to be a member of the Klein 4-group $K_4 = \{1, \Pi, \Theta, \Pi\Theta\}$ formed by unity, the parity operator Π , the antiunitary time-reversal operator Θ , and their product $\Pi\Theta$. This is a discrete, abelian group. We also assume that the Hamiltonian is of the form $H = H_0 + V$, with H_0 , the kinetic energy operator of the particle, being hermitian and satisfying $[H_0, A] = 0$ for all members of the group, whereas the potential V may be non-local in position representation. The motivation to use Klein's group is that the eight relations implied by eqs. (1.1) and (1.2) generate all possible symmetries of a non-local potential due to the identity, complex conjugation, transposition, and sign inversion, both in coordinate or momentum representation, see table 1.1, where each symmetry has been labeled by a roman number. Interesting enough, in this classification hermiticity (symmetry II in table 1.1) may be regarded as 1-pseudohermiticity.

Examples on how to find the relations in the fifth column of table 1.1 of S - and \widehat{S} -matrix elements (for scattering by H and H^\dagger respectively) are provided in ref. [1], where the symmetry types III, VI, and VII were worked out. Similar manipulations, making use of the action of unitary or antiunitary operators of Klein's group on Möller operators, help to complete the table.

TABLE 1.2: Equivalences among symmetries for the potential elements. Given the symmetry of the upper row, the table provides the equivalent symmetries. For example, if II is satisfied, then III=IV holds. In words, if the potential is hermitian, parity symmetry amounts to parity pseudohermiticity. In terms of the matrix elements of the potential, if $\langle x|V|y\rangle = \langle y|V|x\rangle^*$ and also $\langle x|V|y\rangle = \langle -x|V|y\rangle$, $\forall(x,y)$, then $\langle x|V|y\rangle = \langle -y|V|-x\rangle^*$ holds as well. One may proceed similarly for all other relations. The commutation with the identity (I) is excluded as this symmetry is satisfied by all potentials.

II	III	IV	V	VI	VII	VIII
III=IV	II=IV	II=III	II=VI	II=V	II=VIII	II=VII
V=VI	V=VII	V=VIII	III=VII	III=VIII	III=V	III=VI
VII=VIII	VI=VIII	VI=VII	IV=VIII	IV=VII	IV=VI	IV=V

From the fifth column in table 1, equivalences among the amplitudes for left and right incidence for scattering by H , $(T^{l,r}, R^{l,r})$ or H^\dagger ($\hat{T}^{l,r}, \hat{R}^{l,r}$), are deduced, see the Supplemental Material and the four columns for $T^{l,r}$, and $R^{l,r}$ in table 1.1. Together with the generalized unitarity relations $\hat{S}^\dagger S = S\hat{S}^\dagger = 1$, which in terms of amplitudes take the form [1]

$$\begin{aligned} \hat{T}^l T^{l*} + \hat{R}^l R^{l*} &= 1, \\ \hat{T}^r T^{r*} + \hat{R}^r R^{r*} &= 1, \\ \hat{T}^{l*} R^r + T^r \hat{R}^{l*} &= 0, \\ T^l \hat{R}^{r*} + \hat{T}^{r*} R^l &= 0, \end{aligned} \tag{1.3}$$

these equivalences between the amplitudes imply further consequences on the amplitudes' moduli (tenth column of table 1.1) and phases (not shown). The final two columns use the previous results to determine if perfect asymmetry is possible for transmission or reflection. This makes evident that hermiticity (II) and parity (III) preclude, independently, any asymmetry in the scattering coefficients; PT-symmetry (VII) or Θ -pseudohermiticity (VI) forbid transmission asymmetry (all local potentials satisfy automatically symmetry VI), whereas time-reversal symmetry (i.e., a real potential in coordinate space) (V) or PT-pseudohermiticity (VIII) forbid reflection asymmetry. A caveat is that asymmetric effects forbidden by a certain symmetry in the linear (Schrödinger) regime considered in this paper might not be forbidden in a non-linear regime [8], which goes beyond our present scope.

The occurrence of one particular symmetry in the potential (conventionally “first symmetry”) does not exclude a second symmetry to be satisfied as well.

TABLE 1.3: Device types for transmission and/or reflection asymmetry, restricted to 1 or 0 moduli for the scattering amplitudes. The fifth column indicates the symmetries in table 1.1 that forbid the device. Figures S2, S3, S5 and S6 can be found in the supplemental material to this paper.

Device type	Left incidence	Right incidence	Code	Forbidden by
One-way mirror	transmits and reflects	absorbs	$\mathcal{T}\mathcal{R}/\mathcal{A}$	II, III, IV, V, VI, VII, VIII
One-way barrier	transmits	reflects	\mathcal{T}/\mathcal{R}	II, III, IV, V, VI, VII, VIII
One-way T-filter	transmits	absorbs	\mathcal{T}/\mathcal{A}	II, III, IV, V, VI, VII
Mirror&1-way transmitter	transmits and reflects	reflects	$\mathcal{T}\mathcal{R}/\mathcal{R}$	II, III, VI, VII
One-way R-filter	reflects	absorbs	\mathcal{R}/\mathcal{A}	II, III, IV, V, VII, VIII
Transparent 1-way reflector	transmits and reflects	transmits	$\mathcal{T}\mathcal{R}/\mathcal{T}$	II, III, V, VIII

TABLE 1.4: Device types allowed for a given symmetry.

Symmetry	Allowed devices
I	All types
II	None
III	None
IV	$\mathcal{T}\mathcal{R}/\mathcal{R}, \mathcal{T}\mathcal{R}/\mathcal{T}$
V	$\mathcal{T}\mathcal{R}/\mathcal{R}$
VI	$\mathcal{R}/\mathcal{A}, \mathcal{T}\mathcal{R}/\mathcal{T}$
VII	$\mathcal{T}\mathcal{R}/\mathcal{T}$
VIII	$\mathcal{T}/\mathcal{A}, \mathcal{T}\mathcal{R}/\mathcal{R}$

When a double symmetry holds, excluding the identity, the “first” symmetry implies the equivalence of the second symmetry with a third symmetry. We have already mentioned that Π -pseudohermiticity (IV) is equivalent to PT -symmetry (VII) for local potentials. Being local is just one particular way to satisfy symmetry VI, namely Θ -pseudohermiticity. The reader may verify with the aid of the third column for $\langle x|V|y\rangle$ in table 1.1, that indeed, if symmetry VI is satisfied (first symmetry), symmetry IV has the same effect as symmetry VII. They become equivalent. Other well known example is that for a local potential (symmetry VI is satisfied), a real potential in coordinate space is necessarily hermitian, so symmetries V and II become equivalent. These examples are just particular cases of the full set of equivalences given in table 1.2.

Combining the information of the last two-columns in table 1.1 with the additional condition that all scattering coefficients be 0 or 1 we elaborate table 1.3, which provides the symmetries that do not allow the implementation of the devices in fig. 1.1. The complementary table 1.4 gives instead the symmetries that allow, but do not necessarily imply, a given device type. The device denominations in fig. 1.1 or table 1.3 are intended as short and meaningful, and do not necessarily coincide with some extended terminology, in part because the range of possibilities

is broader here than those customarily considered, and because we use a 1 or 0 condition for the moduli. For example, a device with reflection asymmetry and with $T^r = T^l = 1$ would in our case be a particular “transparent, one-way reflector”, as full transmission occurs from both sides. This effect has however become popularized as “unidirectional invisibility” [10, 11]. A debate on terminology is not our main concern here, and the use of a code system as the one proposed will be instrumental in avoiding misunderstandings.

1.3 Designing potentials for asymmetric devices

We will show how to design non-local potentials leading to the asymmetric devices. For simplicity we look for non-local potentials $V(x, y)$ with local support that vanish for $|x| > d$ and $|y| > d$.

Inverse scattering proceeds similarly to [12], by imposing an ansatz for the wavefunctions and the potential in the stationary Schrödinger equation

$$\frac{\hbar^2 k^2}{2m} \psi(x) = -\frac{\hbar^2}{2m} \frac{d^2}{dx^2} \psi(x) + \int_{-d}^d dy V(x, y) \psi(y). \quad (1.4)$$

The free parameters are fixed making use of the boundary conditions. The form of the wavefunction incident from the left is $\psi_l(x) = e^{ikx} + R^l e^{-ikx}$ for $x < -d$ and $\psi_l(x) = T^l e^{ikx}$ for $x > d$, where $k = p/\hbar$. The wavefunction incident from the right is instead $\psi_r(x) = e^{-ikx} T^r$ for $x < -d$ and $\psi_r(x) = e^{-ikx} + R^r e^{ikx}$ for $x > d$.

Our strategy is to assume polynomial forms for the two wavefunctions in the interval $|x| < d$, $\psi_l(x) = \sum_{j=0}^5 c_{l,j} x^j$ and $\psi_r(x) = \sum_{j=0}^5 c_{r,j} x^j$, and also a polynomial ansatz of finite degree for the potential $V(x, y) = \sum_i \sum_j v_{ij} x^i y^j$. Inserting these ansatzes in eq. (1.4) and from the conditions that $\psi_{l,r}$ and their derivatives must be continuous, all coefficients $c_{l,j}$, $c_{r,j}$ and v_{ij} can be determined. Symmetry properties of the potential can also be imposed via additional conditions on the potential coefficients v_{ij} . For example we may use this method to obtain a one-way T-filter (\mathcal{T}/\mathcal{A}) device (third device in table 1.3) with a nonlocal PT-pseudohermitian potential (symmetry VIII of table 1.1) for a chosen wavevector $k = k_0$. The absolute value and argument of the resulting potential $V(x, y)$ are shown in figs. 1.2(a) and 1.2(b) together with its scattering coefficients as function of the incident wave vector, fig. 1.2(c). As can be seen in fig. 1.2(c) the imposed

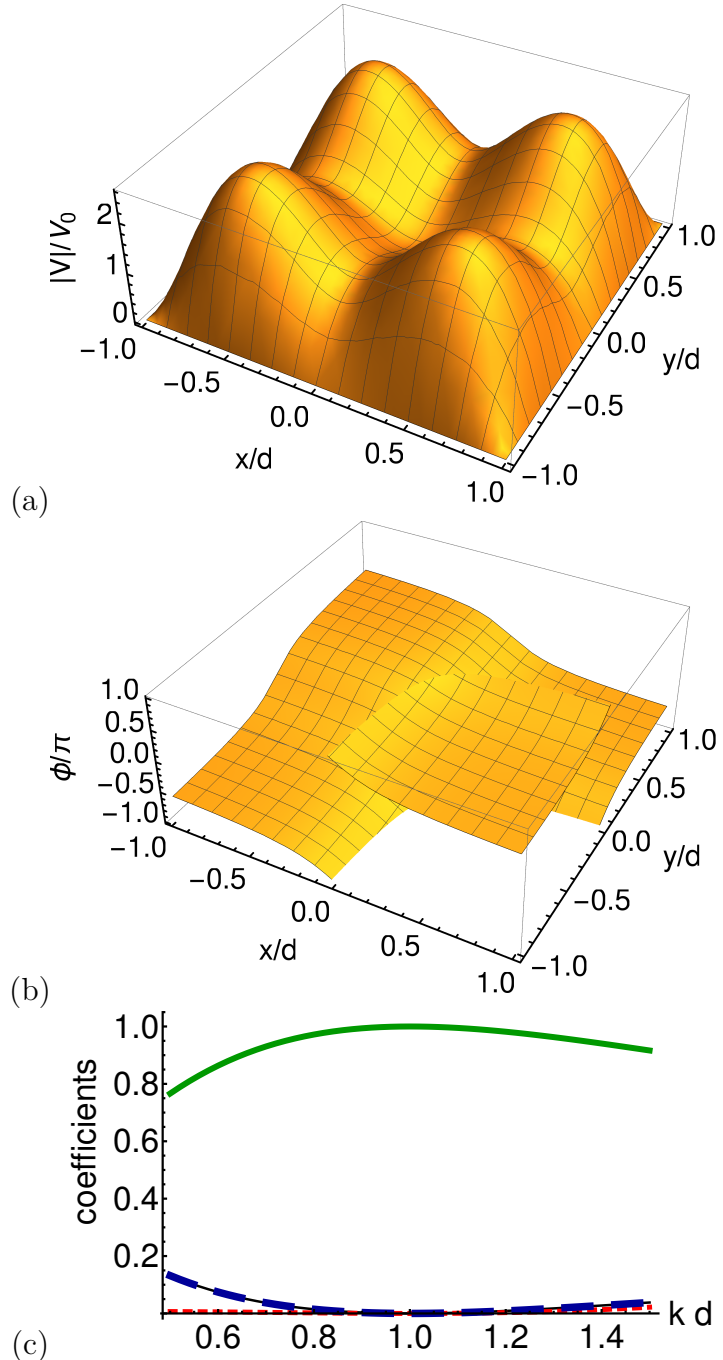


FIGURE 1.2: (Color online) One-way T-filter (\mathcal{T}/\mathcal{A} , $|T^l| = 1, T^r = R^l = R^r = 0$) with potential $V(x, y) = |V(x, y)|e^{i\phi(x, y)}$ set for $k_0 = 1/d$. (a) Absolute value $|V(x, y)|$; (b) Argument $\phi(x, y)$; (c) Transmission and reflection coefficients: $|R^l|^2$ (black, solid line), $|T^l|^2$ (green, solid line), $|R^r|^2$ (blue, tick, dashed line), $|T^r|^2$ (red, dotted line). $V_0 = \hbar^2/(2md^3)$.

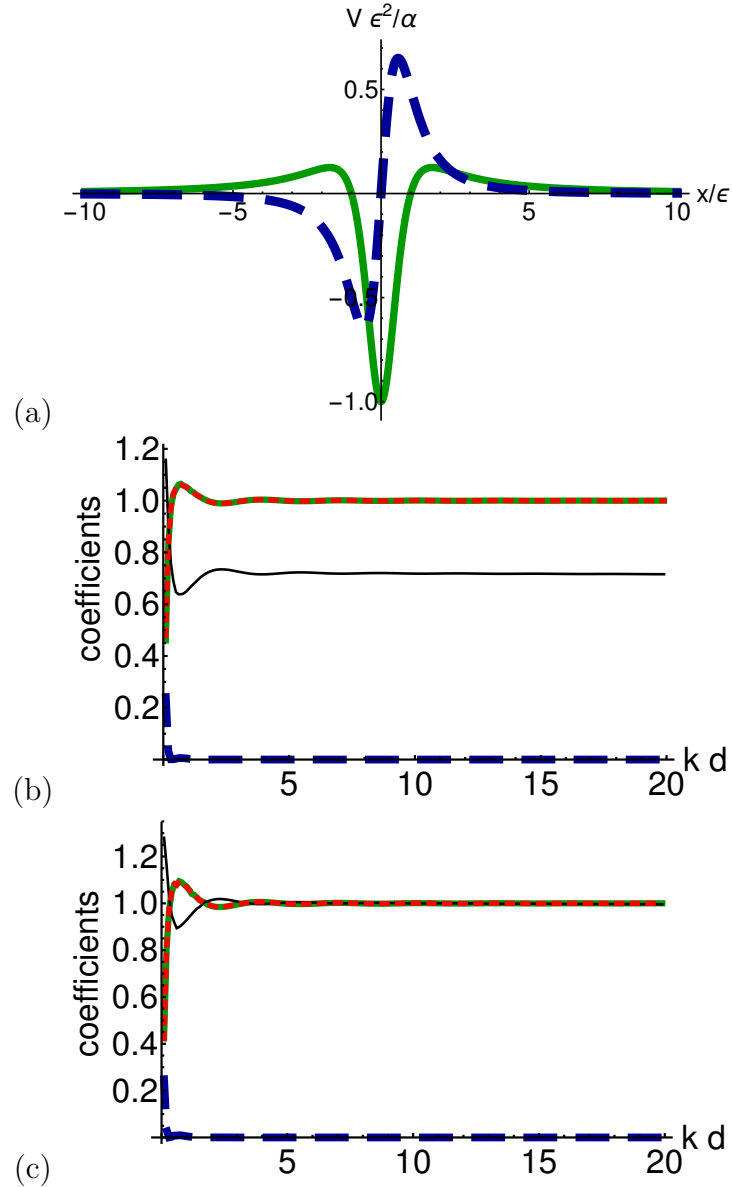


FIGURE 1.3: (Color online) Transparent 1-way reflector with a local PT potential: (a) Approximation of the potential (1.8), real part (green solid line), imaginary part (blue dashed line). (b,c) Transmission and reflection coefficients versus momentum kd ; left incidence: $|R^l|^2$ (black, solid line), $|T^l|^2$ (green, solid line); right incidence: $|R^r|^2$ (blue, tick, dashed line), $|T^r|^2$ (red, dotted line, coincides with green, solid line). $\epsilon/d = 10^{-4}$. (b) $\alpha = 1.0 \hbar^2/(4\pi m)$ (c) $\alpha = 1.225 \hbar^2/(4\pi m)$ (the black, solid line coincides here mostly with the red, dotted and green, solid lines).

scattering coefficients are fulfilled exactly for the chosen wavevector. They are also satisfied approximately in a neighborhood of k_0 . In the Supplemental Material, Sec. II, we give further details about the construction of this potential and we work out other asymmetric devices of fig. 1.1.

1.4 Extending the scattering asymmetry to a broad incident-momentum domain

The inversion technique just described may be generalized to extend the range of incident momenta for which the potential works by imposing additional conditions and increasing correspondingly the number of parameters in the wavefunction ansatz, for example we may impose that the derivatives of the amplitudes, in one or more orders, vanish at k_0 , or 0/1 values for the coefficients not only at k_0 but at a series of grid points k_1, k_2, \dots, k_N , as in [1, 12–14].

Here we put forward instead a method that provides a very broad working-window domain. While we make formally use of the Born approximation, the exact numerical computations demonstrate the robustness and accuracy of the approach to achieve that objective by making use of an adjustable parameter in the potential. The very special role of the Born approximation in inverse problems has been discussed and demonstrated in [15–17]. Specifically we study a transparent one-way reflector $\mathcal{T}\mathcal{R}/\mathcal{T}$. Our aim is now to find a local PT-symmetric potential such that asymmetric reflection results, $T^l = T^r = 1, R^r = 0, |R^l| = 1$ for a broad range of incident momenta. A similar goal was pursued in [18] making use of a supersymmetric transformation, without imposing $|R^l| = 1$.

In the Born approximation and for a local potential $V(x)$, the reflection amplitudes take the simple form

$$R^l = -\frac{2\pi im}{p} \langle -p|V|p\rangle, \quad R^r = -\frac{2\pi im}{p} \langle p|V|-p\rangle. \quad (1.5)$$

Defining the Fourier transform

$$\tilde{V}(k) = \frac{1}{\sqrt{2\pi}} \int_{-\infty}^{\infty} dx V(x) e^{-ikx} \quad (1.6)$$

we get for $k = p/\hbar > 0$:

$$R^l = -\frac{\sqrt{2\pi}im}{k\hbar^2}\tilde{V}(-2k), \quad R^r = -\frac{\sqrt{2\pi}im}{k\hbar^2}\tilde{V}(2k). \quad (1.7)$$

Assuming that the potential is local and PT-symmetrical, we calculate the transition coefficient from them using generalized unitarity as $|T|^2 = 1 - R^{r*}R^l$.

To build a $\mathcal{T}\mathcal{R}/\mathcal{T}$ device we demand: $\tilde{V}(k) = \sqrt{2\pi}\alpha k$ ($k < 0$) and $\tilde{V}(k) = 0$ ($k \geq 0$). By inverse Fourier transformation, this implies

$$\begin{aligned} V(x) &= -\alpha \frac{\partial}{\partial x} \lim_{\epsilon \rightarrow 0} \frac{1}{x - i\epsilon} = \alpha \lim_{\epsilon \rightarrow 0} \frac{1}{(x - i\epsilon)^2} \\ &= \alpha \lim_{\epsilon \rightarrow 0} \left[\frac{x^2 - \epsilon^2}{(x^2 + \epsilon^2)^2} + i \frac{2x\epsilon}{(x^2 + \epsilon^2)^2} \right], \end{aligned} \quad (1.8)$$

which is indeed a local, PT -symmetric potential for α real. α is directly related to the reflection coefficient, within the Born approximation, $R^l = 4\pi im\alpha/\hbar^2$. As the Born approximation may differ from exact results we shall keep α as an adjustable parameter in the following.

In a possible physical implementation, the potential in eq. (1.8) will be approximated by keeping a small finite $\epsilon > 0$, see fig. 1.3(a). Then, its Fourier transform is $\tilde{V}(k) = \sqrt{2\pi}\alpha k e^{\epsilon k}$ ($k < 0$) and $\tilde{V}(k) = 0$ ($k \geq 0$). In figs. 1.3(b) and (c), the resulting coefficients for $\epsilon/d = 10^{-4}$ and two different values of α are shown. These figures have been calculated by numerically solving the Schrödinger equation exactly. Remarkably, the Born approximation contains all the information required to build the required potential shape up to a global factor. Such a prominent role of the Born approximation in inverse problems has been noted in different applications [15–17]. For a range of α , the potential gives $|R^r| \approx 0$, a nearly constant $|R^l|^2$, and $|T^r| = |T^l| \approx 1$ in a broad k -domain, see fig. 1.3(b). Adjusting the value of α , fig. 1.3(c), sets $|R^l| \approx 1$ as desired.

1.5 Discussion

Scattering asymmetries are necessary to develop technologically relevant devices such as one-way mirrors, filters and barriers, invisibility cloaks, diodes, or Maxwell demons. So far much effort has been devoted to build and apply local PT-symmetric potentials but the possible scattering asymmetries with them are

quite limited. We find that six device types with asymmetric scattering are possible when imposing 0 or 1 scattering coefficients. PT-symmetry can only realize one of them, but this symmetry is just one among eight possible symmetries of complex non-local potentials. The eight symmetries arise from the discovery that Klein's four-group $\{1, \Pi, \Theta, \Theta\Pi\}$, combined with two possible relations among the Hamiltonian, its adjoint, and the symmetry operators of the group, eqs. (1) and (2), produce all possible equalities among potential matrix elements after complex conjugation, coordinate inversion, the identity, and transposition. In other words, to have all possible such equalities, the conventional definition of a symmetry A in terms of its commutation with the Hamiltonian H is not enough, and A -pseudohermiticity must be considered as well on the same footing. Extending the concept of what a symmetry is for complex, non-local potentials is a fundamental, far-reaching step of this work. This group theoretical analysis and classification is not only esthetically pleasing, but also of practical importance, as it reveals the underlying structure and span of the possibilities available in principle to manipulate the asymmetrical response of a potential for a structureless particle.

We provide potentials for the different asymmetric devices including an example that works in a broad domain of incident momenta. Although the present theory is for the scattering of quantum particles, the analogies between quantum physics and optics suggest to extend the concepts and results for optical asymmetric devices.

Interesting questions left for future work are the inclusion of other mechanisms for transmission and reflection asymmetries (for example nonlinearities [8, 19], and time dependent potentials [20, 21]), or a full discussion of the phases of the scattering amplitudes in addition to the moduli emphasized here. In this paper the properties of the scattering amplitudes have been worked out assuming that the operator A in the symmetry relations in eqs. (1.1) and (1.2) is a unitary/antiunitary operator in Klein's group. We may generalize the study to include more general operators, possibly including differential operators, as was done in [22] for phase transitions of optical potentials, or the operator that swaps internal states or waveguides [23, 24].

We shall also examine in a complementary paper the physical realization of complex nonlocal effective potentials. In a quantum optics scenario, simple examples were provided in [25] based on applying the partitioning technique [26, 27]

to the scattering of a particle with internal structure. The experimental realization of all new symmetries and devices may be challenging, e.g. to engineer the nonlocality in optics, but there is much to gain. We may expect progress similar to the successful evolution from theory to actual devices in the sequence from the first mathematical models of PT-symmetric potentials [28], to the proposal of an optical realization [2], and to the actual experiments [29], even if considerable time lapses were needed between the three steps.

Chapter 2

Symmetries and Invariants for Non-Hermitian Hamiltonians

We discuss Hamiltonian symmetries and invariants for quantum systems driven by non-Hermitian Hamiltonians. For time-independent Hermitian Hamiltonians, a unitary or antiunitary transformation AHA^\dagger that leaves the Hamiltonian H unchanged represents a symmetry of the Hamiltonian, which implies the commutativity $[H, A] = 0$ and, if A is linear and time-independent, a conservation law, namely the invariance of expectation values of A . For non-Hermitian Hamiltonians, H^\dagger comes into play as a distinct operator that complements H in generalized unitarity relations. The above description of symmetries has to be extended to include also A -pseudohermiticity relations of the form $AH = H^\dagger A$. A superoperator formulation of Hamiltonian symmetries is provided and exemplified for Hamiltonians of a particle moving in one-dimension considering the set of A operators that form Klein's 4-group: parity, time-reversal, parity&time-reversal, and unity. The link between symmetry and conservation laws is discussed and shown to be richer and subtler for non-Hermitian than for Hermitian Hamiltonians.

2.1 Introduction

The intimate link between invariance and symmetry is well studied and understood for Hermitian Hamiltonians but non-Hermitian Hamiltonians pose some interesting conceptual and formal challenges. Non-Hermitian Hamiltonians arise naturally in quantum systems as effective interactions for a subsystem. These Hamiltonians may be proposed phenomenologically or may be found exactly or approximately by applying Feshbach's projection technique to describe the dynamics in the subsystem [25, 26]. It is thus important to understand how common concepts for Hermitian Hamiltonians such as “symmetry”, “invariants”, or “conservation laws” generalize. A lightning review in this section of concepts and formal relations for a time-independent Hermitian Hamiltonian H will be helpful as the starting point to address generalizations for a non-Hermitian H . Unless stated otherwise, H is time-independent in the following. In quantum mechanics A (unitary or antiunitary) represents a symmetry of the Hamiltonian if, together with its adjoint A^\dagger , satisfies

$$A^\dagger H A = H, \quad (2.1)$$

so that

$$[H, A] = 0, \quad (2.2)$$

and thus A , which we assume to be time-independent unless stated otherwise, represents also a conserved quantity when A is unitary (and therefore linear),

$$\langle \psi(t), A\psi(t) \rangle = \langle \psi(0), A\psi(0) \rangle, \quad (2.3)$$

(We use the ordinary quantum inner product notation.) where $|\psi(t)\rangle = U(t)|\psi(0)\rangle$ is the time-dependent wave function satisfying the Schrödinger equation

$$i\hbar\partial_t |\psi(t)\rangle = H |\psi(t)\rangle, \quad (2.4)$$

and $U(t) = e^{-iHt/\hbar}$ is the unitary evolution operator from 0 to t , $U(t)U^\dagger(t) = U^\dagger(t)U(t) = 1$.

Backwards evolution in time from t to 0 is represented by $U(-t) = U(t)^\dagger$ so that the initial state is recovered by a forward and backward sequence, $U(t)^\dagger U(t)|\psi(0)\rangle = |\psi(0)\rangle$.

Equation (2.3) may formally be found for an antiunitary A if $AH = -HA$. However, for antilinear operators expectation values are ambiguous since multiplication of the state by a unit modulus phase factor $e^{i\phi}$ changes the expectation value by $e^{-2i\phi}$. This ambiguity does not mean at all that antilinear symmetries do not have physical consequences. They affect, for example, selection rules for possible transitions.

More generally, time-independent linear operators A satisfying (2.2), fullfill (2.3) without the need to be unitary, and represent also invariant quantities. A further property from (2.2) is that if $|\phi_E\rangle$ is an eigenstate of H with (real) eigenvalue E , then $A|\phi_E\rangle$ is also an eigenstate of H with the same eigenvalue.

2.2 Dual character of H and H^\dagger

For $H \neq H^\dagger$, we find the generalized unitarity relations $U(t)\widehat{U}^\dagger(t) = \widehat{U}^\dagger U(t) = 1$, where $\widehat{U}(t) = e^{-iH^\dagger t/\hbar}$. Backwards evolution with H^\dagger compensates the changes induced forwards by H . Similar generalized unitarity relations exist for the scattering S matrix (for evolution with H) and the corresponding \widehat{S} (for evolution with H^\dagger), with important physical consequences discussed e.g. in [1, 30].

Now consider the following two formal generalizations of the element $\langle\psi(t), A\psi(t)\rangle$ in Equation (2.3),

$$\langle e^{-iH^\dagger t/\hbar}\psi(0), Ae^{-iHt/\hbar}\psi(0)\rangle = \langle \widehat{\psi}(t), A\psi(t)\rangle, \quad (2.5)$$

$$\langle e^{-iHt/\hbar}\psi(0), Ae^{-iH^\dagger t/\hbar}\psi(0)\rangle = \langle \psi(t), A\psi(t)\rangle, \quad (2.6)$$

and the generalizations of (2.2)

$$AH = HA, \quad (2.7)$$

$$AH = H^\dagger A. \quad (2.8)$$

We name (2.8) A -pseudohermiticity of H [4]. (This is here a formal definition that does not presuppose any further property on A .) Up to normalization, which will be discussed in the following section, Equation (2.6) corresponds to the usual rule to define expectation values, whereas (2.5), where $|\widehat{\psi}(t)\rangle \equiv e^{-iH^\dagger t/\hbar}|\psi(0)\rangle$, is unusual, and its physical meaning is not obvious. Note, however, that for linear

$A, AH = HA$ implies the conservation of the unusual quantity (2.5), whereas A -pseudohermiticity $AH = H^\dagger A$ implies the conservation of the usual quantity (2.6) [31, 32], as discussed mostly for local PT-symmetrical potentials with A being the parity operator [19, 33, 34]. At this point we might be tempted to discard (2.7) as less useful or significant physically. This is however premature for several reasons. One is the following (others will be seen in Sections 4 to 6): Unlike Hermitian Hamiltonians, non-Hermitian ones may have generally different right and left eigenvectors. We assume the existence of the resolution

$$H = \sum_j |\phi_j\rangle E_j \langle \hat{\phi}_j|, \quad (2.9)$$

where the E_j may be complex and where

$$H|\phi_j\rangle = E_j|\phi_j\rangle, \quad H^\dagger|\hat{\phi}_j\rangle = E_j^*|\hat{\phi}_j\rangle. \quad (2.10)$$

We have used a simplifying notation for a discrete spectrum, but a continuum part could be treated similarly with integrals rather than sums and continuum-normalized states. Note that left eigenstates of H are right eigenstates of H^\dagger with a complex conjugate eigenvalue. If $|\phi_j\rangle$ is a right eigenstate of H with eigenvalue E_j , Equation (2.7) implies that $A|\phi_j\rangle$ is also a right eigenstate of H , with the same eigenvalue if A is linear, and with the complex conjugate eigenvalue E_j^* if A is antilinear. Instead, Equation (2.8) implies that $A|\phi_j\rangle$ is a right eigenstate of H^\dagger with eigenvalue E_j for A linear or E_j^* for A antilinear, or a left eigenstate of H with eigenvalue E_j^* for A linear, or E_j for A antilinear. As right and left eigenvectors must be treated on equal footing, since both are needed for the resolution (2.9), this argument points at a similar importance of the relations (2.7) and (2.8).

2.3 Time evolution for normalized states.

For a quantum system following the Schrödinger equation (2.4) with H non-Hermitian, in general the evolution will not be unitary and the norm $N_\psi(t) \equiv \langle\psi(t)|\psi(t)\rangle$ is not conserved. We shall assume the initial condition $N_\psi(0) = 1$. Using Equation (2.4), the rate of change of the norm is

$$\partial_t \langle\psi(t)|\psi(t)\rangle = \frac{1}{i\hbar} \langle\psi(t)|H - H^\dagger|\psi(t)\rangle. \quad (2.11)$$

2.3.1 Expectation Values

We now restrict the discussion to linear (not necessarily unitary) observables A . Since the state of the system is not normalized to 1 for $t > 0$, the expectation value formula has to take into account the norm explicitly,

$$\langle A \rangle(t) = \frac{\langle \psi(t) | A | \psi(t) \rangle}{\langle \psi(t) | \psi(t) \rangle}. \quad (2.12)$$

Since here A is linear we may use the standard Dirac “braket” notation for matrix elements with vertical bars. Using Equations (2.4) and (2.11) the rate of change of the expectation value of A is

$$\partial_t \langle A \rangle(t) = \frac{1}{i\hbar} \frac{\langle \psi(t) | \psi(t) \rangle \langle \psi(t) | AH - H^\dagger A | \psi(t) \rangle - \langle \psi(t) | H - H^\dagger | \psi(t) \rangle \langle \psi(t) | A | \psi(t) \rangle}{\langle \psi(t) | \psi(t) \rangle^2}. \quad (2.13)$$

For Hermitian Hamiltonians the commutation of A and H leaves the expectation values of A invariant. For non-Hermitian Hamiltonians the symmetry Equation (2.8) applied to Equation (2.13) gives

$$\partial_t \langle A \rangle(t) = \frac{-1}{i\hbar} \frac{\langle \psi(t) | H - H^\dagger | \psi(t) \rangle \langle \psi(t) | A | \psi(t) \rangle}{\langle \psi(t) | \psi(t) \rangle^2}. \quad (2.14)$$

If we use Equations (2.11) and (2.12) in Equation (2.14),

$$\frac{\langle A \rangle}{\langle \psi(t) | \psi(t) \rangle} \partial_t \langle \psi(t) | \psi(t) \rangle = -\partial_t \langle A \rangle, \quad (2.15)$$

$$\langle A \rangle \langle \psi(t) | \psi(t) \rangle = \text{Constant}. \quad (2.16)$$

Applying the initial condition $\langle \psi(0) | \psi(0) \rangle = 1$,

$$\langle A \rangle(t) = \frac{\langle A \rangle(0)}{\langle \psi(t) | \psi(t) \rangle}, \quad (2.17)$$

so the expectation value of an A that obeys $AH = H^\dagger A$, is simply rescaled by the norm of the wave function as it increases or decreases.

2.3.2 Lower Bound on the Norm of the Wave Function

The symmetry condition $AH = H^\dagger A$ may set lower bounds to the norm along the dynamical process. Consider a linear observable A with real eigenvalues $\{a_i\}$

bounded by $\max\{|a_i|\}$. Then, the expectation values satisfy $|\langle A \rangle| \leq \max\{|a_i|\}$. If we use the result in (2.17) we get

$$\langle \psi(t) | \psi(t) \rangle \geq \frac{|\langle A \rangle(0)|}{\max\{|a_i|\}}. \quad (2.18)$$

Equation (2.18) bounds the norm of the state due to symmetry conditions. A remarkable case is parity pseudohermiticity, $\Pi H = H^\dagger \Pi$, where the (unitary) parity operator acts on the position eigenstates as $\Pi |x\rangle = |-x\rangle$ and has eigenvalues $\{-1, 1\}$. Under this symmetry, Equation (2.18) gives

$$\langle \psi(t) | \psi(t) \rangle \geq |\langle \Pi \rangle(0)|, \quad (2.19)$$

where $\langle \Pi \rangle(0)$ is the expectation value of the state at $t = 0$.

2.4 Generic symmetries

We postulate that both (2.7) and (2.8), for A unitary or antiunitary, are symmetries of the Hamiltonian. A superoperator framework helps to understand why (2.8) also represents a symmetry. Let us define the superoperators $\mathcal{L}_A(\cdot) \equiv A^\dagger(\cdot)A$, $\mathcal{L}_\dagger(\cdot) \equiv (\cdot)^\dagger$ and $\mathcal{L}_{A,\dagger}(\cdot) \equiv \mathcal{L}_A(\mathcal{L}_\dagger(\cdot)) = \mathcal{L}_\dagger(\mathcal{L}_A(\cdot))$. For linear operators B and a complex number a they satisfy

$$\mathcal{L}_A(aB) = aA^\dagger BA, \quad A \text{ unitary}, \quad (2.20)$$

$$\mathcal{L}_A(aB) = a^* A^\dagger BA, \quad A \text{ antiunitary}, \quad (2.21)$$

$$\mathcal{L}_\dagger(aB) = a^* B^\dagger, \quad (2.22)$$

$$\mathcal{L}_{A,\dagger}(aB) = \mathcal{L}_\dagger \mathcal{L}_A(aB) = \mathcal{L}_A \mathcal{L}_\dagger(aB) = a^* A^\dagger B^\dagger A, \quad A \text{ unitary}, \quad (2.23)$$

$$\mathcal{L}_{A,\dagger}(aB) = \mathcal{L}_\dagger \mathcal{L}_A(aB) = \mathcal{L}_A \mathcal{L}_\dagger(aB) = a A^\dagger B^\dagger A, \quad A \text{ antiunitary}. \quad (2.24)$$

As the product of two antilinear operators is a linear operator, the resulting operators (on the right hand sides) are linear in all cases, independently of the linearity or antilinearity of A . This should not be confused with the linearity or antilinearity of the superoperators \mathcal{L} that may be checked by the invariance (for a linear superoperator) or complex conjugation (for an antilinear superoperator) of the constant a . Using the scalar product for linear operators F and G ,

$$\langle\langle F, G \rangle\rangle = \text{Tr}(F^\dagger G), \quad (2.25)$$

we find the adjoints,

$$\mathcal{L}_A^\dagger(\cdot) = \mathcal{L}_{A^\dagger}(\cdot) \equiv A(\cdot)A^\dagger, \quad (2.26)$$

$$\mathcal{L}_\dagger^\dagger(\cdot) = \mathcal{L}_\dagger(\cdot), \quad (2.27)$$

$$\mathcal{L}_{A,\dagger}^\dagger(\cdot) = \mathcal{L}_{A^\dagger,\dagger}(\cdot), \quad (2.28)$$

where $\langle\langle F, \mathcal{L}^\dagger G \rangle\rangle = \langle\langle G, \mathcal{L}F \rangle\rangle^*$ for \mathcal{L} linear and $\langle\langle F, \mathcal{L}^\dagger G \rangle\rangle = \langle\langle G, \mathcal{L}F \rangle\rangle$ for \mathcal{L} antilinear.

All the above transformations are unitary or antiunitary (in a superoperator sense), $\mathcal{L}^\dagger = \mathcal{L}^{-1}$, and they keep “transition probabilities” among two states, most generally represented by density operators ρ_1 and ρ_2 , invariant, namely

$$\langle\langle \rho_1, \rho_2 \rangle\rangle = \langle\langle \mathcal{L}\rho_1, \mathcal{L}\rho_2 \rangle\rangle. \quad (2.29)$$

Due to the Hermicity of the density operators, $\langle\langle \rho_1, \rho_2 \rangle\rangle$ is a real number (both for unitary or antinunitary \mathcal{L}). This result is reminiscent of Wigner’s theorem, originally formulated for pure states [35], but considering a more general set of states and transformations.

We conclude that all the above \mathcal{L} superoperators may represent symmetry transformations, and in particular Hamiltonian symmetries if they leave the Hamiltonian invariant, namely, if $\mathcal{L}H = H$. The following section provides specific examples for the set of symmetry transformations that may leave Hamiltonians for a particle in one dimension invariant, making use of transposition, complex conjugation, and inversion of coordinates or momenta.

As for the connection between symmetries and conservation laws, the results of the previous sections apply. It is possible to find quantities that on calculation remain invariant, but they are not necessarily physically significant.

2.5 Example of physical relevance of the relations $AH = HA$ or $AH = H^\dagger A$ as symmetries

In this section we exemplify the above general formulation of Hamiltonian symmetries for Hamiltonians of the form $H_0 + V$ corresponding to a spinless particle of mass m moving in one dimension, where $H_0 = P^2/(2m)$ is the kinetic energy, P is

the momentum operator, and V is a generic potential that may be non-Hermitian and non-local (non-local means that matrix elements in coordinate representation, $\langle x|V|y\rangle$, may be nonzero for $x \neq y$. Non-locality is as common as non-Hermiticity, in the sense that Feschbach's projection framework typically provides non-local effective Hamiltonians for the subsystems). We assume that H is diagonalizable, possibly with discrete and continuum parts. By inspection of Table 2.1, one finds a set of possible Hamiltonian symmetries described by the eight relations of the second column. They imply the invariance of the Hamiltonian with respect to the transformations represented by the superoperators in the third column. In coordinate or momentum representation, see the last two columns, each symmetry amounts to the invariance of the potential matrix elements with respect to some combination of transposition, complex conjugation and inversion of coordinates or momenta. (H_0 is invariant with respect to the eight transformations.)

Table 2.1 demonstrates that the eight transformations are complete when making only use of transposition, complex conjugation, inversion of the coordinates (or momenta), and their combinations. The eight superoperators form the elementary abelian group of order eight [36], with a minimal set of three generators $\mathcal{L}_\dagger, \mathcal{L}_\Pi, \mathcal{L}_\Theta$, from which all elements may be formed by multiplication, i.e., successive application. (Θ is the antilinear (antiunitary) time-reversal operator acting as $\Theta a|x\rangle = a^*|x\rangle$ in coordinate representation, and as $\Theta a|p\rangle = a^*|-p\rangle$ in momentum representation.) The eight superoperators may also be found from the generating set $\{\mathcal{L}_A\}, \mathcal{L}_\dagger$, where A is one of the elements of Klein's 4-group $\{1, \Theta, \Pi, \Pi\Theta\}$. These four operators commute. Moreover they are Hermitian and equal to their own inverses. The superoperators in the third column may be classified as antiunitary (symmetries II, IV, V, and VII) and unitary (symmetries I, III, VI, and VIII).

In [30] these symmetries are exploited to find relations among matrix elements of the scattering operators and selections rules that allow or disallow certain asymmetries in the reflection or transmission amplitudes for right and left incidence, a relevant information to implement microscopic asymmetrical devices such as diodes or rectifiers in quantum circuits [37].

To end this section we note the use of Equation (2.8) with differential operators different from the Klein's four-group set to generate non-PT local potentials with real spectra [6].

TABLE 2.1: Symmetries of the potential dependent on the commutativity or pseudo-hermiticity of $H = H_0 + V$ with the elements of Klein's 4-group $\{1, \Pi, \Theta, \Pi\Theta\}$ (second column). Each symmetry has a roman number code in the first column. Each symmetry may also be regarded as the invariance of the potential with respect to the transformations represented by superoperators \mathcal{L} in the third column. The kinetic part H_0 is invariant in all cases. In coordinate (fourth column) or momentum representation (last column), the eight transformations correspond to all possible combinations of transposition, complex conjugation, and inversion.

Code	Symmetry	Superoperator	$\langle x V y\rangle =$	$\langle p V p'\rangle =$
I	$1H = H1$	\mathcal{L}_1	$\langle x V y\rangle$	$\langle p V p'\rangle$
II	$1H = H^\dagger 1$	\mathcal{L}_\dagger	$\langle y V x\rangle^*$	$\langle p' V p\rangle^*$
III	$\Pi H = H\Pi$	\mathcal{L}_Π	$\langle -x V - y\rangle$	$\langle -p V - p'\rangle$
IV	$\Pi H = H^\dagger \Pi$	$\mathcal{L}_{\Pi\dagger}$	$\langle -y V - x\rangle^*$	$\langle -p' V - p\rangle^*$
V	$\Theta H = H\Theta$	\mathcal{L}_Θ	$\langle x V y\rangle^*$	$\langle -p V - p'\rangle^*$
VI	$\Theta H = H^\dagger \Theta$	$\mathcal{L}_{\Theta\dagger}$	$\langle y V x\rangle$	$\langle -p' V - p\rangle$
VII	$\Theta\Pi H = H\Theta\Pi$	$\mathcal{L}_{\Pi\Theta}$	$\langle -x V - y\rangle^*$	$\langle p V p'\rangle^*$
VIII	$\Theta\Pi H = H^\dagger \Pi\Theta$	$\mathcal{L}_{\Pi\Theta\dagger}$	$\langle -y V - x\rangle$	$\langle p' V p\rangle$

2.6 Discussion

The relations between invariance and symmetry are often emphasized, but for non-Hermitian Hamiltonians, which occur naturally as effective interactions, they become more complex and subtler than for Hermitian Hamiltonians. We have discussed these relations for time-independent Hamiltonians.

Time-dependent non-Hermitian Hamiltonians require a specific analysis and will be treated in more detail elsewhere. (In particular for a time-dependent H , exceptional points, not addressed here, may be crossed.) We briefly advance here some important differences with the time-independent Hamiltonians. 1969, Lewis and Riesenfeld [38] showed that the motion of a system subjected to time-varying forces admits a simple decomposition into elementary, independent motions characterized by constant values of some quantities (eigenvalues of the invariant). In other words, the dynamics is best understood, and is most economically described, in terms of invariants even for time-dependent Hamiltonians. In fact the powerful link between forces and invariants can be used in reverse order to inverse engineer from the invariant associated with some desired dynamics the necessary driving forces.

Invariants for Hermitian, time-dependent Hamiltonians obey the invariance condition

$$\frac{\partial I(t)}{\partial t} - \frac{1}{i\hbar}[H(t), I(t)] = 0, \quad (2.30)$$

so that $\frac{d}{dt}\langle\psi(t)|I(t)|\psi(t)\rangle = 0$ for states $\psi(t)$ that evolve with $H(t)$ (we assume that the invariant is linear). In general the operator $I(t)$ may depend on time and the invariant quantity is the expectation value $\langle\psi(t)|I(t)|\psi(t)\rangle$. In this context a Hamiltonian symmetry, defined by the commutativity of A with H as in (2.7) does not lead necessarily to a conservation law, unless A is time independent.

Invariant operators are useful to express the dynamics of the state $\psi(t)$ in terms of superpositions of their eigenvectors with constant coefficients [38]; also to do inverse engineering, as in shortcuts to adiabaticity, so as to find $H(t)$ from the desired dynamics [39, 40].

$I(t)$ may be formally defined by (2.30) for non-Hermitian Hamiltonians too, and its roles to provide a basis for useful state decompositions and inverse engineering are still applicable [39]. Note however that in this context $I(t)$ is not invariant in an ordinary sense, but rather

$$\frac{d}{dt}\langle\hat{\psi}(t)|I(t)|\psi(t)\rangle = 0. \quad (2.31)$$

The alternative option, yet to be explored for inverse engineering the Hamiltonian, is to consider (linear) operators $I'(t)$ such that

$$\frac{\partial I'(t)}{\partial t} - \frac{1}{i\hbar}[H(t)^\dagger I'(t) - I'(t)H(t)] = 0, \quad (2.32)$$

and thus $\frac{d}{dt}\langle\psi(t)|I'(t)|\psi(t)\rangle = 0$.

As an outlook for further work, it would be interesting to extend the present formalism to field theories [41], and to other generalized symmetries where intertwining operators A relate H to operators different from H^\dagger [42–44], for example $-H$ [45]. Klein's group may also be augmented by considering further symmetries due to internal states [23]. Applications in optical devices [46] and quantum circuits [30] may be expected.

Chapter 3

Real Eigenvalues of complex potentials

The complex eigenvalues of some non-Hermitian Hamiltonians, e.g. parity-time symmetric Hamiltonians, come in complex-conjugate pairs. We show that for non-Hermitian scattering Hamiltonians (of a structureless particle in one dimension) possessing one of four certain symmetries, the poles of the S -matrix eigenvalues in the complex momentum plane are symmetric about the imaginary axis, i.e. they are complex-conjugate pairs in complex-energy plane. This applies even to states which are not bounded eigenstates of the system, i.e. antibound or virtual states, resonances, and antiresonances. The four Hamiltonian symmetries are formulated as the commutation of the Hamiltonian with specific antilinear operators. Example potentials with such symmetries are constructed and their pole structures and scattering properties are calculated.

3.1 Introduction

Non-Hermitian (NH) Hamiltonians may represent effective interactions for components of a system. Feshbach's partitioning technique [26, 27] provides the formal framework to find NH-Hamiltonians for a subspace, from the Hermitian Hamiltonian for the total system. NH-Hamiltonians are also set phenomenologically to mimic some observed or desired behaviour, such as gain, decay or absorption in nuclear or atomic, molecular, and optical physics [1, 19, 46–49]. They arise as well as auxiliary tools to facilitate calculations of cross sections or resonances, e.g. by complex scaling of the coordinates [50, 51], and also to model some open systems [52] and lattices [53].

Much work on NH-physics has focused on PT-symmetric Hamiltonians, as they may have a purely real spectrum [28]. More recently, other NH and non-PT Hamiltonians, have been shown to hold real eigenvalues [6, 45, 54]. Work on scattering by PT-symmetric potentials was at first rather scarce [1, 2, 5, 55]. However, scattering has been later investigated intensely in connection with spectral singularities and reflection asymmetries for left or right incidence (i.e. unidirectional invisibility) [18, 56, 57], in most cases restricting the analysis to local potentials. Interestingly, it has been recently shown that different devices with asymmetrical scattering responses (i.e., with different transmission and/or reflection for right and left incidence in a 1D setting) are possible if one makes use of non-local potentials [30]. Ref. [30] provides the selection rules for the transmission and reflection coefficient asymmetries based on eight basic Hamiltonian symmetries. Four of these symmetries are of the standard form,

$$AH = HA, \quad (3.1)$$

and the other four are of the form

$$AH = H^\dagger A, \quad (3.2)$$

where A is a unitary or anti-unitary operator in Klein's 4-group $\mathbf{K}_4 = \{1, \Pi, \Theta, \Theta\Pi\}$ formed by the identity (1), parity (Π), time-reversal (Θ), and their product ($\Theta\Pi$), also termed PT . A Hamiltonian which has symmetry (3.2) is called A -pseudohermitian.

Here we aim at extending further our understanding of scattering of a structureless particle by NH-potentials in 1D by considering general potentials that are

not necessarily diagonal in coordinate representation (i.e., non-local potentials). These typically arise when applying Feshbach's partitioning technique [25]. The results of [30] are expanded in several directions:

- i) We provide an alternative characterization of the above-mentioned eight symmetries in terms of the invariance of H with respect to the action of superoperators. We also show that the four symmetries associated with A -pseudohermiticity relations (3.2) can be formulated as well as the commutativity of H with certain operators (linear if A is antilinear, and antilinear if A is linear). This formulation extends earlier results for Hamiltonians with a discrete spectrum [31, 58].
- ii) Moreover, four of these eight symmetries imply the same type of pole structure of S -matrix eigenvalues in the complex momentum plane that was found for PT symmetry [1], namely, zero-pole correspondence at complex-conjugate points, and poles on the imaginary axis or forming symmetrical pairs with respect to the imaginary axis.¹

This configuration with poles located on the imaginary axis or as symmetrical pairs has some important consequences. In particular, it provides stability of the real energy eigenvalues with respect to parameter variations of the potential. While a simple pole on the imaginary axis can move along that axis when a parameter is changed, it cannot move off this axis (since this would violate the pole-pair symmetry) or bifurcate. The formation of pole pairs occurs near special parameter values for which two poles on the imaginary axis collide.

The remainder of the article is organized as follows. In section 3.2 we review the scattering properties of eight different Hamiltonian symmetries. These symmetries may be characterized as commutativity or pseudohermiticity with respect to four unitary or antiunitary operators forming a Klein 4-group, or as invariance with respect to the action of eight linear or antilinear superoperators. In section 3.3 we discuss the physical consequences of the symmetries in the pole structure of the scattering matrix eigenvalues and hence in the transmission/reflection amplitudes. Four symmetries are shown to lead to complex poles corresponding to real energies

¹ S -matrix poles of Hermitian Hamiltonians are symmetric in the complex momentum plane with respect to the imaginary axis (see Fig. 3.1). In the upper half-plane they are on the imaginary axis and represent bound states. In the lower half-plane they come in symmetrical resonance and antiresonance pairs, and may also lie on the imaginary axis as “virtual states”. A further symmetry is the occurrence of a zero at the complex-conjugate momentum of a given pole. These properties are well known for partial wave scattering by spherical potentials but also hold for the S -matrix eigenvalues in one dimensional scattering [1]. For NH-Hamiltonians the above pole- and pole/zero-symmetries do not hold in general.

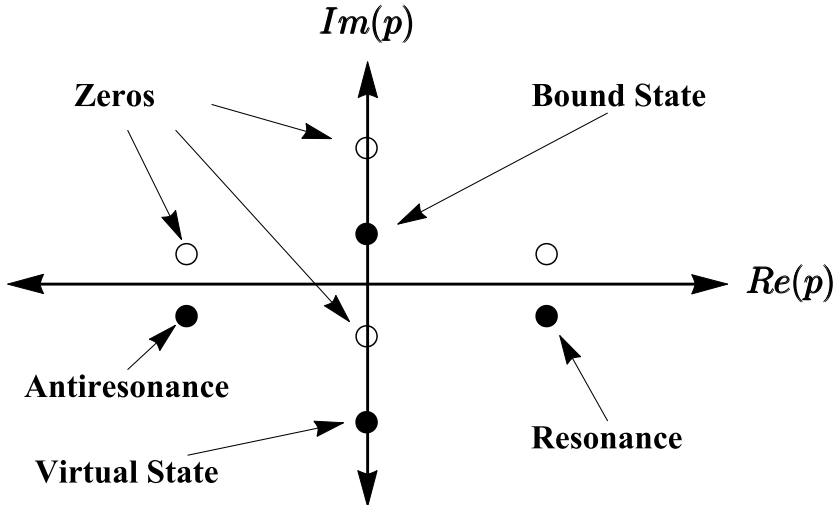


FIGURE 3.1: Example of configuration of poles (filled circles) and zeros (empty circles) of the S -matrix eigenvalues in the complex momentum plane for hermitian Hamiltonians. Poles in the upper half plane ($\text{Im}(p) > 0$) correspond to bound eigenstates of the Hamiltonian, i.e. localized states with negative energy. Poles in the lower half plane correspond to virtual states ($\text{Re}(p) = 0$), resonances ($\text{Re}(p) > 0$) and antiresonances ($\text{Re}(p) < 0$). The singularities with negative imaginary part correspond to states that do not belong to the Hilbert space since they are not normalizable. However, they can produce observable effects in the scattering amplitudes, in particular when they approach the real axis. The pole structure of symmetries IV, V, and VII, see Table I, is similar, but pole pairs are also possible in the upper half-plane.

or conjugate (energy) pairs. In section 3.4 we exemplify the general results with separable potentials exhibiting parity-pseudohermiticity and time-reversal symmetry. These are the two non-trivial symmetries of the four (in the sense that the other two, hermiticity and PT-symmetry, are already well discussed). In section 3.5 we discuss and summarize our results.

3.2 Hamiltonian Symmetries

3.2.1 Basic concepts and terminology

Let us first clarify the terminology. Scattering Hamiltonians are the ones that can be written as the sum of kinetic energy $H_0 = p^2/(2m)$ operator and a potential energy operator V ,

$$H = H_0 + V. \quad (3.3)$$

1 Code	2 Symmetry	3 $\langle x V y\rangle$	4 \mathcal{L} (coord)	5 $\langle p V p'\rangle$	6 \mathcal{L} (momentum)	7 $\langle p S p'\rangle$
I	$1H = H1$	$\langle x V y\rangle$	1	$\langle p V p'\rangle$	1	$\langle p S p'\rangle$
II	$1H = H^\dagger 1$	$\langle y V x\rangle^*$	$\mathcal{T}\mathcal{C}$	$\langle p' V p\rangle^*$	$\mathcal{T}'\mathcal{C}'$	$\langle p \widehat{S} p'\rangle$
III	$\Pi H = H\Pi$	$\langle -x V - y\rangle$	\mathcal{I}	$\langle -p V - p'\rangle$	\mathcal{I}'	$\langle -p S - p'\rangle$
IV	$\Pi H = H^\dagger \Pi$	$\langle -y V - x\rangle^*$	$\mathcal{CT}\mathcal{I}$	$\langle -p' V - p\rangle^*$	$\mathcal{C}'\mathcal{T}'\mathcal{I}'$	$\langle -p \widehat{S} - x\rangle$
V	$\Theta H = H\Theta$	$\langle x V y\rangle^*$	\mathcal{C}	$\langle -p V - p'\rangle^*$	$\mathcal{T}'\mathcal{C}'$	$\langle -p' \widehat{S} - y\rangle$
VI	$\Theta H = H^\dagger \Theta$	$\langle y V x\rangle$	\mathcal{T}	$\langle -p' V - p\rangle$	$\mathcal{I}'\mathcal{T}'$	$\langle -p' \widehat{S} - x\rangle$
VII	$\Theta\Pi H = H\Theta\Pi$	$\langle -x V - y\rangle^*$	\mathcal{IC}	$\langle p V p'\rangle^*$	\mathcal{C}'	$\langle p' \widehat{S} p\rangle$
VIII	$\Theta\Pi H = H^\dagger \Theta\Pi$	$\langle -y V - x\rangle$	\mathcal{IT}	$\langle p' V p\rangle$	\mathcal{T}'	$\langle p' \widehat{S} p\rangle$

TABLE 3.1: Symmetries of the potential based on the commutativity or pseudohermiticity of H with the elements of \mathbf{K}_4 (column 2). Columns 3, 5, and 7 to 11 are to be read as follows: For each symmetry the object in the column is equal to the one in the top row of the column. The relations among potential matrix elements are given in coordinate and momentum representations in the third and fifth columns. In columns 4 and 6, each symmetry is regarded as the invariance of the potential with respect to the transformations represented by superoperators \mathcal{L} (see Sec. 3.2.2) in coordinate or momentum representation. The fifth column gives the relations they imply in the matrix elements of S and \widehat{S} matrices. The final four columns set the relations for the scattering amplitudes.

V is in general non-local, i.e., it does not have the local form $\langle x|V|x'\rangle = \delta(x - x')V(x)$. Apart from their generic appearance in Feschbach's partitioning technique, see e.g. [25], non-local potentials are quite common in models that discretize the coordinates at specific sites, as in tight-binding models. These are widely used for describing condensed matter and ultracold atoms in a lattice. For example, the well known Bose-Hubbard model has been generalized to a non-Hermitian Hamiltonian to account for dissipation effects, see e.g. [59, 60]. However, here we limit ourselves to continuous-coordinate scattering models.² The potential function in position coordinates $V(x, x') = \langle x|V|x'\rangle$ is assumed to decay fast enough to 0 when a position goes to infinity so that the usual operators of scattering theory are well defined and the Hilbert space is (biorthogonally) decomposed into a continuum part with real eigenvalues and a discrete part. See Appendix .1 for a review of the formalism and notation we use.

² Also, discrete Hamiltonian matrix models abound in many fields, for example quantum optics, in which rather than couplings among different “sites” there are couplings among states or levels. Thus a generalized concept of “non-locality” may be applied, as being equivalent to non-zero non-diagonal elements in the chosen basis. The non-Hermitian symmetry groups in these discrete models can be larger than the set of symmetries based on Eqs. (3.1) and (3.2) described here, which are constrained by the structure of H_0 . Discrete model symmetries, interesting as they are, and with potential applications in condensed matter, optics, or quantum optics, lie beyond the scope of this work and need a deeper separate study.

We will now discuss the eight symmetries identified in [30], which are associated with the two generalized symmetry relations corresponding to commutation with A and A -pseudohermiticity [31], see Eqs. (3.1,3.2). We use Roman numeral to label these symmetries as shown in Table I: I ($1H = H1$, the trivial identity) ; II ($1H = H^\dagger 1$, hermiticity or “1-pseudohermiticity”); III ($\Pi H = H\Pi$, parity); IV ($\Pi H = H^\dagger \Pi$, Π -pseudohermiticity); V ($\Theta H = H\Theta$, time-reversal invariance); VI ($\Theta H = H^\dagger \Theta$, Θ -pseudohermiticity); VII ($\Pi\Theta H = H\Pi\Theta$, PT-symmetry); VIII ($\Pi\Theta H = H\Pi\Theta$, $\Pi\Theta$ -pseudohermiticity). Note that a local potential would automatically fulfill symmetry VI but this symmetry does not necessarily imply locality. For local potentials four of the eight symmetries coincide with the other four [30]. Here we consider general nonlocal potentials where all the eight symmetries are distinct.

The generalization of the symmetry concept to the pair (3.1) and (3.2) is in fact quite natural if we take into account that a $NH-H$ has generically different left and right eigenvectors. Given a right eigenstate $|\psi\rangle$ of H with eigenvalue E , Eq. (3.1) implies that $A|\psi\rangle$ is also a right eigenvector with eigenvalue E or E^* , whereas Eq. (3.2) implies that $\langle\psi|A$ is a left eigenvector of H with eigenvalues E^* or E , for A unitary or antiunitary respectively.³

The symmetries which imply the presence of real or complex-conjugate pairs of energy eigenvalues for bound eigenstates are II, IV, V and VII. The emergence of these complex-conjugate pairs has been previously discussed in [31, 61] for a general class of diagonalizable Hamiltonians that posses a discrete spectrum. They can be heuristically understood for the symmetries we consider as follows: Symmetry V implies that the Hamiltonian must be real in coordinate space, which would lead to a real characteristic polynomial with real or complex-conjugate roots. Symmetry VII is PT symmetry which is well discussed in the literature as having real or complex-conjugate pairs of eigenvalues [28]. Note also that the matrix elements of PT-symmetric Hamiltonians are real in the momentum representation. More generally, in [58], it was shown, for diagonalizable Hamiltonians having a discrete spectrum, that A -pseudohermiticity for a Hermitian invertible linear operator A is equivalent to the presence of an ordinary symmetry of the form $BH = HB$ for some antilinear operator B with $B^2 = 1$. Because B is an antilinear operator, the

³ A is an antiunitary operator if it is an antilinear operator that maps a Hilbert space onto itself satisfying $\langle A\psi, A\phi\rangle = \langle\phi, \psi\rangle$ for ψ and ϕ in that Hilbert space. It satisfies $AA^\dagger = A^\dagger A = 1$, where the adjoint is to be understood as for antilinear operators, namely $\langle\phi, A^\dagger\psi\rangle = \langle\psi, A\phi\rangle$ [1].

eigenvectors $|E_n\rangle$ of H with eigenvalues E_n satisfy

$$\begin{aligned} HB|E_n\rangle &= BH|E_n\rangle \\ &= E_n^*B|E_n\rangle. \end{aligned} \quad (3.4)$$

Therefore complex eigenvalues E_n come in complex-conjugate pairs. In particular, when $|E_n\rangle$ is an eigenvector of B , i.e., $B|E_n\rangle = e^{ib_n}|E_n\rangle$ for some real number b_n , we have $E_n \in \mathbb{R}$. The proof of the equivalence of A -pseudohermiticity for linear A and the presence of ordinary antilinear symmetries given in [58] relies on the observation that every diagonalizable Hamiltonian with a discrete spectrum is τ -pseudohermitian for some invertible Hermitian antilinear operator τ , i.e., $\tau H = H^\dagger\tau$. This relation together with Eq. (3.2) implies $BH = HB$, if we set $B = A^{-1}\tau$. (If $AH = H^\dagger A$ and A is a Hermitian antilinear operator, a linear $B = A^{-1}\tau$ can also be constructed so that $BH = HB$, but the E_n do not form conjugate pairs.) In Appendix .2 we extend this construction to scattering potentials.

In summary, the symmetries with conjugate pairs II, IV, V, and VII can be all expressed as the commutation of H with a certain antilinear operator, as seen directly in the symmetries V and VII, in which H commutes with an antilinear A , and by constructing an antilinear B in the symmetries II and IV. A novel aspect uncovered in this paper is that whenever one of the above-mentioned four symmetries holds not only the complex eigenvalues representing the bound states come in conjugate-complex pairs, but all the complex poles of the S -matrix have this property.

3.2.2 Superoperator formalism

The eight symmetries listed in Table I may also be regarded as the invariance of the Hamiltonian matrix with respect to transformations represented by superoperators \mathcal{L} [62] defined by

$$\mathcal{L}(H) = \begin{cases} A^\dagger HA & \text{I, III, V, VII} \\ A^\dagger H^\dagger A & \text{II, IV, VI, VIII} \end{cases}. \quad (3.5)$$

This definition of the superoperator action is independent of the representation we use, but its realization in coordinates or momenta in terms of the operations of complex conjugation, transposition, and inversion is different. For example,

in coordinate representation, these superoperators take the following forms (see column 3 in Table I),

$$\begin{aligned} 1H &= \iint |x\rangle\langle x|H|y\rangle\langle y|dxdy, \\ \mathcal{T}(H) &= \iint |x\rangle\langle y|H|x\rangle\langle y|dxdy, \\ \mathcal{C}(H) &= \iint |x\rangle\langle x|H|y\rangle^*\langle y|dxdy, \\ \mathcal{I}(H) &= \iint |x\rangle\langle -x|H|y\rangle\langle y|dxdy. \end{aligned} \quad (3.6)$$

Adopting the following inner product for linear operators F and G , $\langle\langle F|G \rangle\rangle = \text{tr } F^\dagger G$, we can show that all superoperators \mathcal{L} are either unitary (for $\mathcal{L} = 1, \mathcal{T}, \mathcal{I}, \mathcal{T}\mathcal{I}$), or antiunitary (for $\mathcal{L} = \mathcal{C}, \mathcal{CT}, \mathcal{CI}, \mathcal{CTI}$), as defined by

$$\langle\langle \mathcal{L}F|\mathcal{L}G \rangle\rangle = \langle\langle F|G \rangle\rangle \quad (\mathcal{L} \text{ unitary}), \quad (3.7)$$

$$\langle\langle \mathcal{L}F|\mathcal{L}G \rangle\rangle = \langle\langle F|G \rangle\rangle^* \quad (\mathcal{L} \text{ antiunitary}). \quad (3.8)$$

They all satisfy $\mathcal{L}\mathcal{L}^\dagger = \mathcal{L}^\dagger\mathcal{L} = 1$ where the adjoints are defined differently for linear or antilinear superoperators,

$$\langle\langle F|\mathcal{L}^\dagger G \rangle\rangle = \langle\langle \mathcal{L}F|G \rangle\rangle \quad (\mathcal{L} \text{ unitary}), \quad (3.9)$$

$$\langle\langle F|\mathcal{L}^\dagger G \rangle\rangle = \langle\langle \mathcal{L}F|G \rangle\rangle^* \quad (\mathcal{L} \text{ antiunitary}). \quad (3.10)$$

Moreover the eight superoperators satisfy $\mathcal{L}^\dagger = \mathcal{L}$.

The set $\{1, \mathcal{I}, \mathcal{T}, \mathcal{C}, \mathcal{CT}, \mathcal{T}\mathcal{I}, \mathcal{IC}, \mathcal{CTI}\}$ forms the elementary abelian group E8 [36]. This is a homocyclic group, namely, the direct product of isomorphic cyclic groups of order 2 with generators $\mathcal{C}, \mathcal{T}, \mathcal{I}$. We may, similarly to Eq. (3.6), define primed superoperators in momentum representation, e.g. $\mathcal{T}'H = \iint |p\rangle\langle p'|H|p\rangle\langle p'|dpdp'$. They also form the E8 group $\{1, \mathcal{I}', \mathcal{T}', \mathcal{C}', \mathcal{CT}', \mathcal{T}'\mathcal{I}', \mathcal{IC}', \mathcal{CTI}'\}$. Only for the subgroup $\{1, \mathcal{I}, \mathcal{CT}, \mathcal{CTI}\}$ the superoperators have the same representation-independent form in terms of complex conjugation, transposition and inversion.

A direct application of the superoperator framework is the generalization of Wigner's formulation of symmetries [35]. He associated symmetry transformations to unitary or antiunitary operators preserving the (Hilbert space) inner product, namely the “transition probabilities” $|\langle A\psi, A\phi \rangle|^2 = |\langle \psi, \phi \rangle|^2$. For general states described by density operators ρ_1, ρ_2 , transition probabilities are computed

as $\langle\langle\rho_1|\rho_2\rangle\rangle$ and the transformations described by the unitary or antiunitary superoperators preserve the transition probability. Hamiltonian symmetries are, within the conventional Wigner scheme, the symmetry transformations that leave the Hamiltonian invariant ($A^\dagger H A = H$, so that A and H commute). Here the Hamiltonian symmetry is more broadly defined as the invariance $\mathcal{L}H = H$, which includes transformations beyond the conventional scheme.

3.3 S-matrix pole structure

To derive the results in [30] an extensive use of the scattering matrix (S -matrix) formalism was made. The full S -matrix provides outgoing waves when acting on incoming waves. It is typically decomposed into on-the-energy-shell matrices. In 1D scattering, the on-the-energy-shell $\mathbf{S}(p)$ matrix for H is defined on the real positive momentum axis in terms of transmission and reflection amplitudes for right and left incidence [1],

$$\mathbf{S} = \begin{pmatrix} T^l(p) & R^r(p) \\ R^l(p) & T^r(p) \end{pmatrix}. \quad (3.11)$$

There is a companion matrix $\widehat{\mathbf{S}}$ with hatted amplitudes corresponding to scattering by H^\dagger . See Appendix .1 and [1] for details. The \mathbf{S} matrix contains the scattering amplitudes for incoming wave packets with well defined momentum being scattered into states with the same kinetic energy and reflected and transmitted components. For negative p the matrix elements give the amplitudes of scattering states with a pure outgoing plane wave towards the right or the left. Moreover we assume, as it is customary, that the amplitudes may be continued analytically beyond the real axis. The existence of a continuation on a complex plane domain depends on decay properties of the potentials and may be checked for each potential. The analytical continuation is indeed possible for the model potentials of the following section.

The eigenvalues of \mathbf{S} can be calculated from the transmission and reflection amplitudes as

$$S_j = \frac{(T^l + T^r) + (-1)^j[(T^l - T^r)^2 + 4R^l R^r]^{1/2}}{2} \quad (3.12)$$

for $j = 1, 2$, and of course there is a similar expression for \widehat{S}_j with hatted amplitudes. In general they satisfy the relations [1],

$$S_j(p) = \widehat{S}_j^*(-p^*) , \quad (3.13)$$

and

$$\widehat{S}_j^*(p^*)S_j(p) = 1 . \quad (3.14)$$

Combining Eqs. (3.13) and (3.14) gives

$$S_j(p) = S_j^{-1}(-p) . \quad (3.15)$$

Equation (3.15) is remarkable since it reveals the presence of a pole (zero) at $-p$ if there is a zero (pole) at p . If the following relations are fulfilled,

$$T^{r,l}(p) = \widehat{T}^{r,l}(p) \text{ or } T^{r,l}(p) = \widehat{T}^{l,r}(p), \quad (3.16)$$

$$R^{r,l}(p) = \widehat{R}^{r,l}(p) \text{ or } R^{r,l}(p) = \widehat{R}^{l,r}(p), \quad (3.17)$$

then

$$S_j(p) = \widehat{S}_j(p), \quad (3.18)$$

which together with Eq. (3.13) gives

$$S_j(p) = S_j^*(-p^*) . \quad (3.19)$$

In plain language, Eq. (3.19) tells that if Eqs. (3.16) and (3.17) are satisfied, the poles and zeros of S_j must be symmetrically distributed with respect to the imaginary axis of momentum complex plane. Combined with Eq. (3.15) this also means that each pole has a symmetrical zero with respect to the real axis. This symmetrical distribution of poles and zeros is the same as in the Hermitian case (see Fig. 3.1), the only difference being the possibility of finding pairs of symmetrical poles in the upper complex plane when $H \neq H^\dagger$. They represent normalizable “bound states with complex energies”. When they are not present, the discrete spectrum becomes purely real.

According to Table I, Eqs. (3.16) and (3.17) are fulfilled for symmetries II (hermiticity), VII (PT-symmetry), IV (parity pseudohermiticity), and V (time-reversal invariance). Thus, Hamiltonians having these symmetries have their S –matrix poles symmetrically distributed around the imaginary axis. For local potentials

the last two symmetries coalesce with the first two well-known cases [30], namely, IV becomes equivalent to PT-symmetry, and V becomes equivalent to hermiticity. For non-local potentials, though, these symmetries correspond to genuinely distinct properties. In the following section we shall demonstrate this fact with potentials that are either purely parity-pseudohermitian (and not PT-symmetrical), or time-reversal invariant but not Hermitian.

3.4 Separable Potentials

In order to illustrate and test the theoretical concepts that we have discussed, in particular the symmetrical configuration of poles with respect to the imaginary axis in the complex momentum plane for certain Hamiltonian symmetries, we will use some solvable toy models consisting on rank-one separable potentials. Separable potentials are quite useful models as a solvable approximation to realistic ones, in particular in nuclear, atomic and molecular physics [63]. Often they lead to explicit expressions for wave functions or scattering amplitudes, so they are used to test concepts and new methods. They are also instrumental in learning about different dynamical phenomena (for example transient effects, short-time and long-time behavior, or anomalous decay laws) and their relation to complex-plane singularities [64–67]. Their simplest version takes the form $|\chi\rangle V_0 \langle\chi|$ for some χ . In particular, with a complex V_0 , they have been used to examine anomalous (negative) time delays caused by crossing of zeroes of the S -matrix eigenvalues or S -matrix elements across the momentum real axis [68].

In this work we consider the simple structure $V = V_0 |\phi\rangle\langle\chi|$, with V_0 (potential strength) real, and conveniently chosen functions ϕ, χ . The aim of this section is to demonstrate the formal results of the previous section without attempting to simulate any specific systems, but we note that separable, NH potentials are instrumental to model nuclear reactions, in particular by increasing the rank (number of separable terms) [69]. Separable NH potentials also provide solvable approximations to nonlocal NH potentials that arise naturally in quantum optics to describe the interaction of a ground state atom with a laser beam [25]. In passing we shall also note some interesting phenomena that may be studied in more detail elsewhere, such as pole collisions, crossings of the real axis, or diodic (Maxwell demon) behavior with asymmetrical transmission for right/left incidence.

From the stationary Schrödinger equation $H|\psi\rangle = E|\psi\rangle$, the eigenvalues of separable potentials may be found by solving

$$Q_0(E)V_0 = 1, \quad (3.20)$$

where $Q_0(E) = \langle\chi|(E - H_0)^{-1}|\phi\rangle$ and $H_0 = p^2/(2m)$. Moreover, for a separable potential, the transition operator T_{op} can be written (see Appendix .3.1) as

$$T_{op} = \frac{V_0}{1 - V_0 Q_0(E)} |\phi\rangle\langle\chi|. \quad (3.21)$$

Since all scattering amplitudes in S are simply related to matrix elements of T_{op} in momentum representation, see Eq. (35), solutions to Eq. (3.20) provide their core singularities (independent of the representation [65]). Once $Q_0(E)$ is calculated, the transmission and reflection amplitudes can be found from (35) using the momentum representation of $|\phi\rangle$ and $|\chi\rangle$.

In the following subsections we will build a Hamiltonian with symmetry V (time reversal) and another one with symmetry IV (parity pseudohermicity) and illustrate the symmetries of the S matrix poles in momentum complex plane.

3.4.1 Time-reversal symmetric potential

We start with an example of a separable potential which only satisfies symmetry V (apart from the trivial symmetry I). The normalised vector $|\chi\rangle$, is given in position and momentum representation as

$$\begin{aligned} \langle x|\chi\rangle &= \sqrt{\frac{a}{\hbar}} e^{-a|x|/\hbar}, \\ \langle p|\chi\rangle &= \sqrt{\frac{2a^3}{\pi}} \frac{1}{p^2 + a^2}. \end{aligned} \quad (3.22)$$

We choose $|\phi\rangle$ similarly as

$$\begin{aligned} \langle x|\phi\rangle &= \sqrt{\frac{2ab}{\hbar(a+b)}} \begin{cases} e^{-bx/\hbar} & x > 0, \\ e^{ax/\hbar} & x < 0, \end{cases} \\ \langle p|\phi\rangle &= \sqrt{\frac{ab}{\pi(a+b)}} \frac{a+b}{(p+ia)(p-ib)}. \end{aligned} \quad (3.23)$$

The real and positive parameters \hbar/a and \hbar/b determine the width of the potential functions in coordinate representation. b is chosen different from a to introduce a right/left asymmetry in $\langle x|\phi\rangle$. In coordinate representation the potential is given as

$$\langle x|V|y\rangle = V_0 \sqrt{\frac{2ba^2}{\hbar^2(a+b)}} \begin{cases} e^{-(a|y|+bx)/\hbar} & x > 0, \\ e^{a(x-|y|)/\hbar} & x < 0. \end{cases} \quad (3.24)$$

Clearly the potential is always even in y and in the limiting case where $a = b$, it is also even in x . For $a = b$, the potential will satisfy parity symmetry (III) and also PT symmetry (VII), without asymmetric transmission or reflection.

We define first a complex momentum $q = \sqrt{2mE}$ (for complex E) with positive imaginary part. To calculate $Q_0(q)$ explicitly we use a closure relation in momentum representation, and complex contour integration around the poles at ia , q and ib . The result is then analytically continued to the whole q -plane,

$$Q_0(q)/m = -\frac{i\sqrt{2b}[2a(a+b)^2 - q^2(3a+b) - iq(2a+b)(3a+b)]}{q(a+b)^{3/2}(a-iq)^2(b-iq)}, \quad (3.25)$$

with which we may calculate the transmission and reflection amplitudes. The four roots of Eq. (3.20) are the core poles.

Using m , V_0 and \hbar we define the length and momentum scales $L_0 = \hbar/\sqrt{mV_0}$ and $p_0 = \sqrt{mV_0}$. In Fig. 3.2(a), we can see the trajectory of the S -matrix core poles (zeros of $1 - V_0 Q_0(q)$) for varying V_0 . Notice a bound state for $V_0 < 0$ and collisions of the eigenvalue pairs around $V_0 = 0$. In Figs. 3.2(b) and 3.2(c), where V_0 is positive and a or b are varied, there are two virtual states and one resonance/anti-resonance pair. In all cases the symmetry of the poles about the imaginary axis which corresponds to real energies or complex-conjugate pairs of energies, is evident. For larger values of the a or b parameters (not shown) the pair collides so that all poles end up as virtual states.

Figure 3.3 depicts the associated transmission and reflection coefficients (square moduli of the amplitudes) as functions of the momentum p . $|R^l(p)| = |R^r(p)|$ for all p due to symmetry V [30]. The coefficients can be greater than one in contrast to the Hermitian case.

3.4.2 Parity pseudohermitian potential

As a second example we will consider a separable potential which only fulfils symmetry IV. The normalised vector $|\chi\rangle$ in position and momentum representation is

$$\begin{aligned}\langle x|\chi\rangle &= \sqrt{\frac{a}{\hbar}} \begin{cases} e^{-(a+ib)x/\hbar} & x > 0, \\ e^{ax/\hbar} & x < 0, \end{cases} \\ \langle p|\chi\rangle &= \sqrt{\frac{a}{2\pi}} \frac{2a+ib}{(p+ia)(p+b-ia)},\end{aligned}\quad (3.26)$$

where $a > 0$ and b is real. We choose $|\phi\rangle$ as

$$\begin{aligned}\langle x|\phi\rangle &= \sqrt{\frac{a}{\hbar}} \begin{cases} e^{-ax/\hbar} & x > 0, \\ e^{(a+ib)x/\hbar} & x < 0, \end{cases} \\ \langle p|\phi\rangle &= \sqrt{\frac{a}{2\pi}} \frac{2a+ib}{(p-ia)(p-b+ia)},\end{aligned}\quad (3.27)$$

where \hbar/a gives as before the width in coordinate representation. The potential functions in coordinate representation become asymmetrical because of the imaginary terms ib in the exponent added only on one side. This term leads to oscillations in real and imaginary parts. In momentum representation b appears as a real shift in the position of one of the poles. In coordinate representation the potential is

$$\langle x|V|y\rangle = \frac{aV_0}{\hbar} \begin{cases} e^{-[a(x+y)-iby]/\hbar}, & x > 0, y > 0 \\ e^{a(y-x)/\hbar}, & x > 0, y < 0 \\ e^{[a(x-y)+ib(x+y)]/\hbar}, & x < 0, y > 0 \\ e^{[a(x+y)+ibx]/\hbar}, & x < 0, y < 0 \end{cases}. \quad (3.28)$$

The case $b = 0$ implies that the potential is real and hence satisfies time-reversal symmetry (V) with equal reflection amplitudes (as in the previous case), and also symmetry VIII.

By calculating Q_0 again explicitly using complex contour integration around the poles at $-q$, $-b - ia$ and $b - ia$, we get that

$$\begin{aligned} Q_0(q)/m \\ = \frac{8a^2q^3 - 4a^2q(10a^2 + b^2) - ia(4a^2 + b^2)^2 + 32ia^3q^2}{q(4a^2 + b^2)(a - iq)^2[b^2 + (a - iq)^2]}. \end{aligned} \quad (3.29)$$

Equation (3.20) has five roots in this case constituting core poles of the S matrix elements.

Figure 3.4 depicts the trajectories of these poles for varying a , b or V_0 . As for the previous potential, the poles are symmetric with respect to the imaginary axis. In Fig. 3.4(a) there is a single bound state for $V_0 < 0$ while for positive values there are a resonance/antiresonance pair and a pair of virtual states. There are collisions of eigenvalues for values of V_0 close to 0. In Fig. 3.4(b) two complex-conjugate (bound) eigenvalues cross the real axis and become a resonance/antiresonance pair. At the exact point where the eigenvalues are on the real axis, the scattering amplitudes diverge, however the eigenvalues of the S matrix do not, since divergences of the left and right amplitudes cancel each other. For $a \approx 4.55 p_0$ a resonance/antiresonance pair collides and becomes a pair of virtual states. In Fig. 3.4(c) another crossing of the real axis takes place, but in this case when decreasing b .

Figure 3.5 depicts the associated transmission and reflection coefficients as functions of the momentum p . The eigenvalues are not always equal since parity pseudohermiticity does not imply any strict restriction to them [30]. For large momenta, i.e. $p \gg \sqrt{2}p_0$, the potential is transparent giving $T^l, T^r \approx 1$. For $p \approx 1.5 p_0$ the right incidence transmission has a pronounced peak. Comparing with 3.4(c), we notice that the values of the potential parameters and the momentum are close to the ones for which the real axis crossing takes place. Around $p = 0.6 p_0$ the potential acts as an asymmetric transmitter [30].

3.5 Conclusion

In this paper we have studied some aspects of the scattering of a structureless particle in one dimension by generally non-local and non-Hermitian potentials.

Conditions that were found for discrete Hamiltonians to imply conjugate pairs of discrete eigenenergies (pseudohermiticity with respect to a linear operator or commutativity of H with an antilinear operator [31, 58, 70]) can in fact be extended to scattering Hamiltonians in the continuum, implying symmetry relations not just for bound-state eigenvalues but also for complex poles of the S -matrix. Specifically the poles of S matrix eigenvalues are symmetrically located with respect to the imaginary axis, also in the lower momentum plane, so that resonances and antiresonance energies are conjugate pairs as well. In terms of the eight possible Hamiltonian symmetries associated with Klein's group of A operators (unity, parity, time reversal and PT) and their commutation or pseudohermiticity with H , the symmetrical disposition of the poles applies to four of them, which includes hermiticity and PT-symmetry. Potential models and pole motions are provided for the two other non trivial symmetries: time-reversal symmetry and parity pseudohermiticity.

The study contributes to deepen our understanding of asymmetric scattering (with different responses for left/right incidence) beyond the much studied PT-symmetric potentials. This work opens interesting perspectives in AMO physics where much activity on asymmetric-scattering, mostly via optical devices, is currently being carried out. Moreover asymmetric devices such as rectifiers, Maxwell demons, or diodes will be fundamental to develop quantum technologies and quantum information. For future work we plan to consider more complicated systems including internal states, as well as physical realizations of the different symmetries in quantum optical systems.

.1 Review of scattering theory formalism

A detailed overview of scattering theory can be found in [3] and its extension to NH systems in [1]. Scattering theory describes the interaction of an incoming wave packet with a localized potential. In general, the spectrum of scattering Hamiltonians (as defined at the beginning of section 3.2) has both a discrete part and a continuum with real, positive energies. The eigenstates of the continuous spectrum are constructed by the action on plane waves of the Möller operators

$|p^\pm\rangle = \Omega_\pm |p\rangle$ and $|\widehat{p}^\pm\rangle = \widehat{\Omega}_\pm |p\rangle$, where

$$\begin{aligned}\Omega_+ &= \lim_{t \rightarrow -\infty} e^{iHt/\hbar} e^{-iH_0 t/\hbar}, \\ \Omega_- &= \lim_{t \rightarrow \infty} e^{iH^\dagger t/\hbar} e^{-iH_0 t/\hbar}, \\ \widehat{\Omega}_+ &= \lim_{t \rightarrow -\infty} e^{iH^\dagger t/\hbar} e^{-iH_0 t/\hbar}, \\ \widehat{\Omega}_- &= \lim_{t \rightarrow \infty} e^{iHt/\hbar} e^{-iH_0 t/\hbar},\end{aligned}\tag{30}$$

and a regularization of the limit is implied, see e.g. [1]. The Möller operators satisfy the isometry relation $\widehat{\Omega}_\pm^\dagger \Omega_\pm = 1$ and the intertwining relations $H\Omega_+ = \Omega_+ H_0$ and $H^\dagger \Omega_- = \Omega_- H_0$. By using the intertwining relations, it is easy to see that $|p^+\rangle$ and $|\widehat{p}^-\rangle$ are right eigenvectors of H while $|\widehat{p}^+\rangle$ and $|p^-\rangle$ are left eigenvectors of H , all with positive energy $E_p = p^2/2m$. In the following we will assume that the Hamiltonian admits a basis of biorthonormal right/left eigenstates $\{|\psi_n\rangle, |\phi_a\rangle\}$ with energies E_n satisfying $\langle\phi_n|\psi_m\rangle = \delta_{n,m}$ for the discrete part. The stationary scattering states are also biorthonormal, i.e. $\langle\widehat{p}^+|q^+\rangle = \langle\widehat{p}^-|q^-\rangle = \delta(p-q)$ and together with the eigenstates of the discrete spectrum they give the resolution of the identity

$$\begin{aligned}1 &= \sum_n |\psi_n\rangle\langle\phi_n| + \int_{-\infty}^{\infty} dp |p^+\rangle\langle\widehat{p}^+| \\ &= \sum_n |\psi_n\rangle\langle\phi_n| + \int_{-\infty}^{\infty} dp |\widehat{p}^-\rangle\langle p^-|.\end{aligned}\tag{31}$$

There is no degeneracy in the discrete spectrum of one-dimensional systems, whereas the continuum is doubly degenerate, e.g. with continuum eigenfunctions incident from the right or the left. We shall explicitly make use of this property in what follows. Using the resolution of the identity in terms of discrete eigenstates and the stationary scattering states, the Hamiltonian can be expanded as

$$H = \sum_n E_n |\psi_n\rangle\langle\phi_n| + \frac{1}{2m} \int_{-\infty}^{\infty} dp p^2 |p^+\rangle\langle\widehat{p}^+|. \tag{32}$$

We call the first and the second terms of (32) the discrete, H_d , and continuous, H_c , parts of the Hamiltonian respectively. A central object is the scattering operator (or matrix), $S \equiv \Omega_-^\dagger \Omega_+$ for scattering processes by H and $\widehat{S} \equiv \widehat{\Omega}_-^\dagger \widehat{\Omega}_+$ for H^\dagger . Unhatted quantities refer to scattering by H , while hatted ($\widehat{}$) quantities refer to scattering by its Hermitian conjugate H^\dagger . The scattering operator gives the probability of an incident state $|\psi_{in}\rangle$ to be scattered (by H or H^\dagger) into a state

	<i>A</i> linear	<i>A</i> antilinear
$AH = HA$	$\begin{aligned} A\Omega_{\pm} &= \Omega_{\pm}A \\ AS &= SA \end{aligned}$	$\begin{aligned} A\Omega_{\pm} &= \widehat{\Omega}_{\mp}A \\ AS &= \widehat{S}^{\dagger}A \end{aligned}$
$AH = H^{\dagger}A$	$\begin{aligned} A\Omega_{\pm} &= \widehat{\Omega}_{\pm}A \\ AS &= \widehat{S}A \end{aligned}$	$\begin{aligned} A\Omega_{\pm} &= \Omega_{\mp}A \\ AS &= S^{\dagger}A \end{aligned}$

TABLE 2: Transformation rules of the Möller and scattering operators under symmetries with linear or antilinear operators.

$|\psi_{out}\rangle$ as $|\langle\psi_{out}|S|\psi_{in}\rangle|^2$ or $\left|\langle\psi_{out}|\widehat{S}|\psi_{in}\rangle\right|^2$. Although the scattering operator is not unitary for NH Hamiltonians, S and \widehat{S} obey the generalized unitarity relations $\widehat{S}^{\dagger}S = S\widehat{S}^{\dagger} = 1$ which collapses to the usual unitarity condition ($S = \widehat{S}$) if $H = H^{\dagger}$. If the Hamiltonian is symmetric or pseudohermitian with respect to a linear/antilinear operator A , the Möller and scattering operators transform according to the intertwining relations in Table 2. The intertwining relations of the Möller operators give the transformation rules for scattering states under A and provide interesting relations between the different transmission/reflection coefficients.

Also relevant to scattering theory is the transition operator, which is defined as

$$T_{op}(E) = V + VG(E)V \quad (33)$$

where $G(E) = (E - H)^{-1}$ is Green's operator. The transition operator satisfies $T_{op}^{\dagger}(z) = \widehat{T}_{op}(z^*)$ and its matrix elements in momentum representation are related to the scattering operator by

$$\langle p|S|p'\rangle = \delta(p - p') - 2i\pi\delta(E_p - E_{p'}) \langle p|T_{op}(+)|p'\rangle, \quad (34)$$

where $T_{op}(\pm)|p'\rangle = \lim_{\epsilon \rightarrow 0^+} T_{op}(E_p \pm i\epsilon)|p'\rangle$. This operator can then be used to define the scattering amplitudes for real p as

$$\begin{aligned} R^l(p) &= -\frac{2\pi im}{p} \langle -p | T_{op}(\text{sign}(p)) | p \rangle, \\ T^l(p) &= 1 - \frac{2\pi im}{p} \langle p | T_{op}(\text{sign}(p)) | p \rangle, \\ R^r(p) &= -\frac{2\pi im}{p} \langle p | T_{op}(\text{sign}(p)) | -p \rangle, \\ T^r(p) &= 1 - \frac{2\pi im}{p} \langle -p | T_{op}(\text{sign}(p)) | -p \rangle, \end{aligned} \quad (35)$$

where $R^{l,r}$ is the left/right reflection amplitude and $T^{l,r}$ is the left/right transmission amplitude. We assume that the amplitudes admit analytic continuations. The generalized unitarity relation of the scattering operators give the following set of equations for the amplitudes

$$\begin{aligned} \hat{T}^l(p)T^{l*}(p) + \hat{R}^l(p)R^{l*}(p) &= 1, \\ \hat{T}^r(p)T^{r*}(p) + \hat{R}^r(p)R^{r*}(p) &= 1, \\ \hat{T}^{l*}(p)R^r(p) + T^r(p)\hat{R}^{l*}(p) &= 0, \\ T^l(p)\hat{R}^{r*}(p) + \hat{T}^{r*}(p)R^l(p) &= 0, \end{aligned} \quad (36)$$

where p is taken to be real and nonnegative. The Dirac deltas in Eq. (34) make clear that the S matrix only connects momentum eigenstates having the same kinetic energy. Factoring out the Dirac delta of energy using $\delta(p - p') = \frac{|p|}{m}\delta(E_p - E_{p'})\delta_{pp'}$ ($\delta_{pp'}$ is to be understood as a Kronecker delta of the signs of the momenta) we can write $\langle p | S | p' \rangle = \frac{|p|}{m}\delta(E_p - E_{p'}) \langle \mathbf{p} | \mathsf{S} | \mathbf{p}' \rangle$ in terms of the two-dimensional vectors $|\mathbf{p}\rangle \equiv (1, 0)^T$ and $|-\mathbf{p}\rangle \equiv (0, 1)^T$ that correspond to the states $|p\rangle$ and $|-p\rangle$ for $p > 0$ [1]. The previous relation defines the on-the-energy-shell S matrix as

$$\begin{aligned} \langle \mathbf{p} | \mathsf{S} | \mathbf{p}' \rangle &= \delta_{pp'} - \frac{2i\pi m}{|p|} \langle p | T_{op}(+) | p' \rangle \\ &\Downarrow \\ \mathsf{S} &= \begin{pmatrix} T^l(p) & R^r(p) \\ R^l(p) & T^r(p) \end{pmatrix}. \end{aligned} \quad (37)$$

$\widehat{\mathsf{S}}$ can be defined similarly. The on-the-energy-shell scattering matrix S inherits the generalized unitarity relation of the scattering operator S , i.e., $\widehat{\mathsf{S}}^\dagger \mathsf{S} = 1$. Equation (36) is just this generalized unitarity relation written for all matrix elements.

.2 Alternative formulation of A -pseudohermitian symmetries as ordinary (commuting) symmetries

Symmetry relations like (3.2) (for A either linear or antilinear) may also be expressed as ordinary (commuting) symmetries, generalizing for scattering Hamiltonians the work in [31, 58, 70]. In other words, for a Hamiltonian H and a linear hermitian (antilinear hermitian) operator A satisfying (3.2) we can find an antilinear (linear) operator B that commutes with H . In this appendix we explicitly construct the operators B from the Hamiltonian both for A linear and antilinear in the first and second sections respectively.

Let us assume for now that besides A (linear or antilinear) there exists an invertible and hermitian antilinear operator τ that also satisfies (3.2). With A and τ let us define the operator $B = A^{-1}\tau$ that will be antilinear (linear) for A linear (antilinear). As defined, B commutes with the Hamiltonian, because

$$\begin{aligned} BH &= A^{-1}\tau H \\ &= A^{-1}H^\dagger\tau \\ &= HA^{-1}\tau \\ &= HB. \end{aligned} \tag{38}$$

B is not generally Hermitian unless τ commutes with A^{-1} .

The main task to define B is to find the antilinear operator τ that satisfies (3.2). This can be achieved if the eigenvectors of the Hamiltonian and its adjoint form bases of the Hilbert space that are biorthonormal. In [58] the expression of τ for a discrete spectrum (with no degeneracy) is found as

$$\tau_d |\zeta\rangle = \sum_n \langle \zeta | \phi_n \rangle |\phi_n\rangle, \tag{39}$$

where the d subscript indicates that the Hamiltonian has a discrete spectrum. The action of the operator in Eq. (39) on a vector in an eigenspace amounts to complex conjugation of its coordinate representation. τ_d is clearly antilinear, Hermitian (for antilinear operators hermicity is defined as $\langle \chi | \tau_d \zeta \rangle = \langle \zeta | \tau_d \chi \rangle$), and invertible. It can be checked that the relation $\tau_d H = H^\dagger \tau_d$ is satisfied.

To generalize this to Hamiltonians whose spectrum includes a continuous part, we have to build an antilinear operator τ that acts in both the subspaces, \mathcal{H}_d and \mathcal{H}_c , that are respectively spanned by the eigenfunctions associated with the discrete (point) and continuous spectra of the Hamiltonian. We propose to take $\tau = \tau_d + \tau_c$. The operators τ_d and τ_c act on complementary subspaces of the Hilbert space: while τ_d maps \mathcal{H}_d to \mathcal{H}_d and annihilates states in \mathcal{H}_c , τ_c maps \mathcal{H}_c to \mathcal{H}_c and annihilates states in \mathcal{H}_d . Specifically, we take τ_d to be given by Eq. (39) with n denoting the eigenvectors of the Hamiltonian associated with the discrete part of the spectrum. To construct τ_c , note that to satisfy $\tau H = H^\dagger \tau$ (Eq. (3.2)) it has to transform right scattering eigenvectors into some linear combination of left scattering eigenvectors in the same energy shell. This is so because

$$H^\dagger \tau |p^+\rangle = \tau H |p^+\rangle = \tau E_p |p^+\rangle = E_p \tau |p^+\rangle. \quad (40)$$

To fulfill the last requirement we set

$$\tau_c |\zeta\rangle = \int_{-\infty}^{\infty} dp [C_+(p) \langle \zeta | \hat{p}^+ \rangle |\hat{p}^+\rangle + C_-(p) \langle \zeta | \hat{p}^+ \rangle |-\hat{p}^+\rangle], \quad (41)$$

where $C_+(p)$ and $C_-(p)$ are complex coefficients. It is straightforward to check that $\tau_c |p^+\rangle = C_+(p) |\hat{p}^+\rangle + C_-(p) |-\hat{p}^+\rangle$. The operator in (41) is clearly antilinear because of the antilinearity of the inner product with respect to its first argument. Hermicity of τ requires $C_-(p) = C_-(-p)$. The condition that τ must be invertible restricts the coefficients in Eq. (41) further. Consider the *on shell* representation of τ_c , $\langle p^+ | \tau q^+ \rangle = \frac{|p|}{m} \delta(E_p - E_q) \mathsf{C}_{p,q}$, with $\mathsf{C}_{p,q} \equiv \delta_{p,q} C_+(q) + \delta_{p,-q} C_-(q)$, or in matrix form

$$\mathsf{C}(p) = \begin{pmatrix} C_+(p) & C_-(p) \\ C_-(p) & C_+(-p) \end{pmatrix}. \quad (42)$$

Since τ has to be invertible, $\mathsf{C}(p)$ must be invertible as well. This implies $C_+(p)C_+(-p) - C_-(p)C_-(p) \neq 0$.

In the following sections we construct expressions for B , in section 1 for A linear, and in section 2 for A antilinear.

2.1 Pseudohermicity with linear operators

In [31, 58, 70] it is shown that pseudohermitian Hamiltonians, i.e. those satisfying (3.2) for $A = \eta$ with η a hermitian and invertible linear operator, posses

an energy spectrum whose complex eigenvalues come in complex-conjugate pairs. Moreover the eigenspaces associated with the eigenvalues E and E^* have the same degeneracy and η maps one to the other. Conversely, if the complex part of the spectrum of H contains only complex-conjugate pairs, it can be shown that there exists an η for which the Hamiltonian satisfies (3.2). These results hold for a general class of diagonalizable Hamiltonians with a discrete spectrum. For these Hamiltonians we can identify η with

$$\begin{aligned}\eta_d = & \sum_{n_0} |\phi_{n_0}\rangle\langle\phi_{n_0}| \\ & + \sum_n \left[|\phi_{n_-}\rangle\langle\phi_{n_+}| + |\phi_{n_+}\rangle\langle\phi_{n_-}| \right],\end{aligned}\tag{43}$$

where the states $|\psi_{n_0}\rangle$ ($|\phi_{n_0}\rangle$) correspond to the right (left) eigenstates of H with real energy E_{n_0} . $|\psi_{n_+/n_-}\rangle$ (respectively $|\phi_{n_+/n_-}\rangle$) correspond to the right (respectively left) eigenvectors whose eigenvalue E_{n_+/n_-} has a positive/negative imaginary part. This gives $\eta_d |\psi_{n_0}\rangle = |\phi_{n_0}\rangle$, $\eta_d |\psi_{n_+}\rangle = |\phi_{n_-}\rangle$ and $\eta_d |\psi_{n_-}\rangle = |\phi_{n_+}\rangle$. Clearly η_d is compatible with pseudohermicity since it maps right eigenvectors associated with the eigenvalue E into left eigenvectors with eigenvalue E^* and the pseudohermicity relation (3.2) is satisfied. To generalize (43) for a scattering Hamiltonian we must add an additional term η_c which acts on the subspace of scattering states and is compatible with the hermiticity and invertibility of $\eta = \eta_d + \eta_c$. Since η should transform the right scattering states into left ones in the same energy shell, $\eta_c |p^+\rangle$ should be a linear combination of both $|\hat{p}^+\rangle$ and $|-\hat{p}^+\rangle$. Accordingly, we propose

$$\eta_c = \int_{-\infty}^{\infty} dp \left[\Lambda_+(p) |\hat{p}^+\rangle\langle\hat{p}^+| + \Lambda_-(p) |-\hat{p}^+\rangle\langle\hat{p}^+| \right],\tag{44}$$

where $\Lambda_+(p), \Lambda_-(p)$ are complex coefficients depending on the momentum p . Hermiticity of η requires $\Lambda_+(p) \in \mathbb{R}$ and $\Lambda_-^*(p) = \Lambda_-(-p)$.

Since η_c connects scattering states with the same energy it admits the following *on-shell* representation, $\langle q^+ | \eta_c | p^+ \rangle = \frac{|p|}{m} \delta(E_q - E_p) \Lambda_{q,p}(p)$, with $\Lambda_{q,p}(p) \equiv \delta_{q,p} \Lambda_+(p) + \delta_{q,-p} \Lambda_-(p)$, or in matrix form

$$\Lambda(p) = \begin{pmatrix} \Lambda_+(p) & \Lambda_-^*(p) \\ \Lambda_-(p) & \Lambda_+(-p) \end{pmatrix}.\tag{45}$$

Since η has to be invertible, this implies that the determinant of $\Lambda(p)$ should not

vanish i.e. $\Lambda_+(p)\Lambda_+(-p) - \Lambda_-(p)\Lambda_-^*(p) \neq 0$. The inverse of η is then $\eta^{-1} = \eta_d^{-1} + \eta_c^{-1}$ with

$$\begin{aligned}\eta_d^{-1} &= \sum_{n_0} |\psi_{n_0}\rangle\langle\psi_{n_0}| \\ &\quad + \sum_n [|\psi_{n_+}\rangle\langle\psi_{n_-}| + |\psi_{n_-}\rangle\langle\psi_{n_+}|]\end{aligned}\tag{46}$$

$$\eta_c^{-1} = \int_{-\infty}^{\infty} dp \left[\Lambda_+^{(-1)}(p) |p^+\rangle\langle p^+| + \Lambda_-^{(-1)}(p) |-p^+\rangle\langle p^+| \right],\tag{47}$$

where the complex coefficients $\Lambda_{\pm}^{(-1)}(p)$ are taken from the inverse of $\Lambda(p)$

$$\Lambda^{-1}(p) = \begin{pmatrix} \Lambda_+^{(-1)}(p) & \Lambda_-^{(-1)*}(p) \\ \Lambda_-^{(-1)}(p) & \Lambda_+^{(-1)}(-p) \end{pmatrix}.\tag{48}$$

Using the orthogonality between the subspace of discrete (bound) and scattering states we find the final expression for B

$$\begin{aligned}B |\zeta\rangle &= \eta_d^{-1} \tau_d |\zeta\rangle + \eta_c^{-1} \tau_c |\zeta\rangle \\ &= \sum_{n_0} \langle \zeta | \phi_{n_0} \rangle |\psi_{n_0}\rangle + \sum_n \langle \zeta | \phi_{n_+} \rangle |\psi_{n_-}\rangle + \sum_n \langle \zeta | \phi_{n_-} \rangle |\psi_{n_+}\rangle \\ &\quad + \int_{-\infty}^{\infty} dp \langle \zeta | \hat{p}^+ \rangle \left[\tilde{C}_+(p) |p^+\rangle + \tilde{C}_-(p) |-p^+\rangle \right],\end{aligned}\tag{49}$$

with $\tilde{C}_{\pm}(p) = C_+(p)\Lambda_{\pm}^{(-1)}(p) + C_-(p)\Lambda_{\mp}^{(-1)}(-p)$. Note that the resulting operator B is antilinear.

2.2 Pseudohermicity with antilinear operators

In this section we will consider the case where the operator A appearing in Eq. (3.2) is antilinear. In ref. [58] this is called antipseudohermicity, but we will not use this terminology in order to avoid confusion with antihermicity ($H = -H^\dagger$). The effect of A on a right eigenvector of H is to transform it into its corresponding

biorthonormal partner, i.e. the left eigenvector corresponding to the same energy

$$\begin{aligned} H^\dagger A |\psi_n\rangle = AH |\psi_n\rangle &= AE_n |\psi_n\rangle = E_n^* A |\psi_n\rangle \\ &\Downarrow \\ A |\psi_n\rangle &\propto |\phi_n\rangle. \end{aligned} \quad (50)$$

A also admits a decomposition similar to Eq. (39). The Hamiltonian satisfies Eq. (3.2) with respect to τ . One can check that $A^{-1}\tau$ is a linear symmetry of the Hamiltonian, $HA^{-1}\tau - A^{-1}\tau H = 0$. The expansion of A on the discrete and scattering basis is

$$A |\xi\rangle = \sum_n g_n \langle \xi | \phi_n \rangle |\phi_n\rangle + \int dp \langle \xi | \hat{p}^+ \rangle [G_+(p) |\hat{p}^+\rangle + G_-(p) |-\hat{p}^+\rangle], \quad (51)$$

with $A |p^+\rangle = G_+(p) |\hat{p}^+\rangle + G_-(p) |-\hat{p}^+\rangle$ and $g_n = \langle \psi_n | A \psi_n \rangle$. As examples we have found the expressions of $B = A^{-1}\tau$ for $A_T = \Theta$ (time reversal) and $A_{PT} = \Pi\Theta$ (PT). In both cases we have $A_T^{-1} = A_T$ and $A_{PT}^{-1} = A_{PT}$.

.2.2.1 PT Symmetry

The action of $B_{PT} = A_{PT}\tau$ on an arbitrary state is

$$B_{PT} |\zeta\rangle = A_{PT}\tau |\zeta\rangle = A_{PT} \left\{ \sum_n \langle \zeta | \phi_n \rangle |\phi_n\rangle + \int dp [C_+(p) \langle \zeta | \hat{p}^+ \rangle |\hat{p}^+\rangle + C_-(p) \langle \zeta | \hat{p}^+ \rangle |-\hat{p}^+\rangle] \right\}. \quad (52)$$

Using $A_{PT}H = H^\dagger A_{PT}$ and table 2 we have $A_{PT} |\hat{p}^\pm\rangle = |\hat{p}^\mp\rangle$. Note that The “-” right scattering states can be expressed in terms of the “+” right scattering

states as

$$\begin{aligned}
|\widehat{p}^-\rangle &= \int dq |q^+\rangle \langle \widehat{q}^+| \widehat{p}^-\rangle \\
&= \int dq |q^+\rangle \langle q| \widehat{\Omega}_+^\dagger \widehat{\Omega}_- |p\rangle \\
&= \int dq |q^+\rangle \langle q| \widehat{S}^\dagger |p\rangle \\
&= |p^+\rangle \langle p| \widehat{S}^\dagger |p\rangle + |-p^+\rangle \langle -p| \widehat{S}^\dagger |p\rangle.
\end{aligned} \tag{53}$$

With all this, the final form of B_{PT} is

$$\begin{aligned}
B_{PT} &= \sum_n (g_n^*)^{-1} |\psi_n\rangle \langle \phi_n| \\
&+ \int dp \left[\tilde{C}_+^*(p) |p^+\rangle \langle \widehat{p}^+| + \tilde{C}_-^*(p) |-p^+\rangle \langle \widehat{p}^+| \right],
\end{aligned} \tag{54}$$

with $C_\pm^*(p) = C_\pm^*(p) \langle \pm p| \widehat{S}^\dagger | \pm p\rangle + C_\mp^*(p) \langle \pm p| \widehat{S}^\dagger | \mp p\rangle$.

2.2.2 Time-Reversal Symmetry

For time-reversal symmetry,

$$B_T |\zeta\rangle = A_T \tau |\zeta\rangle = A_T \left\{ \sum_n \langle \zeta| \phi_n \rangle |\phi_n\rangle + \int dp \left[C_+(p) \langle \zeta| \widehat{p}^+ \rangle | \widehat{p}^+\rangle + C_-(p) \langle \zeta| \widehat{p}^+ \rangle | -\widehat{p}^+\rangle \right] \right\}. \tag{55}$$

Since the time-reversal operator satisfies the relation (3.2) with the Hamiltonian, Table 2 implies $A_T |\widehat{p}^\pm\rangle = |-\widehat{p}^\mp\rangle$. The linear symmetry operator can be expressed as in Eq. (54) but in this case $\tilde{C}_\pm^*(p) = C_\pm^*(p) \langle \pm p| \widehat{S}^\dagger | \mp p\rangle + C_\mp^*(p) \langle \pm p| \widehat{S}^\dagger | \pm p\rangle$.

.3 Properties of separable potentials

.3.1 Transition operator

For a separable potential $V = V_0 |\phi\rangle\langle\chi|$, the transition operator becomes

$$T_{op} = \alpha |\phi\rangle\langle\chi| \quad (56)$$

where $\alpha = V_0 + V_0^2 \langle\chi| G(E) |\phi\rangle$. Then using the Lippmann-Schwinger equation we get that

$$\begin{aligned} T_{op}(E) &= V + VG_0(E)T_{op}(E) \\ &= [V_0 + \alpha V_0 \langle\chi| G_0(E) |\phi\rangle] |\phi\rangle\langle\chi| \end{aligned} \quad (57)$$

where $G_0(E) = (E - H_0)^{-1}$ is the Green's operator for free motion. Solving for α now gives

$$\alpha = \frac{V_0}{1 - V_0 \langle\chi| G_0(E) |\phi\rangle} = \frac{V_0}{1 - V_0 Q_0(E)}. \quad (58)$$

.3.2 S-matrix eigenvalues

The eigenvalues for the S-matrix are given by Eq. (3.12) in terms of the reflection and transmission amplitudes. For a separable potential, using Eq. (35), we can simplify the transmission and reflection coefficients as

$$\begin{aligned} T^l &= 1 - \frac{2\pi im}{p} \alpha \phi(p) \chi^*(p), \\ T^r &= 1 - \frac{2\pi im}{p} \alpha \phi(-p) \chi^*(-p), \\ R^l &= -\frac{2\pi im}{p} \alpha \phi(-p) \chi^*(p), \\ R^r &= -\frac{2\pi im}{p} \alpha \phi(p) \chi^*(-p). \end{aligned} \quad (59)$$

If we now define

$$\Gamma = \frac{2\pi im}{p} \alpha [\phi(p) \chi^*(p) + \phi(-p) \chi^*(-p)], \quad (60)$$

we can write the eigenvalues as simply

$$S_j = 1 - \frac{\Gamma - (-1)^j \Gamma}{2}. \quad (61)$$

Note that $S_2 = 1$ for all p . Clearly the following relation must also always hold for the reflection and transmission amplitudes,

$$T^l + T^r - T^l T^r + R^l R^r = 1. \quad (62)$$

.3.3 Uniqueness of bound state

A separable potential can only have at most one bound state $|\psi_E\rangle$. In momentum representation,

$$\begin{aligned} \langle p | \psi_E \rangle &= \langle p | \frac{V_0}{E - H_0} |\phi\rangle \langle \chi | \psi_E \rangle \\ &= \frac{M}{p^2 - q_B^2} \langle p | \phi \rangle, \end{aligned} \quad (63)$$

where $M = -2mV_0 \langle \chi | \psi_E \rangle$ and $q_B^2 = 2mE < 0$. Suppose there is a second bound state $|\psi_{E'}\rangle$, with corresponding quantities M' and $q_{B'}^2$. Then,

$$\langle \psi_{E'} | \psi_E \rangle = MM' \int_{-\infty}^{\infty} dp |\langle p | \phi \rangle| \frac{1}{p^2 - q_B^2} \frac{1}{p^2 - q_{B'}^2}. \quad (64)$$

Since $MM' \neq 0$ and the integral is positive the overlap cannot be zero so there cannot be two bound states.

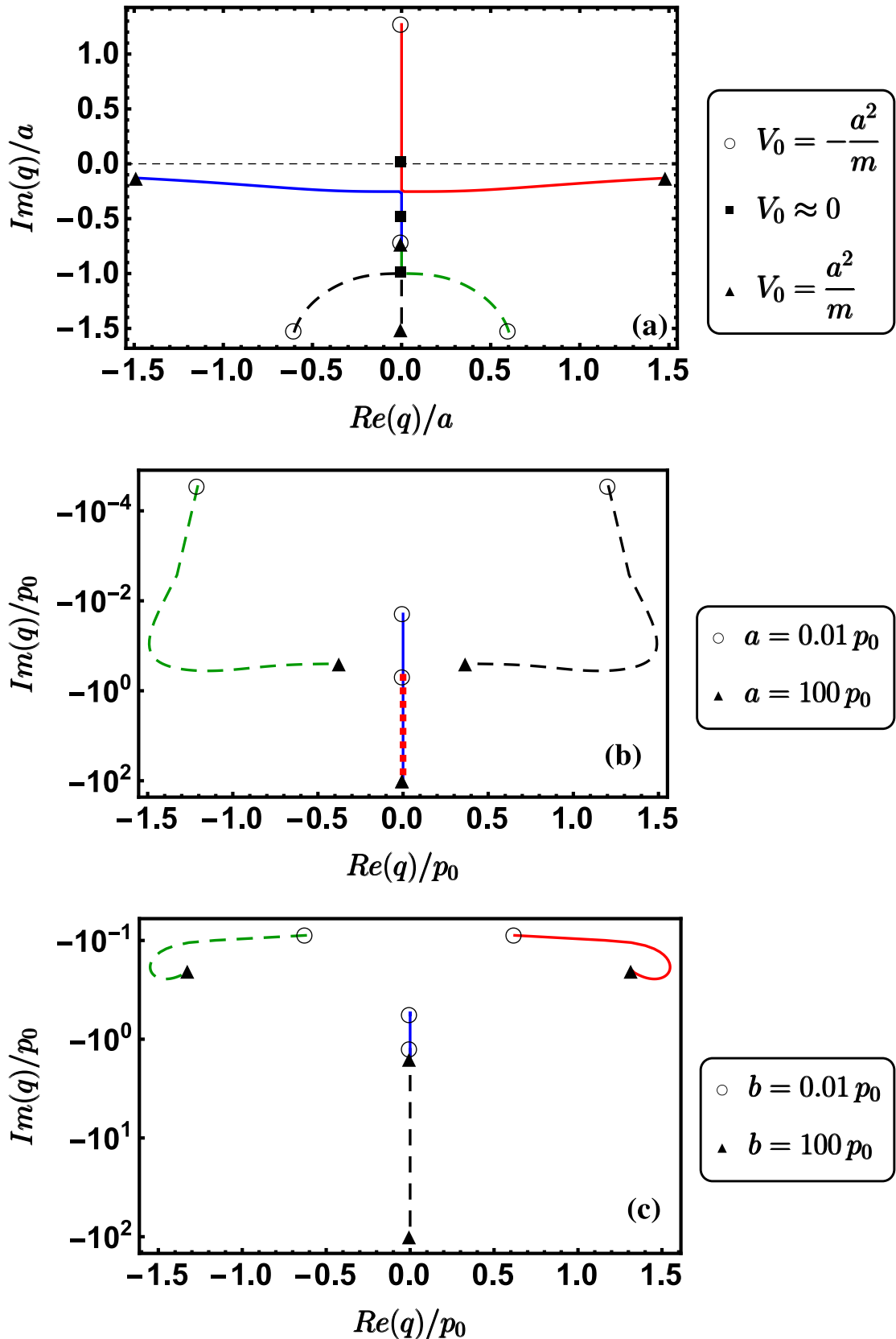


FIGURE 3.2: (Color online) Poles and pole trajectories of time-reversal symmetric potential (3.24) for (a) varying V_0 with $a = 2b$; (b) varying a with $b = 0.5 p_0$, $V_0 > 0$; and (c) varying b with $a = p_0$, $V_0 > 0$. At pole collisions we connect each of the incoming trajectories with a different emerging trajectory but the choice of outgoing branch is arbitrary since the two colliding poles lose their identity.

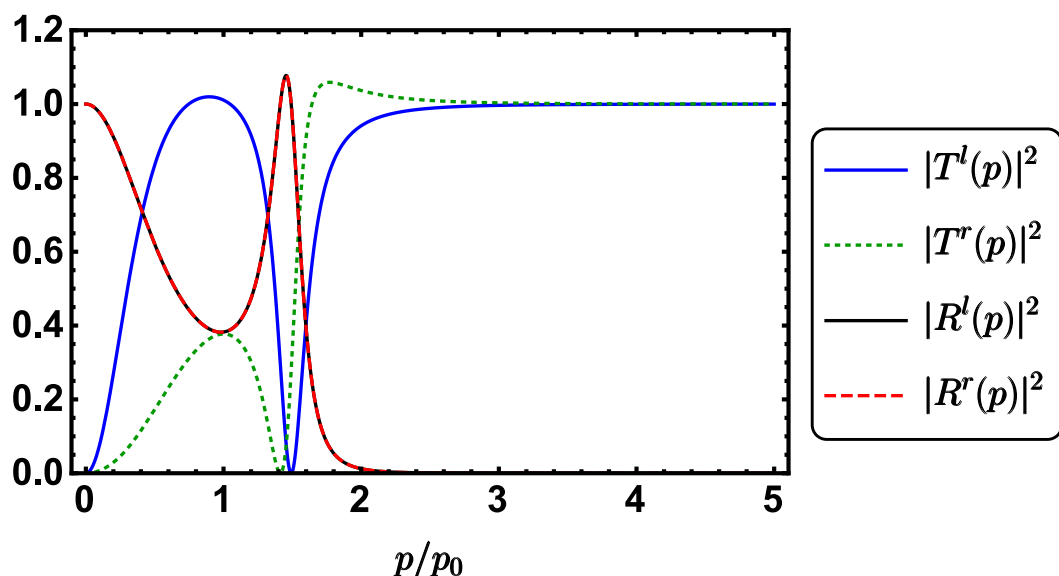


FIGURE 3.3: (Color online) Transmission and reflection coefficients of the time-reversal symmetric potential (3.24) with $a = p_0$, $b = 0.5 p_0$ and $V_0 > 0$.

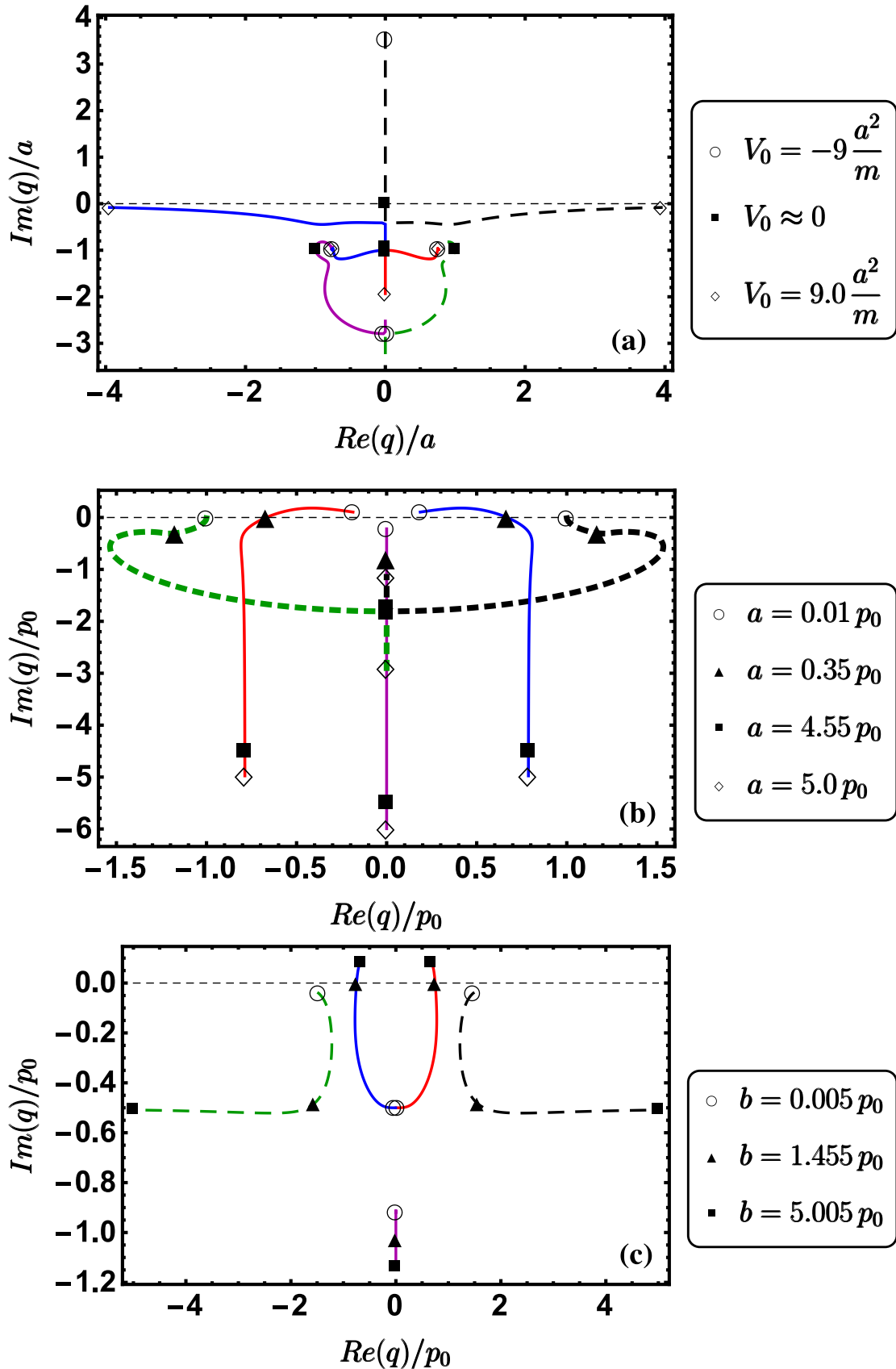


FIGURE 3.4: (Color online) Poles and pole trajectories for the parity pseudo-hermitian potential (3.28) (a) varying V_0 with $a = b$; (b) varying a with $b = p_0$, $V_0 > 0$; (c) varying b with $a = 0.5 p_0$, $V_0 > 0$.

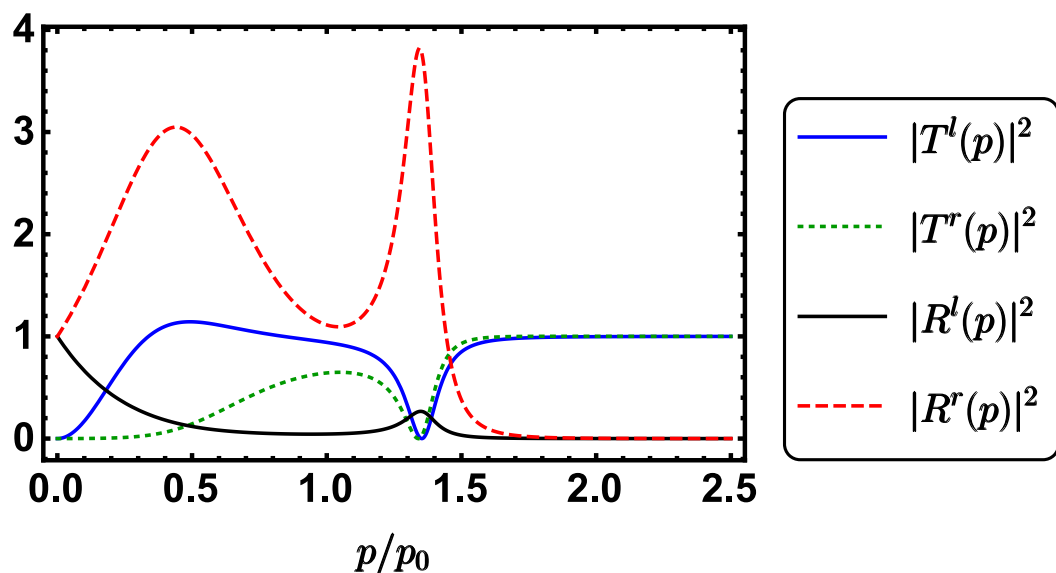


FIGURE 3.5: (Color online) Transmission and reflection coefficients for $a = b = 0.5 p_0$ and $V_0 > 0$.

Appendix A

Local rectification of heat flux

We present a chain-of-atoms model where heat is rectified, with different fluxes from the hot to the cold baths located at the chain boundaries when the temperature bias is reversed. The chain is homogeneous except for boundary effects and a local modification of the interactions at one site, the “impurity”. The rectification mechanism is due here to the localized impurity, the only asymmetrical element of the structure, apart from the externally imposed temperature bias, and does not rely on putting in contact different materials or other known mechanisms such as grading or long-range interactions. The effect survives if all interaction forces are linear except the ones for the impurity.

A.1 Introduction

In spite of much work on thermal rectification after the first model proposal in 2002 [71] (for a broad perspective on heat rectification see [72, 73]), the manipulation of phononic heat fluxes is still far from being completely controlled as no efficient and feasible thermal diodes have been found [74, 75]. The thermal rectifier, a device where the heat current changes when the temperature bias of the thermal baths at the boundaries is reversed, is one of the key tools needed to manipulate heat currents and build thermal circuits. A wealth of research is underway to meet the challenge posed by a “near standstill” of the field [74, 75], combined with the prospects of widespread and impactful practical applications. Together with experimental progress, at this stage work exploring new models is important to test possibilities that may become feasible as control capabilities improve [72]. In this paper we propose, motivated by previous work on “atom diodes” [37, 76], a rectifying scheme based on the effect of a local defect, or impurity, in an otherwise homogeneous system.

To date, there have been several proposals of systems that could be used to rectify heat flows at the nanoscale. A common scheme is based on coupling two or more different homogeneous segments, modelled with chains of atoms with non-linear interactions (which in this context means non-linear forces, i.e., anharmonic potentials) [71, 77–80] or with a temperature and position dependent conductivity assuming expressions for the heat current [79, 81]. Basic ingredients for thermal rectification have been considered to be the asymmetry in the system and non-linear interactions [73, 80, 82], which lead to a temperature dependence of the phonon bands, or power spectral densities, of the weakly coupled [78] segments. These bands match or mismatch at the interfaces, depending of the sign of the temperature bias, leading, respectively, to heat flow or insulating conditions. In fact, alternative mechanisms due to band mixing appear for stronger coupling or long chains [78], and Pereira [75], based on minimalist models, has recently reformulated the conditions leading to rectification as the combination of asymmetry plus the existence of some feature of the system that depends on the temperature (nonlinearity is certainly a possible cause of such dependence). Other systems proposed are graded materials, such as a chain with an uneven distribution of mass [74, 82, 83], and long-range interactions have been shown to be able to amplify the rectification and avoid or mitigate the decay of the effect with system size [74, 84]. Also, recent models and experiments use asymmetrical homogeneous or

inhomogeneous nanostructures and, in particular, graphene [85, 86]. Finally, we mention for completeness theoretical works that consider the use of a quantum system [72], such as a three-level system, with each level coupled to a thermal bath [87], or a double well with different frequencies to implement the asymmetry [88].

The model proposed in this paper is a one-dimensional chain of atoms where all, except one of them, are trapped in on-site harmonic potentials and interact with their nearest neighbours by Morse potentials (or also by harmonic potentials in a simplified version). Unlike most chain models, the structural asymmetry is, except for the boundaries, only in the impurity, which is subjected to a different on-site potential and interaction with one of its neighbors. The chain is connected to thermal baths at different temperatures at the boundaries. Let us clarify our terminology: The structural asymmetry we have in mind amounts, to different interaction potentials of one or several atoms in the chain (other than the boundary atoms) with neighbors on the right and on the left, and/or asymmetric onsite potentials. In this regard chains with Morse interatomic potentials per se are not considered structurally asymmetric here as long as their parameters are the same on both sides of a given atom, even if a single Morse potential is obviously asymmetric with respect to its minimum [89].

First, we shall describe the homogeneous 1D chain, without the impurity, and show its heat conduction behavior. Then we modify the potentials for one of the atoms and demonstrate the rectification effect.

A.2 Homogeneous one-dimensional chain

We start with a homogeneous 1D chain with N atoms coupled at both extremes to heat baths, at different temperatures T_h and T_c for “hot” and “cold” respectively. The baths are modeled with a Nosé-Hoover method as described in [90]. Atoms 1 and N represent the first and the N -th atom in the chain, from left to right, that will be in contact with the baths. All the atoms are subjected to on-site potentials and to nearest-neighbor interactions, and their equilibrium positions y_{i0} are assumed to be equally spaced by a distance a . $x_i = y_i - y_{i0}$, $i = 1, \dots, N$, represent the displacements from the equilibrium positions of the corresponding atoms with positions y_i .

The classical Hamiltonian of the atom chain can be written in a general form as

$$H = \sum_{i=1}^N H_i, \quad (\text{A.1})$$

with

$$\begin{aligned} H_1 &= \frac{p_1^2}{2m} + U_1(x_1) + V_L, \\ H_i &= \frac{p_i^2}{2m} + U_i(x_i) + V_i(x_{i-1}, x_i) \quad i = 2, \dots, N-1, \\ H_N &= \frac{p_N^2}{2m} + U_N(x_N) + V_N(x_{N-1}, x_N) + V_R, \end{aligned} \quad (\text{A.2})$$

where the p_i are the momenta, $U_i(x_i)$ is the on-site potential for the i th atom, and $V_i(x_{i-1}, x_i)$ represents the atom-atom interaction potential. V_R and V_L are the interactions coupling the boundary atoms to the Nosé-Hoover thermostats, see [90].

There are a large number of 1D models that obey this general Hamiltonian. Using different potentials for the trapping and interactions we would get different conductivity behaviors. We choose a simple form of the Hamiltonian in which each atom is subjected to a harmonic on-site potential and a Morse interaction potential between nearest neighbors (see fig. A.1, dashed lines),

$$U_i(x_i) = \frac{1}{2}m\omega^2 x_i^2, \quad (\text{A.3})$$

$$V_i(x_{i-1}, x_i) = D \left\{ e^{-\alpha[x_i - x_{i-1}]} - 1 \right\}^2, \quad (\text{A.4})$$

where ω is the trapping angular frequency, and D and α are time independent parameters of the Morse potential. A “minimalist version” of the model where V becomes the harmonic limit of eq. (A.4), dotted line in fig. 1, will also be considered in the final discussion,

$$V_i(x_{i-1}, x_i) = k(x_i - x_{i-1})^2/2, \quad k = 2D\alpha^2. \quad (\text{A.5})$$

For convenience, dimensionless units are used and the mass of all particles is set to unity.

We start by studying the homogeneous configuration with no impurity and potentials (A.3) and (A.4), solving numerically the dynamical equations for the Hamiltonian (A.1) with a Runge-Kutta-Fehlberg algorithm. We have chosen a

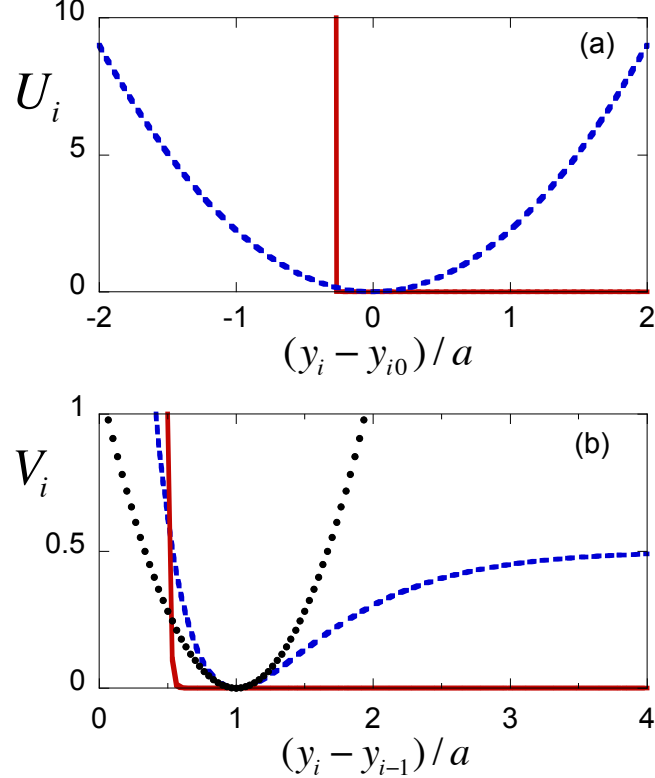


FIGURE A.1: (Color online) (a) On-site potentials: harmonic potential centered at the equilibrium position of each atom (dashed blue line) as a function of the displacement from this position $x_i = y_i - y_{i0}$ in a -units, and the on-site potential for the impurity, $i = N/2 + 1$ (N even, red solid line). (b) Interaction potentials as a function of the distance between nearest neighbors: Morse potential (blue dashed line) valid for all atoms except for $i = N/2 + 1$, N even, where the modified potential (red solid line) is used. The harmonic approximation of the Morse potential is also depicted (eq. (A.5), black dots, only used for fig. 5, below). Parameters: $D = 0.5$, $g = 1$, $\gamma = 45$, $d = 100$ and $b = 105$, used throughout the paper.

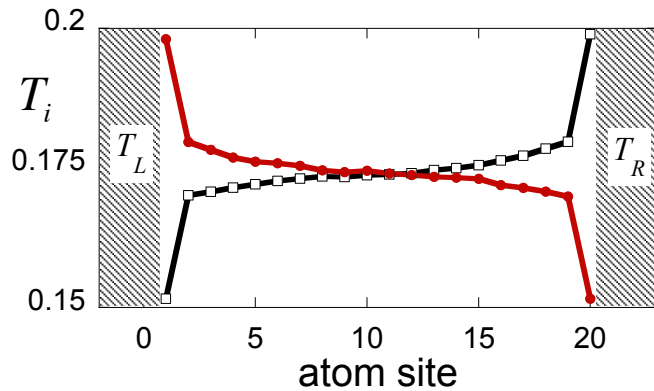


FIGURE A.2: (Color online) Symmetric temperature profiles for a homogeneous chain, without impurity. For $T_h = T_L$, $T_c = T_R$ (red solid dots) the (absolute value of) the heat flux is $J_{L \rightarrow R}$, equal to $J_{R \rightarrow L}$ for the reverse configuration of the bath temperatures, $T_h = T_R$, $T_c = T_L$ (black empty squares). Parameters as in fig. 1.

low number of atoms, $N = 20$, with thermal baths at $T_h = 0.20$ and $T_c = 0.15$ at both ends of the chain with 16 thermostats each. The real temperature is related to the dimensionless one through $T_{real} = T m a^2 \omega^2 / k_B$ so, for typical values $m \approx 10^{-26}$ kg, $\omega \approx 10^{13}$ s $^{-1}$, $a \approx 10^{-10}$ m, and using $k_B = 1.38 \times 10^{-23}$ JK $^{-1}$, the dimensionless temperatures 0.15, 0.20, translate into 100, 150 K. It is advisable to use temperatures around these values so that we ensure that the displacements of the particles are realistic [91].

First we demonstrate the conductivity behavior of the model. To this end, we calculate the local heat flux J_i and temperature T_i , performing the numerical integration for long enough times to reach the stationary state. The local temperature is found as the time average $T_i = \langle p_i^2 / m \rangle$, whereas J_i , from the continuity equation [92], is given by

$$J_i = -\dot{x}_i \frac{\partial V(x_{i-1}, x_i)}{\partial x_i}. \quad (\text{A.6})$$

From now on we only consider the time average $\langle J_i(t) \rangle$, which converges to a constant value for all sites once the system is in the stationary nonequilibrium state. We depict the temperature profiles, for $N = 20$, first with $T_L = T_h$ and $T_R = T_c$ (L and R stand for left and right) and after switching the positions of the thermal baths in fig. A.2. The profiles are symmetric, as expected, and the heat flux does not have a preferred direction [71, 92]. Denoting the absolute values of the fluxes from the left (when $T_L = T_h$) as $J_{L \rightarrow R}$, and from the right (when $T_R = T_h$) as $J_{R \rightarrow L}$, we find that $J_{L \rightarrow R} = J_{R \rightarrow L} = J = 1.6 \times 10^{-2}$, in the dimensionless units, consistent with the values found in other models [71, 92].

The profile of the temperature is linear with boundary nonlinearities at the edges, close to the thermal baths, due to the boundary conditions [93]. In fig. A.3 we depict T_i vs i/N for $N = 100, 125$ and 150 with the same boundary conditions. For these larger atom numbers we have connected the first 3 and the last 3 atoms to the Nosé-Hoover baths. In the inset (a) of fig. A.3 the product JN is plotted vs. N showing that in a low N limit there is a well defined conductivity per unit length whereas for longer chains, JN tends to be constant which indicates a normal thermal conductivity independent of the length. Fixing the number of atoms to 100, as in the inset (b) of fig. A.3, we observe a linear dependence between the flux and ΔT .

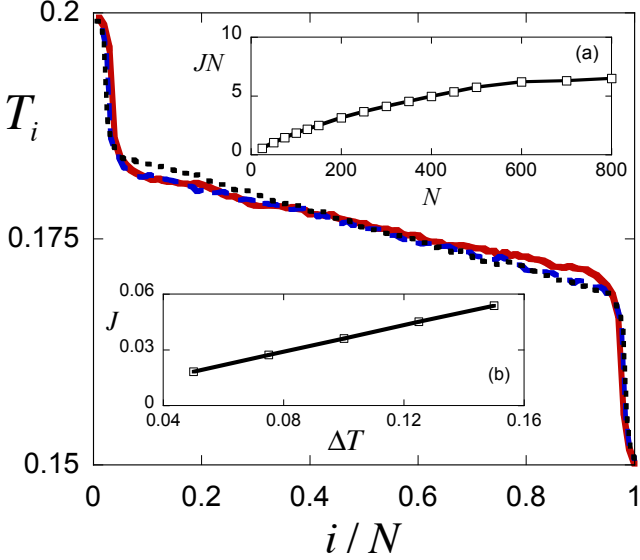


FIGURE A.3: (Color online) Temperature profile along the homogeneous chain for different number of atoms: 100 (dotted black line), 125 (dashed blue line) and 150 (solid red line). The atom sites have been rescaled with the total number of atoms. The time averages have been carried over a time interval of $\approx 2 \times 10^6$ after a transient of $\approx 1 \times 10^5$. In the inset (a), the product JN vs. N demonstrates that for long chains JN is independent of N . In (b) the linear dependence of J with ΔT for a fixed number of atoms, $N = 100$, is shown. Parameters as in fig. 1.

A.3 Impurity-based thermal rectifier

To rectify the heat flux we modify the potentials for site $j = N/2 + 1$ with N even, as

$$U_j(x_j, t) = de^{-b[x_j(t)+a/3]}, \quad (\text{A.7})$$

$$V_j(x_{j-1}, x_j, t) = ge^{-\gamma[x_j(t)-x_{j-1}(t)+a/2]}. \quad (\text{A.8})$$

All the parameters involved, d, b , and g, γ are time independent. In fig. A.1 the modifications introduced with respect to the ordinary sites are shown (solid lines). The different on-site and interaction terms introduce soft-wall potentials (instead of hard-walls to aid integrating the dynamical equations) that make it difficult for the impurity to transmit its excitation to the left whereas left-to-right transmission is still possible. This effect is facilitated by the relative size of the coefficients, $a/3 < a/2$, that determine the position of the walls. These positions imply that an impurity excited by a hot right bath cannot affect its left cold neighbour near its equilibrium position at the $j - 1$ site. However, if the left $j - 1$ atom is excited

from a hot bath on the left, it can get close enough to the impurity to kick it and transfer kinetic energy. The asymmetrical behavior relies on the asymmetry of the potentials and the temperatures of neighboring atoms; it does not require breaking time-reversal invariance. All collisions are elastic and time reversible.

After extensive numerical simulations, we have chosen the values of these parameters as in fig. 1, such that the conductivity in the forward direction, $J_{L \rightarrow R}$, and the rectification factor, defined as $R = (J_{L \rightarrow R} - J_{R \rightarrow L})/J_{R \rightarrow L} \times 100$, are both large for $T_h = 0.2$, $T_c = 0.15$. A large R without a large $J_{L \rightarrow R}$ could in fact be useless [72]. Note that the parameters are not necessarily the optimal combination, which in any case would depend on the exact definition of “optimal” (technically on how $J_{L \rightarrow R}/J$ and R are weighted and combined in a cost function and on the limits imposed on the parameter values). This definition is an interesting question but it goes beyond the focus of our paper, which is to demonstrate and discuss the effect of the localized impurity.

We have used again $N = 20$ connected to baths of 16 thermostats each, with the same temperatures as for the homogeneous chain, and numerically solved the dynamical equations to calculate the local temperature and the heat flux for both configurations of the baths. The interatomic potential for the regular atoms is the Morse potential (A.4). In fig. A.4(a), the temperature profiles show a clear asymmetry between $L \rightarrow R$ and $R \rightarrow L$. Specifically, we find $J_{L \rightarrow R} = 7.6 \times 10^{-3}$ and $J_{R \rightarrow L} = 5.8 \times 10^{-3}$ which gives $R = 31\%$. The effect decays with longer chains, with, for example, $R = 19\%$ for $N = 100$, and $R = 17.8\%$ for $N = 150$.

These temperature profiles depend on the difference between the bath temperatures, see e.g. fig. A.4(b). Increasing the temperature gap, but keeping T_h low enough so that the displacement of the atoms from their equilibrium positions is realistic, we find higher values of R . Figure A.5 shows the strong dependence of R with ΔT (black circles). We have changed both T_h and T_c so that the mean temperature $(T_c + T_h)/2$ remains constant.

A.4 Discussion

We have presented a scheme for thermal rectification using a one-dimensional chain of atoms which is homogeneous except for the special interactions of one of them, the impurity, and the couplings with the baths at the boundaries. Our

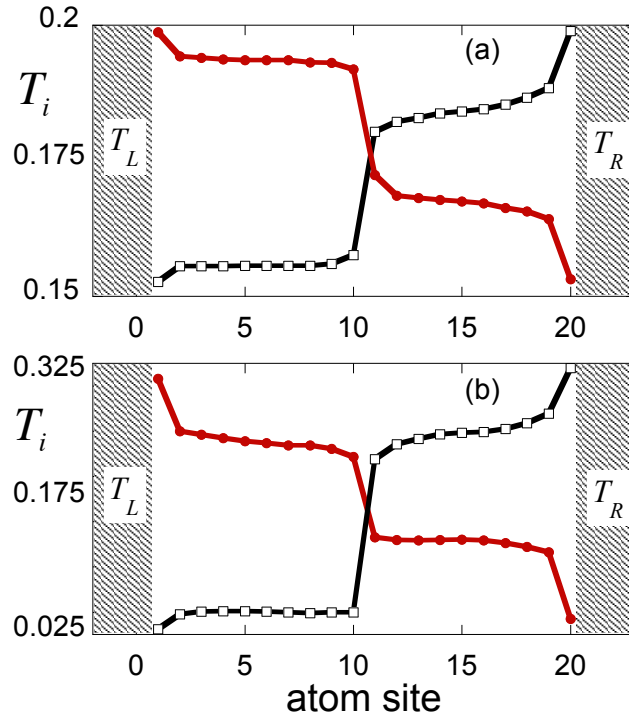


FIGURE A.4: (Color online) Temperature profile for the chain of $N = 20$ atoms, with an impurity in the $N/2 + 1$ position, with $T_L = T_h$ and $T_R = T_c$ (circles) and with the thermostat baths switched (squares). Parameters as in fig. 1. (a) $T_c = 0.15$, $T_h = 0.2$. $J_{L \rightarrow R} = 0.00769$ vs $J_{R \rightarrow L} = 0.00581$, with gives a rectification $R = 31\%$; (b) $T_c = 0.025$, $T_h = 0.325$. $J_{L \rightarrow R} = 0.0499$ vs $J_{R \rightarrow L} = 0.0140$, with $R = 256\%$.

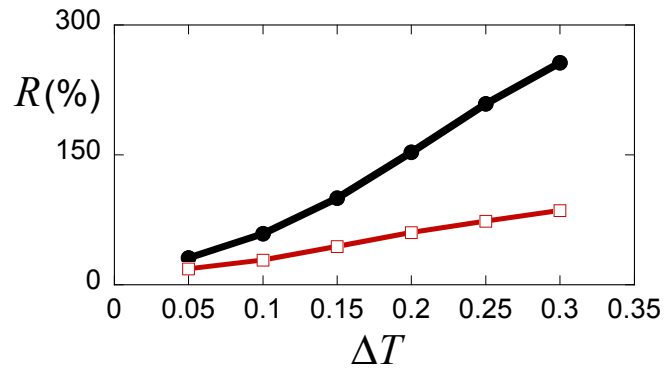


FIGURE A.5: (Color online) Rectification factor R as a function of the temperature difference between ends of the chain of atoms, ΔT . We have changed both T_h and T_c according to $T_c = 0.15 - (\Delta T - 0.05)/2$ and $T_h = 0.2 + (\Delta T - 0.05)/2$, with $N = 20$, keeping the rest of parameters as in fig. A.1. Interatomic potentials: Morse potential, eq. (A.4) (black line with circles, see the temperature profiles of extreme points in fig. 4); harmonic potential, eq. (A.5) (red line with squares).

proof-of-principle results for an impurity-based rectification mechanism encourage further exploration of the impurity-based rectification, in particular of the effect of different forms for the impurity on-site potential and its interactions with neighboring atoms. In contrast to the majority of chain models, the structural asymmetry in our model is only in the impurity. The idea of a localized effect was already implicit in early works on a two-segment Frenkel-Kontorova model [77, 78], where rectification depended crucially on the interaction constant coupling between the two segments. However, the coupling interaction was symmetrical and the asymmetry was provided by the different nature (parameters) of the segments put in contact. Also different from common chain models are the potentials chosen here. Instead of using the Morse potential as an on-site model, see e.g. [71], we have considered a natural setting where this potential characterizes the interatomic interactions, and the on-site potential is symmetrical with respect to the equilibrium position, and actually harmonic. The numerical results indicate that this model is consistent with normal conduction, and also helps to isolate and identify the local-impurity mechanism for rectification. In this regard it is useful to consider a further simplification, in the spirit of the minimalists models proposed by Pereira [75], so as to distill further the essence of the local rectification mechanism. If the Morse interatomic interaction is substituted by the corresponding harmonic interaction, see the black dotted line in fig. 1b, the rectification effect remains, albeit slightly reduced, see fig. A.5. The chain is then perfectly linear with the only nonlinear exception localized at the impurity. The temperature dependent feature mentioned in [75] as the second necessary condition for rectification besides asymmetry, is here localized in the impurity too, and consists of a different capability to transfer kinetic energy depending on the temperatures on both sides of the impurity. Figure 6 shows temperature profiles for the purely harmonic chain to be compared with the Morse-interaction chain in fig. 4. Flatter profiles are found on both sides of the impurity, as corresponds to the abnormal transport expected for harmonic chains [94]. It would be interesting to combine the impurity effect with other rectification mechanisms (such as grading, long-range interactions, or use of different segments), or with more impurities in series to enhance further the rectification effect.

Even though our motivation was to mimic the effect of a localized atom diode that lets atoms pass only one way, unlike the atom diode [37], all interactions in the present model are elastic. The model may be extended by adding an irreversible, dissipative element so as to induce not only rectification but a truly Maxwell

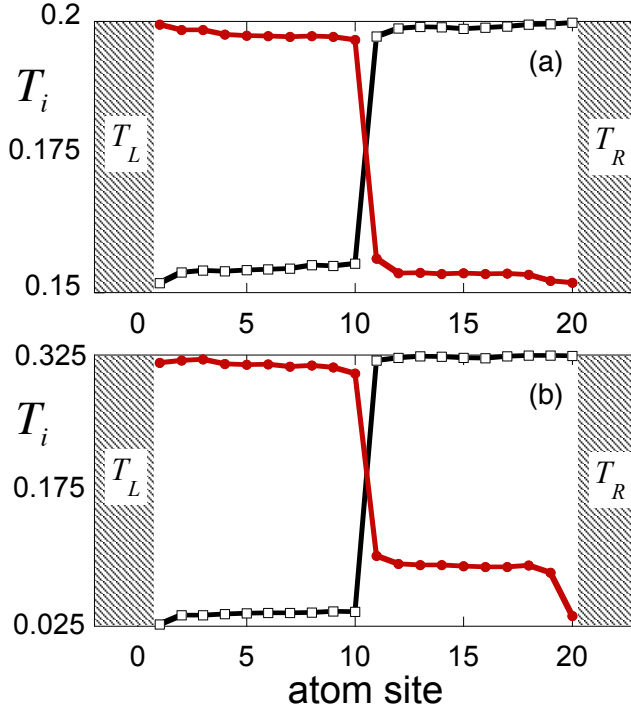


FIGURE A.6: (Color online) Temperature profile for a harmonic interacting chain of $N = 20$ atoms, with an impurity in the $N/2 + 1$ position, with $T_L = T_h$ and $T_R = T_c$ (circles) and with the thermostat baths switched (squares), for (a) $\Delta T = 0.05$ and (b) $\Delta T = 0.3$. The corresponding rectification factors are (a) $R = 18\%$ and (b) $R = 85\%$. Parameters regarding the impurity are the same as in fig. 1.

demon for heat transfer [95, 96]. On the experimental side, one dimensional chains of neutral atoms in optical lattices can be implemented with cold atoms [97]. An impurity with different internal structure could be subjected to a different on-site potential imprinted by a holographic mask [98], and asymmetrical interatomic interactions could be implemented by trapping a controllable polar molecule or mediated by atoms in parallel lattices [99].

We are indebted to G. Casati for raising our attention to thermal rectification and for providing information on his work. We acknowledge financial support by the Basque Government (Grant No. IT986-16) and MINECO/FEDER,UE (Grant No. FIS2015-67161-P). Reid

Appendix B

Chain of Ions

We numerically demonstrate heat rectification for linear chains of ions in trap lattices with graded trapping frequencies, in contact with thermal baths implemented by optical molasses. To calculate the local temperatures and heat currents we find the stationary state by solving a system of algebraic equations. This approach is much faster than the usual method that integrates the dynamical equations of the system and averages over noise realizations.

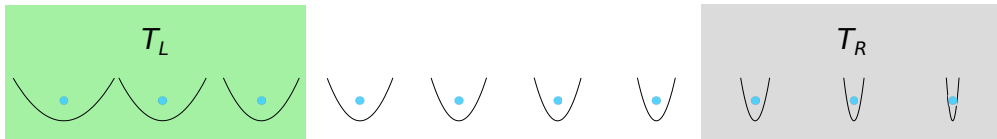


FIGURE B.1: Schematic representation of the frequency-graded chain of trapped ions proposed as a thermal rectifier. The left and right ends of the chain are in contact with optical molasses at temperatures T_L and T_R (green and grey boxes respectively). Each ion is in an individual trap. The (angular) frequencies of the traps increase homogeneously from left to right, starting from ω_1 and ending at $\omega_1 + \Delta\omega$. The ions interact through the Coulomb force, which is long range, and therefore all the ions interact among them, even distant neighbors. By default we use 15 ions.

B.1 Introduction

The ideal thermal rectifier, also “thermal diode”, is a device that allows heat to propagate in one direction, from a hot to a cold bath, but not in the opposite one when the temperature bias of the baths is reversed. The name is set by analogy to the half-wave rectifiers or diodes for electric current. More generally thermal rectification simply denotes asymmetric heat flows (not necessarily all or nothing) when the bath temperatures are reversed. Thermal rectification was discovered by C. Starr in 1936 in a junction between copper and cuprous oxide [100]. Many years later, a work of Terraneo *et al.* demonstrated thermal rectification in a model consisting on a segmented chain of coupled nonlinear oscillators in contact with two thermal baths at temperatures T_H and T_C , with $T_H > T_C$ [71]. This paper sparked a substantial body of research that spans to this day [101] (see Fig. 1 in [72]).

Research on thermal rectification has gained a lot of attention in recent years as a key ingredient to build prospective devices to control heat flows similarly to electrical currents [72, 73]. There are proposals to engineer thermal logic circuits [102] in which information, stored in thermal memories [103], would be processed in thermal gates [104]. Such thermal gates, as their electronic counterparts, will require thermal diodes and thermal transistors to operate [87, 105]. Heat rectifying devices would also be quite useful in nano electronic circuits, letting delicate components dissipate heat while being protected from external heat sources [72].

Most work on thermal diodes has been theoretical with only a few experiments [83, 106–108]. A relevant attempt to build a thermal rectifier was based on a graded structure made of carbon and boron nitride nanotubes that transports heat

between a pair of heating/sensing circuits [83]. One of the ends of the nanotube is loaded with a deposition of another material, which makes the heat flow better from the loaded end to the unloaded end. However, rectifications were small, with rectification factors (relative heat-flow differentials) around 7%.

Much effort has been aimed at improving the rectification factors and the features of the rectifiers. Some works relied, as in [71], on a chain segmented into two or more regions with different properties, but using other lattice models such as the Frenkel-Kontorova (FK) model [78, 109]. The fundamental ingredient for having rectification was attributed to nonlinear forces in the chain [73, 78, 80, 82, 88, 109], which lead to a temperature dependence of the phonon bands or power spectral densities. The bands may match or mismatch at the interfaces depending on the sign of the temperature bias of the baths, allowing or obstructing heat flow [71, 77]. Later, alternative mechanisms have been proposed which do not necessarily rely on anharmonic potentials [75, 110]. Also, Peyrard provided a simple model to explain and build rectifiers based on assuming the Fourier law for heat conduction locally combined with a temperature and position-dependent conductivity [79].

It was soon realized that the performance of segmented rectifiers was very sensitive to the size of the device, i.e., rectification decreases with increasing the length of the rectifier [78]. To overcome this limitation two ideas were proposed. The first one consists in using graded rather than segmented chains, i.e., chains where some physical property varies continuously along the site position such as the mass of particles in the lattice [74, 111–118]. The second one uses particles with long-range interactions (LRI), such that all the particles in the lattice interact with each other [74, 84, 119]. The rationale behind was that in a graded system new asymmetric, rectifying channels are created, while the long-range interactions create also new transport channels, avoiding the usual decay of heat flow with size [74]. Besides a stronger rectification power, LRI graded chains are expected to have better heat conductivity than segmented ones. This is an important point for technological applications, because devices with high rectification factors are not useful if the currents that flow through them are very small.

In this article we propose to bridge the gap between mathematical models and actual systems exploring the implementation of a heat rectifier in a realistic, graded system with long-range interactions: a chain of ultracold ions in a segmented Paul trap with graded microtraps for each ion. Long-range interactions are due to the Coulomb forces, and the baths at the ends of the chain may be implemented with

optical molasses, see Fig. B.1. The trapping frequencies of the microtraps are controlled individually in order to create a graded and asymmetric trap-frequency profile along the chain. This asymmetry will lead to a heat flow that depends on the sign of the temperature difference of the baths. Heat transport in trapped ion chains has been studied in several works [120–124] and interesting phenomena like phase transitions have been investigated [120–123]. The idea of using locally-controlled traps is already mentioned in [120] to implement disorder and study its effects. The device we present here may be challenging to implement, but at reach with the current technology, in particular that of microfabricated traps [125–127]. Thus the setting is thought for a small, realistic number of controllable ions.

The rest of the article is organized as follows. In Section B.2 we describe the physical system of trapped ions with graded trap frequencies. We also set the stochastic dynamics due to the action of lasers at the chain edges. In Section B.3 we implement an efficient method to find the steady state using Novikov’s theorem and solving an algebraic system of equations. In Section B.4 we present simulations of this system exhibiting thermal rectification and discuss the dependence with ion number, different options for the ion-laser coupling, and the advantages/disadvantages of using a graded frequency profile instead of a segmented one. Finally, in Section B.5 we summarize our conclusions, and discuss connections with other works.

B.2 Physical System

Consider a linear lattice of N individual harmonic traps of (angular) trapping frequencies ω_n evenly distributed along the x axis at a distance a from each other. Each trap contains a single ion that interacts with the rest via Coulomb potentials. All the ions are of the same species, with mass m and charge q . The Hamiltonian that describes the dynamics of the system is (we consider only linear, one dimensional motion along the chain axis)

$$H(\mathbf{x}, \mathbf{p}) = \sum_{n=1}^N \left[\frac{p_n^2}{2m} + \frac{m\omega_n^2}{2}(x_n - x_n^{(0)})^2 \right] + V_{int}(\mathbf{x}), \quad (\text{B.1})$$

where $\{x_n, p_n\}$, position and momentum of each ion, are the components of the vectors \mathbf{x}, \mathbf{p} , $x_n^{(0)} = na$ are the centers of the harmonic traps, and V_{int} is the sum

of the Coulomb interaction potential between all pairs of ions,

$$V_{int}(\mathbf{x}) = \frac{1}{2} \sum_n \sum_{l \neq n} V_C(|x_n - x_l|), \quad (\text{B.2})$$

with $V_C(|x_n - x_l|) = \frac{q^2}{4\pi\varepsilon_0} \frac{1}{|x_n - x_l|}$. The ends of the chain are in contact with two thermal reservoirs at temperatures T_L for the left bath and T_R for the right bath respectively. The action of the reservoirs on the dynamics of the chain is modeled via Langevin baths at temperatures T_L and T_R [94, 128]. The equations of motion of the chain, taking into account the baths and the Hamiltonian, are

$$\begin{aligned} \dot{x}_n &= \frac{1}{m} p_n, \\ \dot{p}_n &= -m\omega_n^2(x_n - x_n^{(0)}) - \frac{\partial V_{int}}{\partial x_n} - \frac{\gamma_n}{m} p_n + \xi_n(t), \end{aligned} \quad (\text{B.3})$$

where γ_n and $\xi_n(t)$ are only non-zero for the ions in the end regions, in contact with the left and right baths in the sets $\mathcal{L} = \{1, 2, \dots, N_L\}$ and $\mathcal{R} = \{N - (N_R - 1), \dots, N - 1, N\}$, see Fig. B.1. The γ_n are friction coefficients and $\xi_n(t)$ are uncorrelated Gaussian noise forces satisfying $\langle \xi_n(t) \rangle = 0$ and $\langle \xi_n(t) \xi_m(t') \rangle = 2D_n \delta_{nm} \delta(t - t')$, D_n being the diffusion coefficients. These Gaussian forces are formally the time derivatives of independent Wiener processes (Brownian motions) $\xi_n(t) = \sqrt{2D_n} \frac{dW_n}{dt}$ [121, 129] and Eq. (B.3) is a stochastic differential equation (SDE) in the Stratonovich sense [129].

The baths are physically implemented by optical molasses consisting of a pair of counterpropagating Doppler-cooling lasers [121]. The friction and diffusion coefficients for the ions in contact with the baths are given by [121, 130, 131]

$$\begin{aligned} \gamma_n &= -4\hbar k_{L,R}^2 \left(\frac{I_{L,R}}{I_0} \right) \frac{2\delta_{L,R}/\Gamma}{[1 + (2\delta_{L,R}/\Gamma)^2]^2}, \\ D_n &= \hbar^2 k_{L,R}^2 \left(\frac{I_{L,R}}{I_0} \right) \frac{\Gamma}{1 + (2\delta_{L,R}/\Gamma)^2}, \\ n &\in \mathcal{L}, \mathcal{R}, \end{aligned} \quad (\text{B.4})$$

where k_L (k_R) and I_L (I_R) are the wave vector and intensity of the left (right) laser. δ_L (δ_R) is the detuning of the left (right) laser with respect to the angular frequency ω_0 of the atomic transition the laser is exciting, and Γ is the corresponding natural line width of the excited state. The expressions in Eq. (B.4) are valid only if the intensities of the lasers are small compared to the saturation intensity I_0 ,

$I_{L,R}/I_0 \ll 1$. In this bath model, the friction term in Eq. (B.3) comes from the cooling action of the laser and the white noise force $\xi_n(t)$ corresponds to the random recoil of the ions due to spontaneous emission of photons [130, 131]. Using the diffusion-dissipation relation $D = \gamma k_B T$ [132], the temperatures of the optical molasses baths are given by

$$T_{L,R} = -\frac{\hbar\Gamma}{4k_B} \frac{1 + (2\delta_{L,R}/\Gamma)^2}{(2\delta_{L,R}/\Gamma)}, \quad (\text{B.5})$$

with k_B being the Boltzmann constant. If the laser intensities are low enough, the temperatures of the baths are controlled by modifying the detunings. When $\delta = \delta_D = -\Gamma/2$ the optical molasses reach their minimum temperature possible, the Doppler limit $T_D = \hbar\Gamma/(2k_B)$. Note that away from the Doppler limit the same temperature may be achieved for two different values of detuning. These two possibilities imply different couplings (two different pairs of γ and D values) and thus different physical effects that will be studied in Sec. B.4.3.

B.3 Calculation of the stationary heat currents

The local energy of each site is defined by

$$H_n = \frac{1}{2m} p_n^2 + \frac{1}{2} m\omega_n^2 (x_n - x_n^{(0)})^2 + \frac{1}{2} \sum_{l \neq n} V_C(|x_n - x_l|). \quad (\text{B.6})$$

Differentiating H_n with respect to time we find the continuity equation

$$\dot{H}_n = \frac{p_n}{m} \left[\xi_n(t) - \gamma_n \frac{p_n}{m} \right] - \frac{1}{2m} \sum_{l \neq n} \frac{\partial V_C(|x_n - x_l|)}{\partial x_n} (p_n + p_l). \quad (\text{B.7})$$

Two different contributions can be distinguished: $j_n^B \equiv \frac{p_n}{m} [\xi_n(t) - \gamma_n \frac{p_n}{m}]$, which is the energy flow from the laser reservoir to the ions at the edges of the chain (only for $n \in \mathcal{L}, \mathcal{R}$), and $\dot{H}_n^{int} \equiv -\frac{1}{2m} \sum_{l \neq n} \frac{\partial V_C(|x_n - x_l|)}{\partial x_n} (p_n + p_l)$, which gives the “internal” energy flow due to the interactions with the rest of the ions. In the steady state $\langle \dot{H}_n \rangle = 0$, and therefore

$$\langle j_n^B \rangle + \langle \dot{H}_n^{int} \rangle = 0, \quad (\text{B.8})$$

where $\langle \dots \rangle$ stands for the expectation value with respect to the ensemble of noise processes $\xi(t)$ (ξ represents a vector with components ξ_n). Equation (B.8) implies that, in the steady state, the internal rates \dot{H}_n^{int} vanish for the inner ions of the chain because $j_n^B = 0$ for $n \notin \mathcal{L}, \mathcal{R}$. In chains with nearest-neighbor (NN) interactions, $\langle \dot{H}_n^{int} \rangle$ simplifies to two compensating and equal-in-magnitude contributions that define the homogeneous heat flux across the chain. For long-range interactions this is not so and defining the flux is not so straightforward. A formal possibility is to impose nearest-neighbor interatomic interactions for some atoms in the chain [74], but this approach is not realistic in the current system so we define instead the heat currents for the left and right baths as

$$\begin{aligned} J_L(t) &= \sum_{n \in \mathcal{L}} \langle j_n^B \rangle, \\ J_R(t) &= \sum_{n \in \mathcal{R}} \langle j_n^B \rangle, \end{aligned} \quad (\text{B.9})$$

respectively. These expressions are in general time-dependent. In the steady state we must have $J_{L,\text{steady}} + J_{R,\text{steady}} = 0$, since the local energies stabilize and internal energy flows cancel. We use either $J_{L,\text{steady}}$ or $J_{R,\text{steady}}$ to calculate the total energy flow in the chain, always taking the absolute value, i.e., $J \equiv |J_{L,\text{steady}}| = |J_{R,\text{steady}}|$. J is defined as J_\rightarrow when the hot bath is on the left and J_\leftarrow when it is on the right.

To compute the average heat fluxes of the baths $\langle j_n^B \rangle$ in Eq. (B.9) we need the averages $\langle p_n(t)\xi_n(t) \rangle$. Instead of explicitly averaging $p_n(t)\xi_n(t)$ over different realizations of the white noise we use Novikov's theorem [129, 133, 134]. Novikov's theorem states that the ensemble average (over the realizations of the noise) of the product of some functional $\phi(t)$, which depends on a Gaussian noise $\xi(t)$ with zero mean value, $\langle \xi(t) \rangle = 0$, and the noise itself, is given by

$$\langle \xi(t)\phi(t) \rangle = \int_0^t dt' \langle \xi(t)\xi(t') \rangle \left\langle \frac{\delta\phi(t)}{\delta\xi(t')} \right\rangle, \quad (\text{B.10})$$

where $\delta\phi(t)/\delta\xi(t')$ is the functional derivative of $\phi(t)$ with respect to the noise, with $t' < t$. When the noise is δ -correlated, $\langle \xi(t)\xi(t') \rangle = 2D\delta(t-t')$, and Eq. (B.10) reads $\langle \xi(t)\phi(t) \rangle = D \langle \delta\phi(t)/\delta\xi(t') \rangle |_{t' \rightarrow t^-}$. To apply Novikov's theorem to our model we need the functional derivatives of the position $x_n(t)$ and momentum $p_n(t)$ coordinates with respect to the white noises. We integrate Eq. (B.3) to have

its formal solution as a functional depending on the white Gaussian noises $\xi_n(t)$,

$$\begin{aligned} x_n(t) &= x_n(0) + \frac{1}{m} \int_0^t ds p_n(s), \\ p_n(t) &= p_n(0) + \int_0^t ds \left[-\frac{\partial H}{\partial x_n}(s) - \frac{\gamma_n}{m} p_n(s) + \xi_n(s) \right]. \end{aligned} \quad (\text{B.11})$$

Equation (B.11) implies that the functional derivatives are $\delta x_n(t)/\delta \xi_m(t')|_{t' \rightarrow t^-} = 0$ and $\delta p_n(t)/\delta \xi_m(t')|_{t' \rightarrow t^-} = \delta_{nm}$ (δ_{nm} is the usual Kronecker delta symbol). Thus we have $\langle x_n(t)\xi_m(t) \rangle = 0$ and $\langle p_n(t)\xi_m(t) \rangle = \delta_{nm}D_m$, which gives for the heat flow from the baths

$$\langle j_n^B \rangle = \frac{1}{m} \left[D_n - \gamma_n \frac{\langle p_n^2 \rangle}{m} \right]. \quad (\text{B.12})$$

In all simulations we check that $|J_{L,\text{steady}}| = |J_{R,\text{steady}}|$ within the numerical tolerance of the computer. To measure the asymmetry of the heat currents we use the rectification factor R defined as

$$R = \frac{J_\rightarrow - J_\leftarrow}{\max(J_\rightarrow, J_\leftarrow)}. \quad (\text{B.13})$$

R values may go from -1 to 1 (In the figures we depict it in % between -100% and 100%). If there is no rectification $J_\rightarrow = J_\leftarrow$ and $R = 0$. For perfect rectification in the right (left) direction, $J_\rightarrow \gg J_\leftarrow$ ($J_\rightarrow \ll J_\leftarrow$), and $R = 1$ ($R = -1$). Take note that other definitions of rectification factors exist in many works on asymmetric heat transfer so comparisons should be done with care.

This model does not show the antithermodynamical behavior observed in other models [135, 136], and heat is found to flow in all cases from the hot to the cold bath.

B.3.1 Algebraic, small-oscillations approach to calculate the steady state

To find the temperature profiles and heat currents in the steady state the usual approach is to solve the SDE system in Eq. (B.3) up to long times and for many realizations of the white noises $\xi(t)$. In that way the ensemble averages $\langle p_n(t \rightarrow \infty)^2 \rangle$, necessary for both the temperature profiles and heat currents, are computed. This standard route implies a heavy computational effort, in particular when we want to study the heat transport for several bath configurations,

frequency increments and chain parameters. It is possible to circumvent this difficulty and find ensemble averages like $\langle x_n x_m \rangle$, $\langle x_n p_m \rangle$, $\langle p_n p_m \rangle$ (second order moments) without integrating any SDE [137]. The idea is to impose the condition $d\langle \dots \rangle / dt = 0$ for all the second order moments and linearize the dynamical equations of the system around equilibrium. A system of linear algebraic equations for the moments results, that can be easily solved without solving the SDE many times.

To linearize the SDE in Eq. (B.3) we approximate the potential energy of the Hamiltonian in Eq. (B.1), $V(\mathbf{x}) = V_{int}(\mathbf{x}) + m \sum_n \omega_n^2 (x_n - x_n^{(0)})^2 / 2$, by its harmonic approximation around the equilibrium positions \mathbf{x}^{eq} , defined by $\frac{\partial V(\mathbf{x})}{\partial \mathbf{x}} \Big|_{\mathbf{x}=\mathbf{x}^{eq}} = 0$. The approximate potential (ignoring the zero-point energy) is

$$V(\mathbf{x}) \approx \frac{1}{2} \sum_{n,m} K_{nm} (x_n - x_n^{eq})(x_m - x_m^{eq}), \quad (\text{B.14})$$

with $K_{nm} = \frac{\partial^2 V(\mathbf{x})}{\partial x_n \partial x_m} \Big|_{\mathbf{x}=\mathbf{x}^{eq}}$ being the Hessian matrix entries of $V(\mathbf{x})$ around the equilibrium configuration [138]

$$K_{nm} = \begin{cases} m\omega_n^2 + 2 \left(\frac{q^2}{4\pi\varepsilon_0} \right) \sum_{l \neq n} \frac{1}{|x_n^{eq} - x_l^{eq}|^3} & \text{if } n = m \\ -2 \left(\frac{q^2}{4\pi\varepsilon_0} \right) \frac{1}{|x_n^{eq} - x_m^{eq}|^3} & \text{if } n \neq m \end{cases}. \quad (\text{B.15})$$

Note that this approximation does not modify the two main features of the system, namely asymmetry and long-range interactions, which are manifest in the asymmetric distribution of ω_n and the non-zero off-diagonal elements of the K matrix, respectively. In the following we will use $y_n = x_n - x_n^{eq}$ to simplify the notation. The linearized dynamics around the equilibrium positions are given by

$$\begin{aligned} \dot{y}_n &= \frac{1}{m} p_n, \\ \dot{p}_n &= - \sum_l K_{nl} y_l - \frac{\gamma_n}{m} p_n + \xi_n(t). \end{aligned} \quad (\text{B.16})$$

Now, we set $d\langle \dots \rangle / dt = 0$ for all the moments. Using Eq. (B.16) and applying Novikov's theorem we find

$$\begin{aligned} \langle p_n p_l \rangle - \gamma_l \langle y_n p_l \rangle - \sum_m K_{lm} \langle y_n y_m \rangle &= 0, \\ \sum_m [K_{nm} \langle y_m p_l \rangle + K_{lm} \langle y_m p_n \rangle] + \frac{1}{m} (\gamma_l + \gamma_n) \langle p_n p_l \rangle &= 2\delta_{nl} D_n. \end{aligned} \quad (\text{B.17})$$

The system (B.17) is linear in the second order moments so it can be solved numerically to find the steady-state values of the moments. Besides Eq. (B.17) we have that $\langle y_n p_l \rangle = -\langle y_l p_n \rangle$, which follows from Eq. (B.16) and $d \langle y_n y_m \rangle / dt = 0$. Since there are $\frac{1}{2}N(N - 1)$ independent $\langle y_n p_l \rangle$ moments, we choose the ones with $n < l$. Similarly, the moments $\langle y_n y_l \rangle$ and $\langle p_n p_l \rangle$ contribute with $\frac{1}{2}N(N + 1)$ independent variables each and we choose the ones with $n \leq m$. Thus there are in total $\frac{1}{2}N(3N + 1)$ independent moments that we arrange in the vector

$$\boldsymbol{\eta} = \left[\langle y_1 y_1 \rangle, \langle y_1 y_2 \rangle, \dots, \langle y_N y_N \rangle, \langle p_1 p_1 \rangle, \langle p_1 p_2 \rangle, \dots, \langle p_N p_N \rangle, \langle y_1 p_2 \rangle, \langle y_1 p_3 \rangle, \dots, \langle y_{N-1} p_N \rangle \right]^T. \quad (\text{B.18})$$

There are the same number of independent equations as independent moments: N^2 equations correspond to the first line in Eq. (B.17), and $\frac{1}{2}N(N + 1)$ equations to the second line because of the symmetry with respect to n, l . The system of equations (B.17) may be compactly written as $\mathbf{A}\boldsymbol{\eta} = \mathbf{B}$, where \mathbf{A} and \mathbf{B} are a $\frac{1}{2}N(3N + 1)$ square matrix and vector.

B.4 Numerical Results

We now display the results of our simulations. To find the temperature profiles and the currents in the steady state we use the algebraic method described in section B.3.1. We also check that the results coincide with those by solving Eq. (B.3) for many different realizations of the noisy forces $\boldsymbol{\xi}(t)$ and averaging. The code for all the numerical simulations has been written in the language *Julia* [139, 140]. In particular, to solve the Langevin equation, we used *Julia*'s package *DifferentialEquations.jl* [141].

To model the baths and the chain we use atomic data taken from ion trap experiments [142, 143]. We consider 15 $^{24}\text{Mg}^+$ ions in all figures except in Fig. B.6. The three leftmost and three rightmost ions are illuminated by Doppler cooling lasers. The Doppler cooling lasers excite the transition $3s^2 S_{1/2} \rightarrow 3p^2 P_{1/2}$, with angular frequency $\omega_0 = 2\pi \times 1069$ THz and excited state line width $\Gamma = 2\pi \times 41.3$ MHz [121]. For this ionic species and atomic transition the Doppler limit is $T_D = 1$ mK. The intensities of the laser beams are small compared to the

saturation intensity I_0 so that Eq. (B.4) holds. We take $I_n/I_0 = 0.08$ for the ions in the laser beams, whereas $I_n = 0$ for the rest.

The temperatures T_L , T_R of the left and right laser baths are controlled with their detunings δ_L , δ_R with respect to the atomic transition. We fix two values for the detunings, δ_H and δ_C , such that $T_H > T_C$ (hot and cold baths, also source and drain) and we define J_{\rightarrow} (J_{\leftarrow}) as the stationary heat current in the chain when $T_L = T_H$ and $T_R = T_C$ ($T_L = T_C$ and $T_R = T_H$).

Except in Sec. B.4.5 we consider a graded frequency profile. If the frequency of the leftmost trap is ω_1 , the frequency of the n th trap will be $\omega_n = \omega_1 + \Delta\omega \frac{n-1}{N-1}$ up to $\omega_1 + \Delta\omega$ for the rightmost trap. In Sec. B.4.5 we compare the graded chain to a segmented chain, where the left half of the chain has trapping frequencies ω_1 while the other half has $\omega_1 + \Delta\omega$.

B.4.1 Evolution to steady state

To compare the results by solving Eq. (B.3) and averaging and those from the algebraic method we simulated a frequency graded chain with a trapping frequency $\omega_1 = 2\pi \times 50$ kHz for the leftmost ion, see Fig. B.2. The number of ions interacting with the laser beams (three on each bath) is consistent with the lattice constant and typical waists of Gaussian laser beams [142, 143]. To set the trap distance we fix first the characteristic length $l = \left(\frac{q^2}{4\pi\epsilon_0 m\omega_1^2}\right)^{1/3}$ as the distance for which the Coulomb repulsion of two ions equals the trap potential energy for an ion at a distance l away from the center of its trap. If $a < l$, the Coulomb repulsion of the ions is stronger than the trap confinement which makes the ions jump from their traps. With the parameters used in this section we have $l = 38.7$ μm and set $a = 1.29 l = 50$ μm . The detunings of the *hot* and *cold* lasers are $\delta_H = -0.02\Gamma$, and $\delta_C = -0.1\Gamma$ which gives temperatures $T_H \approx 12$ mK and $T_C \approx 3$ mK. We fix the value $\Delta\omega = 0.5\omega_1$ for the frequency increment.

The results of the two methods are in very good agreement. In the scale of Fig. B.2 (a) the calculated local temperatures are undistinguishable. In the calculation based on solving the dynamics we had to integrate Eq. (B.3) for $N_{\text{trials}} = 1000$ realizations of white noise $\xi(t)$. The method based on the system of moments shortened the calculation time with respect to the dynamical trajectories by a factor of 1/700. In fact, the time gain is even more important because the dynamical

method requires further processing, performing a time averaging to compute the stationary flux in addition to noise averaging, see Fig. B.2 (b).

Additionally, the relaxation to the steady state slows down when the frequencies of the traps increase since the deterministic part of the Langevin equation dominates the dynamics over the stochastic part, entering an under-damped regime. In contrast, this increase does not affect the algebraic method.

B.4.2 Rectification in frequency graded chains

In this subsection we demonstrate rectification for the frequency graded chain. We used the method described in section B.3.1 for $^{24}\text{Mg}^+$ ions with the same parameters for the baths used before. We fix the trapping frequency of the leftmost trap to $\omega_1 = 2\pi \times 1 \text{ MHz}$, and a trap spacing $a = 4.76 l$ ($25 \mu\text{m}$) (the characteristic length is $l = 5.25 \mu\text{m}$). Figure B.3 depicts the results with these parameters in a graded chain. Figure B.3 (a) shows that both J_{\rightarrow} and J_{\leftarrow} decrease rapidly as the frequency increment is increased. The rectification reaches its maximum value for a frequency difference of $\Delta\omega \approx 0.1\omega_1$. The fluxes cross so there are some points where the rectification is exactly zero, besides the trivial one at $\Delta\omega = 0$, at $\Delta\omega = 0.05\omega_1, 0.3\omega_1, 1.3\omega_1$. At these points the direction of rectification reverses, presumably as a consequence of the changes in the match/mismatch of the temperature dependent local power spectra. The change of rectification direction occurs for all the choices of parameters, as displayed in Fig. B.4. Figure B.4 gives the rectification factor for different trap distances and frequency increments. 0-rectification curves separate regions with different rectification direction. The second region in Fig. B.4 (starting from the left) would be the most interesting one to build a thermal diode, since rectification reaches its largest values there.

For small values of $\Delta\omega$ there is little asymmetry in the chain and therefore modest rectification is expected whereas a very large $\Delta\omega$ implies very high trapping frequencies on the right implying too strong a confinement and vanishing interactions. This bottleneck decreases the fluxes in both directions and the rectification. However, since $\Delta\omega$ is controllable, and the range of values of $\Delta\omega$ for which rectification is larger can be also controlled with the intertrap distance a , see Fig. B.4, the existence of a rectification window does not imply a major limitation.

B.4.3 Same bath temperatures, different bath couplings

As already mentioned below Eq. (B.5), above and below the detuning $\delta_D = -\Gamma/2$ corresponding to the Doppler limit temperature, the optical molasses allow for two different couplings (two pairs of friction and diffusion coefficients in Eq. (B.4)) between the ions and the laser corresponding to the same bath temperature. This duality may be seen explicitly in Fig. B.5. Specifically Fig. B.5 (a) depicts the variation of the friction coefficient for values of δ around δ_R , and Fig. B.5 (b) the corresponding temperatures. Interestingly, the different couplings imply different rectification factors. If we set $\delta_C = \delta_D = -\Gamma/2$, i.e., the cold bath is cooled to the Doppler limit, δ_H can be chosen to be below or above δ_D for the same temperature T_H . The corresponding rectification factors for the two choices are shown in Fig. B.5 (c), which demonstrates that significant rectification can be achieved by choosing $\delta_H < \delta_D$ for temperature increments that are smaller than or of the order of $T_C = T_D$, for example $R \approx 20\%$ for $\Delta T = 0.1T_C$, or $R \approx 60\%$ for $\Delta T = T_C$. Finding good rectification at low (relative) temperature differences is considered to be one on the challenges in asymmetric heat transport research [144].

B.4.4 Dependence with ion number

Keeping in mind that scaling the frequency-graded ion chain to a large numbers of ions is not a realistic option in this setting, it is nevertheless important to study the dependence with ion number from small to moderate numbers. In Fig. B.6 we observe an overall trend in which the rectification decreases with the number of ions in the chain (while it increases with temperature bias ΔT in the studied range). This effect is easy to understand, as increasing N while keeping the total variation of the trapping frequency $\Delta\omega$ constant, the frequency gradient decreases. This lowers the asymmetry in the chain and the rectification factor. Oscillations with N superimposed to the global trend are more visible at the smaller N values giving an optimal N value at $N = 19$.

B.4.5 Graded versus segmented

We have also compared the performance of the graded thermal diode and a segmented version in which the left half of the chain is trapped with frequency ω_1 and the right half (including the middle ion) with $\omega_1 + \Delta\omega$. Even though the optimal rectification in Fig. B.7 (a) for the segmented chain is larger than for the graded chain, the fact that the fluxes are generally much larger for the graded chain, see Fig. B.7 (b), makes the graded chain more interesting for applications.

B.5 Summary and discussion

In this article we have numerically demonstrated heat rectification in a chain of ions trapped in individual microtraps with graded frequencies, connected at both ends to thermal baths created by optical molasses. An alternative to implement a graded frequency profile in the lab could be combining a collective Paul trap for all the ions with on-site dipolar laser forces [120, 145–147].

A goal of this article is to connect two communities, ion trappers and researchers on heat-rectification models. The results found are encouraging and demonstrate the potential of a trapped-ion platform to experimentally investigate heat rectification schemes. Trapped ions are quite interesting to this end because they are highly controllable, and may easily adopt several features to enhance rectification, such as the ones explored here (long-range interactions and an asymmetrical gradation), or others such as time dependent forces [73, 148], or different nonlinearities in onsite forces. The limitations and application domain should also be clear, the proposed platform is circumscribed to cold temperatures of the order of hundreds of μK to mK achieved by Doppler cooling. In this sense it is not aimed at competing with (it is rather complementary to) proposals for which experiments [83, 106–108] or simulations [144, 149, 150] demonstrate thermal rectification at room temperature or for hundreds of K . Also, the number of ions should realistically be kept small so the proposed ion chain is not aimed at achieving a macroscopic diode length, but at playing a role in thermal diode research and in the context of ion-trapped based quantum technologies.

Methodologically, the calculation of the steady state has been performed with an algebraic approach much faster than the time-consuming integration and averaging over noise and time of the dynamical equations. The algebraic approach linearizes the forces around equilibrium positions which, in this system and for the realistic parameters considered is well justified and tested numerically. The results found provide additional evidence that simple linear models may rectify heat flow [75]. We underline that our linear model is, arguably, even simpler than some linear “minimalist, toy models” in [75] that showed rectification (our on-site forces are already linear from the start and the temperature dependence of explicit model parameters is only in the coefficients of the Langevin baths), with the important bonus of being also realistic.

To shed some more light on the mechanism behind the observed rectification we may analyze the local thermal conductivities $\lambda[x, T(x)]$ defined in a continuous model by [79]

$$J = \lambda[x, T(x)] \left| \frac{dT(x)}{dx} \right|, \quad (\text{B.19})$$

where J is the stationary heat current and $T(x)$ the local temperature. (We use the modulus of the temperature derivative for consistency with our (positive) definition of J .) In our model we discretize the coordinate with the ion index and the temperature derivative is discretized as

$$\frac{dT_n}{dx} = \frac{T_{n+1} - T_{n-1}}{x_{n+1}^{eq} - x_{n-1}^{eq}}. \quad (\text{B.20})$$

Through integration, it is clear that when λ depends on both temperature and position rectification is possible. In the continuous model the temperature increment between the baths is

$$|T_L - T_R| = \int_0^L \frac{J}{\lambda[x, T(x)]} dx \quad (\text{B.21})$$

so that the key for rectification is a different integral of the inverse of the conductivities in the two scenarios ($T_L = T_H, T_R = T_C$ with conductivity $\lambda_{\rightarrow}[x, T_{\rightarrow}(x)]$ along a local temperature decreasing from the left or the reversed one, $T_R = T_H, T_L = T_C$ with conductivity $\lambda_{\leftarrow}[x, T_{\leftarrow}(x)]$ along an increasing local temperature). Particularly favorable for rectification is the scenario where one of the lambdas is above the other one for all x . Figure B.8 shows that this is essentially the case in our model, at least along the most relevant part of the integral.

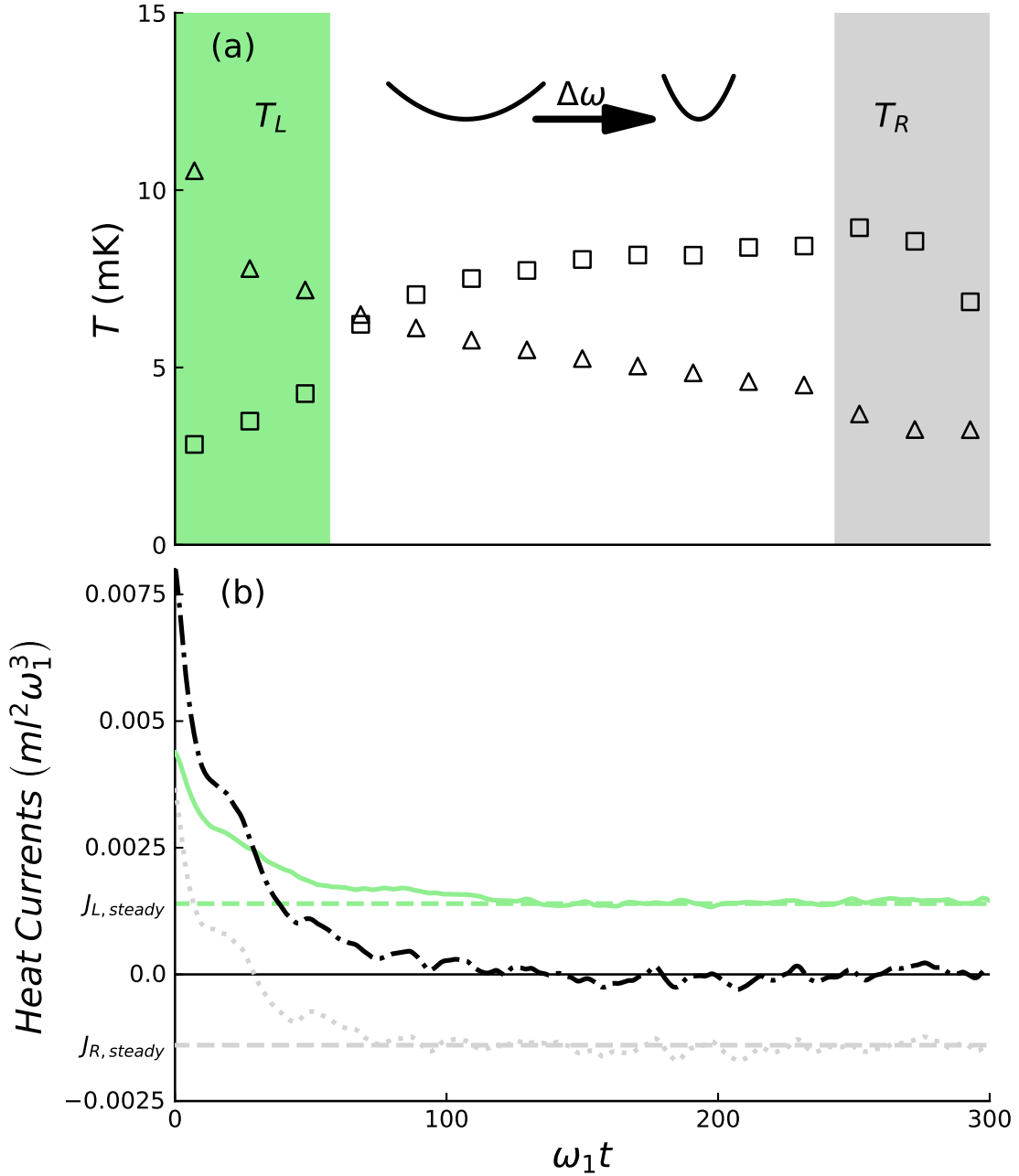


FIGURE B.2: (a) Temperatures of the ions in the stationary state for a graded chain with the parameters described in section B.4.1. The temperature profiles found with the algebraic method (Eq. (B.17)) are indistinguishable from the ones found solving the Langevin equation (Eq. (B.3)). Empty triangles (squares) correspond to $T_L = T_H$ ($T_L = T_C$) and $T_R = T_C$ ($T_R = T_H$). (b) Heat currents as a function of time for $T_L = T_H$ and $T_R = T_C$, see Eq. (B.9): $J_L(t)$ (solid green line) from the left reservoir into the chain; $J_R(t)$ (dotted grey line) from the right reservoir into the chain (negative except at very short times); $J_L(t) + J_R(t)$ (dotted-dashed black line), which must go to zero in the steady state. The three lines tend to stationary values marked by horizontal lines. Parameters: $\omega_1 = 2\pi \times 50$ kHz, $a = 50$ μm , $\delta_H = -0.02\Gamma$, and $\delta_C = -0.1\Gamma$, which gives temperatures $T_H \approx 12$ mK and $T_C \approx 3$ mK. $\Delta\omega = 0.5\omega_1$. In all figures $\Gamma = 2\pi \times 41.3$ MHz.

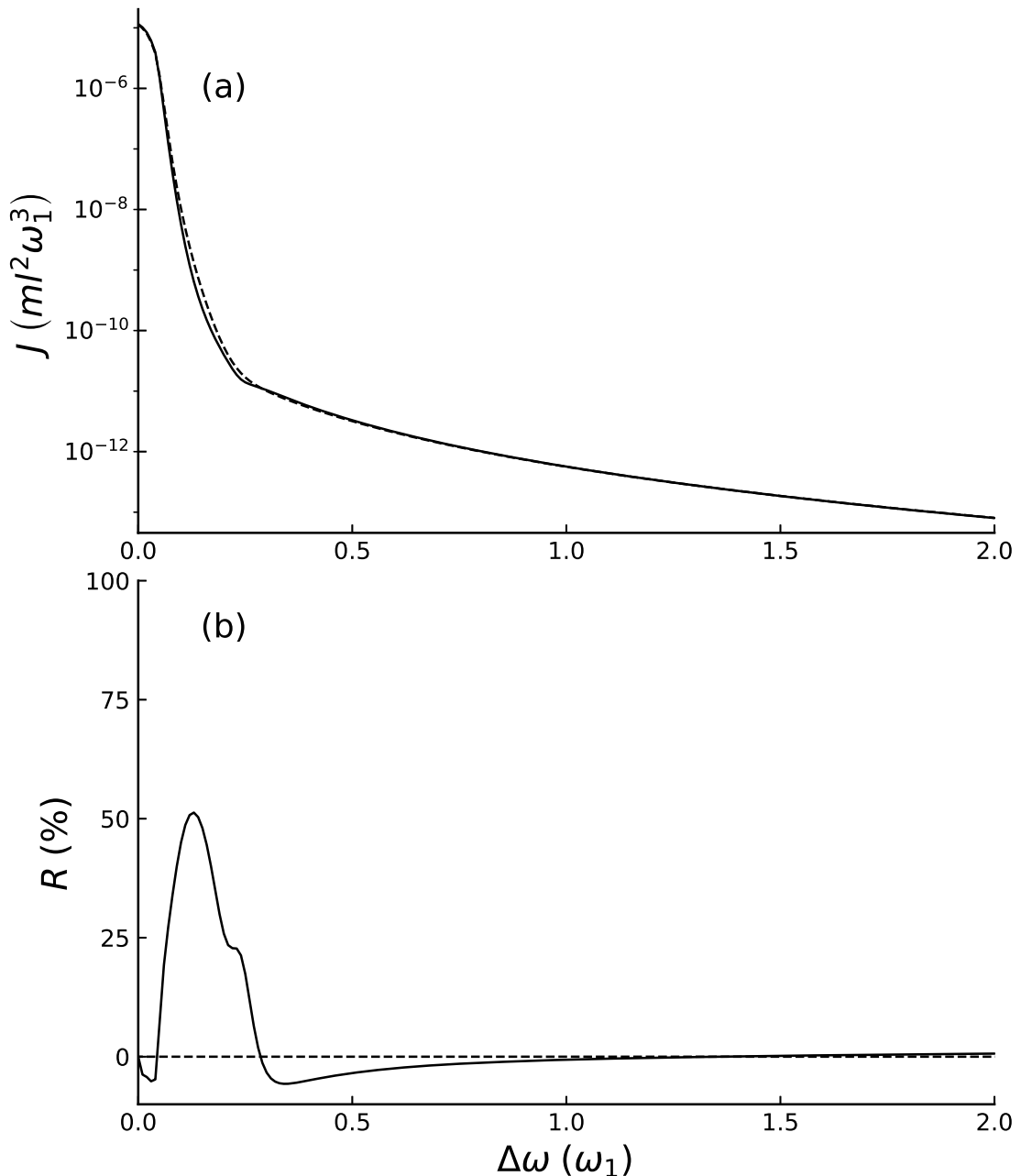


FIGURE B.3: Graded chain of $N = 15$ $^{24}\text{Mg}^+$ ions. (a) Stationary fluxes for different frequency increments: J_{\rightarrow} (for $T_L = T_H$ and $T_R = T_C$, dashed line); J_{\leftarrow} (for $T_L = T_C$ and $T_R = T_H$, solid line) (b) Rectification factor. Parameters: $\omega_1 = 2\pi \times 1$ MHz, $l = 5.25$ μm , $a = 4.76 l$ (25 μm), $\delta_H = -0.02 \Gamma$, and $\delta_C = -0.1 \Gamma$.

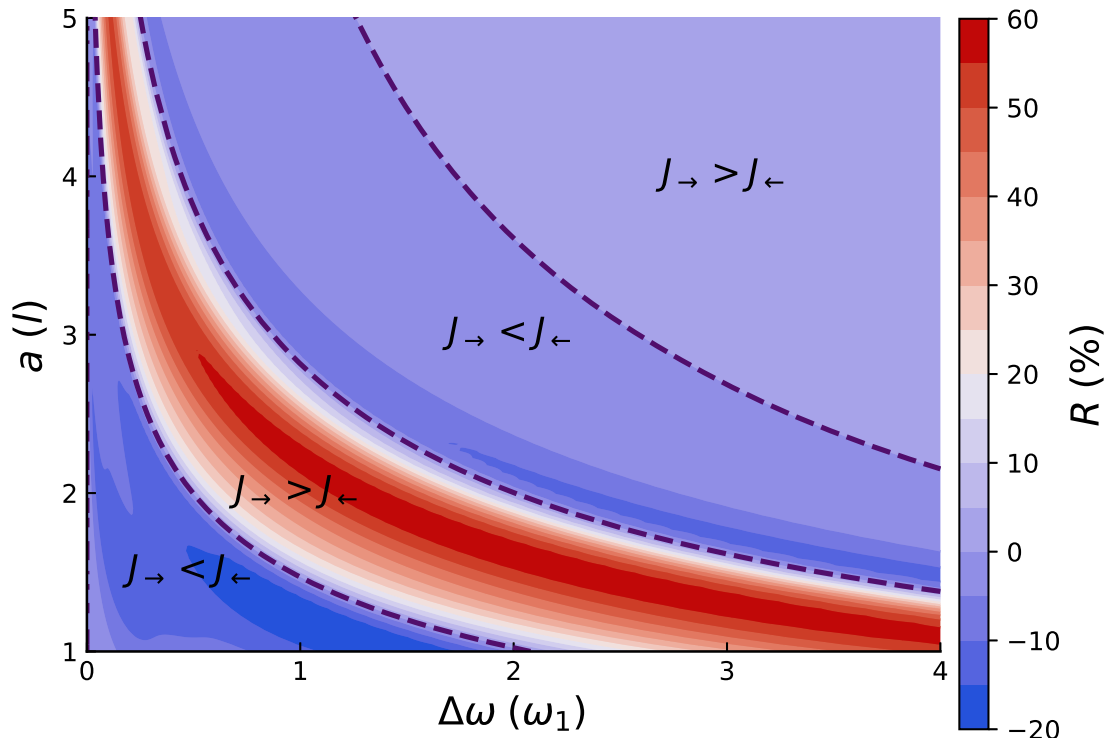


FIGURE B.4: Rectification factor in a graded chain of $N = 15$ $^{24}\text{Mg}^+$ ions for different trap distances and frequency increment. The dashed lines are for $R = 0$ and delimit the regions $J_{\rightarrow} > J_{\leftarrow}$ and $J_{\rightarrow} < J_{\leftarrow}$. The parameters are $\omega_1 = 2\pi \times 1$ MHz, $l = 5.25$ μm , $\delta_H = -0.02\Gamma$, and $\delta_C = -0.1\Gamma$.

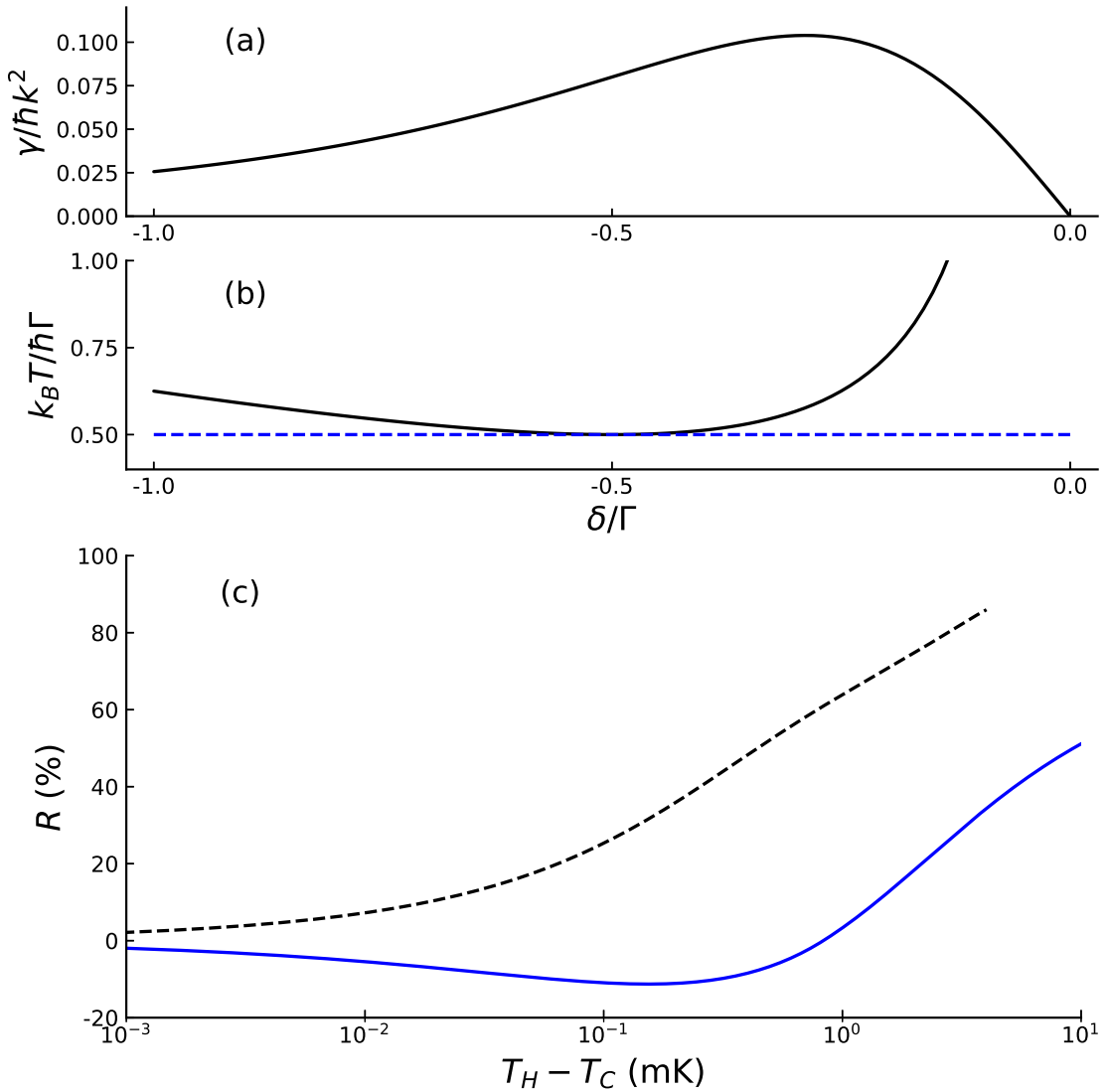


FIGURE B.5: (a) Friction coefficient defined in Eq. (B.4). (b) Bath temperature defined in Eq. (B.5). (c) Rectification as a function of the temperature difference between the hot and cold baths $T_H - T_C$ for δ_H below (dashed black line) and above (solid blue line) the Doppler limit, and $\delta_C = \delta_D$ (Doppler limit).

Parameters: $\omega_1 = 2\pi \times 1$ MHz, $\Delta\omega = 0.15 \omega_1$, $l = 5.25 \mu\text{m}$, $a = 4.76 l$.

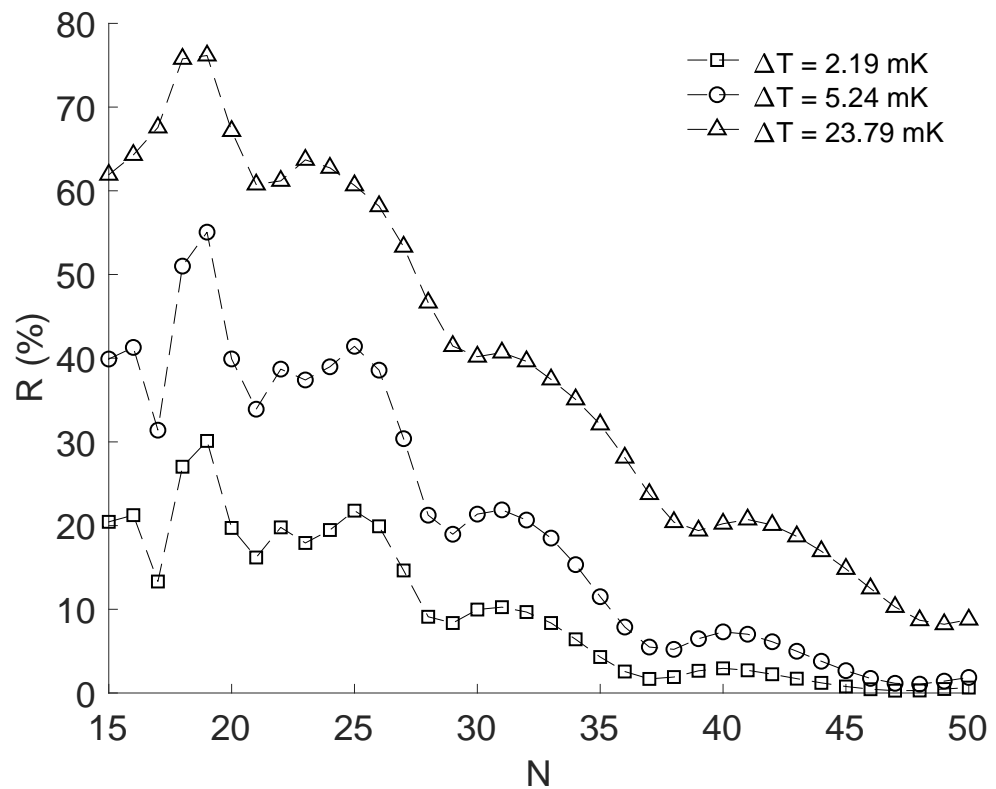


FIGURE B.6: Rectification factor for different bath temperature differences ΔT as the number of ions is increased. The detuning of the cold bath laser is set to the Doppler limit $\delta_C = -\Gamma/2$. $\omega_1 = 2\pi \times 1 \text{ MHz}$, $\Delta\omega = 0.15 \omega_1$, $l = 5.25 \mu\text{m}$, $a = 4.76 l$.

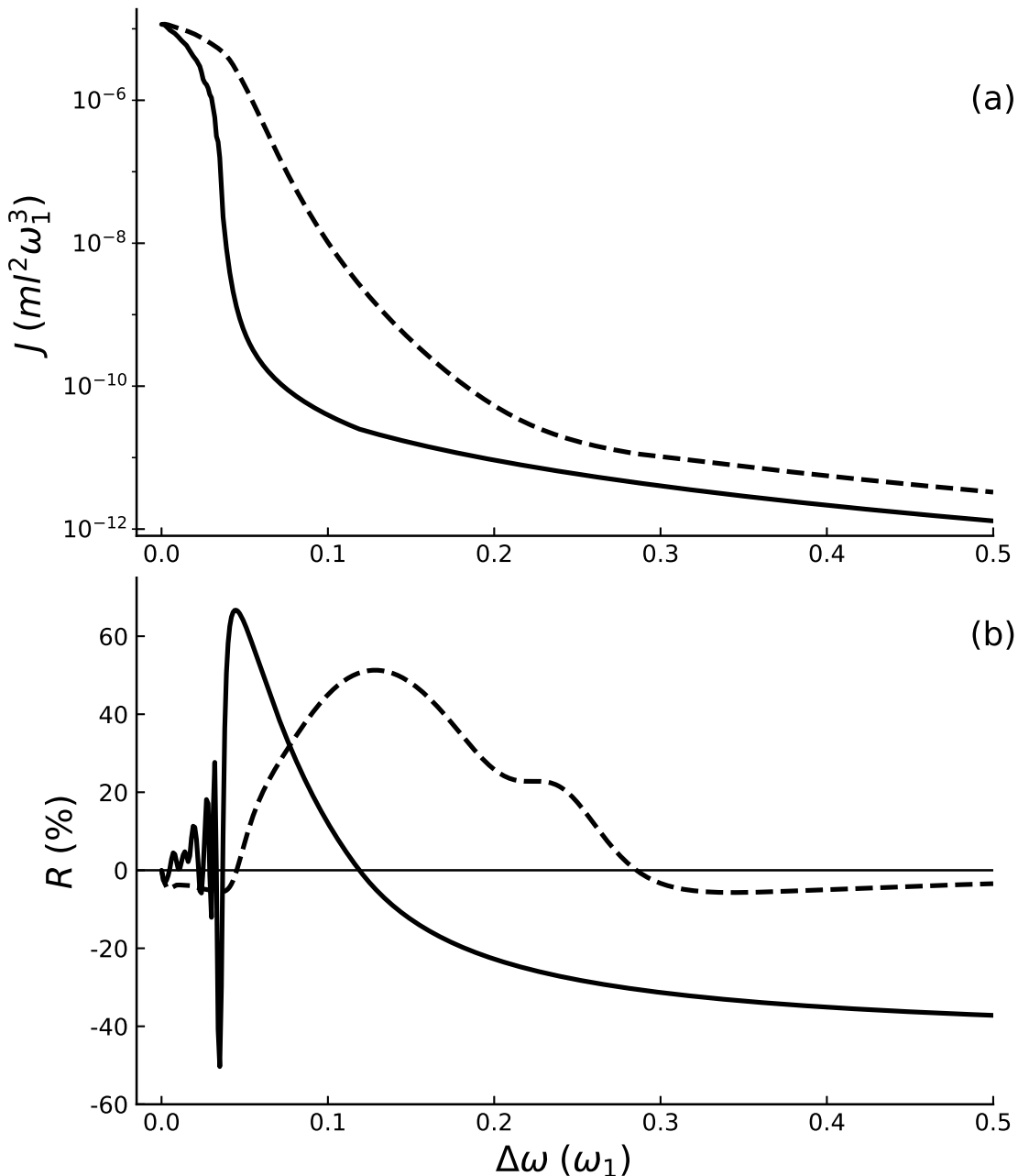


FIGURE B.7: Comparison of graded and segmented chains with $N = 15$ $^{24}\text{Mg}^+$ ions. (a) Maximum of J_{\rightarrow} and J_{\leftarrow} for the graded and segmented chain for different frequency increments. (b) Rectification factor: graded chain (dashed lines); segmented chain (solid lines). Parameters: $\omega_1 = 2\pi \times 1$ MHz, $l = 5.25$ μm , $a = 4.76 l$, $\delta_H = -0.02 \Gamma$, and $\delta_C = -0.1 \Gamma$.

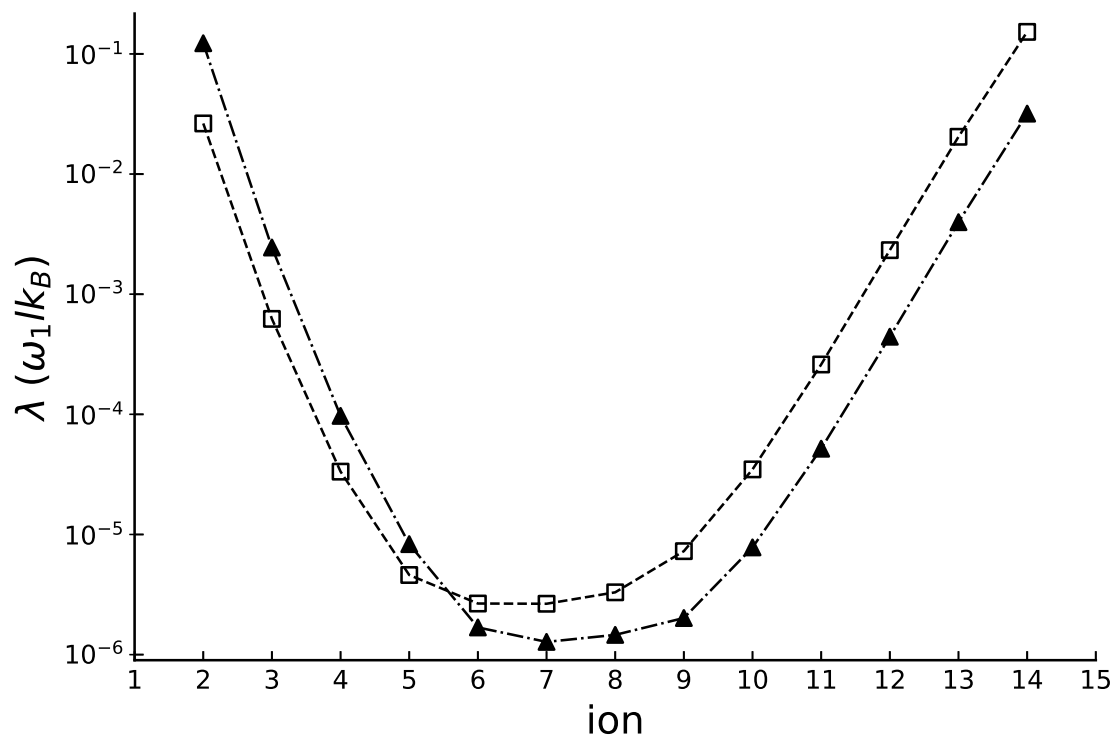


FIGURE B.8: Thermal conductivity through the chain for $T_L > T_R$ (empty squares), and $T_L < T_R$ (filled triangles). $\omega_1 = 2\pi \times 1$ MHz, $\Delta\omega = 0.15\omega_1$, $l = 5.25 \mu\text{m}$, $a = 4.76 l$, $\delta_H = -0.02\Gamma$ and $\delta_C = -0.1\Gamma$.

Appendix C

Rectification in a toy model

We study heat rectification in a minimalistic model composed of two masses subjected to on-site and coupling linear forces in contact with effective Langevin baths induced by laser interactions. Analytic expressions of the heat currents in the steady state are spelled out. Asymmetric heat transport is found in this linear system if both the bath temperatures and the temperature dependent bath-system couplings are also exchanged.

C.1 Introduction

Heat rectification, firstly observed in 1936 by Starr [100], is the physical phenomenon, analogous to electrical current rectification in diodes, in which heat current through a device or medium is not symmetric with respect to the exchange of the baths at the boundaries. In the limiting case the device allows heat to propagate in one direction from the hot to the cold bath while it behaves as a thermal insulator in the opposite direction when the baths are exchanged. In 2002 a paper by Terraneo *et al.* [71] demonstrated heat rectification numerically for a chain of nonlinear oscillators in contact with two thermal baths at different temperatures. Since then, there has been a growing interest in heat rectification [72, 73, 83, 87, 101–108, 110, 151], and the field remains very active because of the potential applications in fundamental science and technology, and the fact that none of the proposals so far appears to be efficient and robust for practical purposes.

Much effort has been devoted to understand the underlying physical mechanism responsible for rectification [101]. In early times some kind of anharmonicity, i.e. non-linear forces, in the substrate potential or in the particle-particle interactions, was identified as a fundamental requisite for rectification [73, 78, 80, 82, 88, 109]. This non-harmonic behavior leads to a temperature dependence of the phonon bands. The match/mismatch of the phonon bands (power spectra) governs the heat transport in the chain, allowing it when the bands match or obstructing it if they mismatch [71, 77]. However, a work by Pereira *et al.* [75] showed that rectification can also be found in effective harmonic systems if two requirements are met: some kind of structural asymmetry, and features that depend on the temperature so they change as the baths are inverted. Indeed, in this article we demonstrate rectification in a minimalistic model of two harmonic oscillators where the coupling to the baths depends on the temperature. This will be justified with a particular physical set up with trapped ions and lasers.

The article is organized as follows. In Section C.2 we describe the physical model and its dynamical equations. In Section C.3 we describe the dynamics of the system in terms of a covariance matrix. We also derive a set of algebraic equations that gives as solution the covariance matrix in the steady state. In Section C.4 we solve the covariance matrix equations and find analytical expressions for the steady-state temperatures of the masses and heat currents. In Section C.5 we

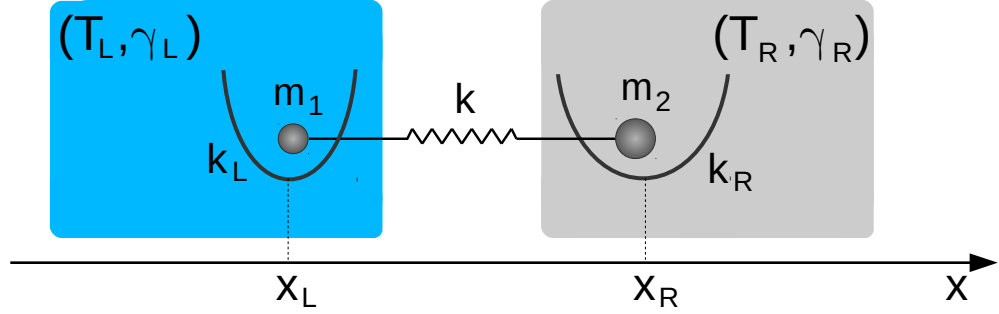


FIGURE C.1: Diagram of the model described in Section C.2. Two ions coupled to each other through a spring constant k . Each ion is harmonically trapped and connected to a bath characterized by its temperature T_i and its friction coefficient γ_i .

relate the parameters of our model to those in a physical set-up of Doppler cooled trapped ions. In Section C.6 we make a parameter sweep looking for configurations which yield high rectification. We also study the power spectra of the oscillators, which confirm the match/mismatch patterns in cases where there is rectification. In Section C.7 we summarize our results and present our conclusions.

C.2 Physical Model

The physical model consists of two masses m_1 and m_2 coupled to each other by a harmonic interaction with spring constant k and natural length x_e . Each of the masses m_1 and m_2 are confined by a harmonic potential with spring constants k_L , k_R and equilibrium positions x_L , x_R respectively (see Fig. C.1). The Hamiltonian describing this model is

$$H = \frac{p_1^2}{2m_1} + \frac{p_2^2}{2m_2} + V(x_1, x_2), \quad (\text{C.1})$$

with $V(x_1, x_2) = \frac{k}{2} (x_1 - x_2 - x_e)^2 + \frac{k_L}{2} (x_1 - x_L)^2 + \frac{k_R}{2} (x_2 - x_R)^2$, where $\{x_i, p_i\}_{i=1,2}$ are the position and momentum of each mass. Switching from the original coordinates x_i to displacements with respect to the equilibrium positions of the system $q_i = x_i - x_i^{eq}$, where x_i^{eq} are the solutions to $\partial_{x_i} V(x_1, x_2) = 0$, the Hamiltonian can

be written as

$$H = \frac{p_1^2}{2m_1} + \frac{p_2^2}{2m_2} + \frac{k + k_L}{2}q_1^2 + \frac{k + k_R}{2}q_2^2 - kq_1q_2 + V(x_1^{eq}, x_2^{eq}). \quad (\text{C.2})$$

This has the form of the Hamiltonian of a system around a stable equilibrium point

$$H = \frac{1}{2}\vec{p}^\top \mathbb{M}^{-1} \vec{p} + \frac{1}{2}\vec{q}^\top \mathbb{K} \vec{q}, \quad (\text{C.3})$$

where $\vec{q} = (q_1, q_2)^\top$, $\vec{p} = (p_1, p_2)^\top$, $\mathbb{M} = \text{diag}(m_1, m_2)$ is the mass matrix of the system and \mathbb{K} is the Hessian matrix of the potential at the equilibrium point, i.e., $\mathbb{K}_{ij} = \partial_{x_i, x_j}^2 V(\vec{x}) \Big|_{\vec{x}=\vec{x}^{eq}}$. In this model $\mathbb{K}_{11} = k + k_L$, $\mathbb{K}_{22} = k + k_R$ and $\mathbb{K}_{12} = \mathbb{K}_{21} = -k$. We shall see later that the generic form (C.3) can be adapted to different physical settings, in particular to two ions in individual traps, or to two ions in a common trap.

The masses are in contact with Langevin baths, which will be denoted as L (for left) and R (for right), at temperatures T_L and T_R for the mass m_1 and m_2 respectively (see Fig. C.1). The equations of motion of the system, taking into account the Hamiltonian and the Langevin baths are

$$\begin{aligned} \dot{q}_1 &= \frac{p_1}{m_1}, \\ \dot{q}_2 &= \frac{p_2}{m_2}, \\ \dot{p}_1 &= -(k + k_L)q_1 + kq_2 - \frac{\gamma_L}{m_1}p_1 + \xi_L(t), \\ \dot{p}_2 &= -(k + k_R)q_2 + kq_1 - \frac{\gamma_R}{m_2}p_2 + \xi_R(t), \end{aligned} \quad (\text{C.4})$$

where γ_L, γ_R are the friction coefficients of the baths and $\xi_L(t), \xi_R(t)$ are Gaussian white-noise-like forces. The Gaussian forces have zero mean ($\langle \xi_L(t) \rangle = \langle \xi_R(t) \rangle = 0$) and satisfy the correlations $\langle \xi_L(t)\xi_R(t') \rangle = 0$, $\langle \xi_L(t)\xi_L(t') \rangle = 2D_L\delta(t-t')$, $\langle \xi_R(t)\xi_R(t') \rangle = 2D_R\delta(t-t')$. D_L and D_R are the diffusion coefficients, which satisfy the fluctuation-dissipation theorem: $D_L = \gamma_L k_B T_L$, $D_R = \gamma_R k_B T_R$ (k_B is the Boltzmann constant).

It is useful to define the phase-space vector $\vec{r}(t) = (\vec{q}, \mathbb{M}^{-1} \vec{p})^\top$ (note that $\vec{v} = \mathbb{M}^{-1} \vec{p}$ is just the velocity vector) so the equations of motion for this vector

are

$$\dot{\vec{r}}(t) = \mathbb{A} \vec{r}(t) + \mathbb{L} \vec{\xi}(t), \quad (\text{C.5})$$

with

$$\begin{aligned} \mathbb{A} &= \begin{pmatrix} \mathbb{1}_{2 \times 2} & \mathbb{1}_{2 \times 2} \\ -\mathbb{M}^{-1}\mathbb{K} & -\mathbb{M}^{-1}\Gamma \end{pmatrix}, \\ \mathbb{L} &= \begin{pmatrix} \mathbb{1}_{2 \times 2} \\ \mathbb{M}^{-1} \end{pmatrix}, \end{aligned} \quad (\text{C.6})$$

and $\vec{\xi}(t) = (\xi_L(t), \xi_R(t))^\top$, $\Gamma = \text{diag}(\gamma_L, \gamma_R)$. $\mathbb{1}_{n \times n}$ and $\mathbb{I}_{n \times n}$ are the n -th dimensional squared 0 matrix and identity matrix respectively. With the vector notation the correlation of the white-noise forces can be written as

$$\langle \vec{\xi}(t) \vec{\xi}(t')^\top \rangle = 2\mathbb{D}\delta(t - t'), \quad (\text{C.7})$$

with $\mathbb{D} = \text{diag}(D_L, D_R)$.

C.3 Covariance matrix in the steady state

We define the covariance matrix of the system as $\mathbb{C}(t) = \langle \vec{r}(t) \vec{r}(t)^\top \rangle$. This matrix is important because the heat transport properties can be extracted from it. In particular, the kinetic temperatures of the masses, $T_1(t)$ and $T_2(t)$, are

$$\begin{aligned} T_1(t) &= \frac{\langle p_1^2(t) \rangle}{m_1 k_B} = \frac{m_1 C_{3,3}(t)}{k_B}, \\ T_2(t) &= \frac{\langle p_2^2(t) \rangle}{m_2 k_B} = \frac{m_2 C_{4,4}(t)}{k_B}. \end{aligned} \quad (\text{C.8})$$

One approach to find the covariance matrix is to solve Eq. (C.5). However, this requires solving the equations explicitly or simulate them numerically many times to find the covariance matrix for the ensemble of simulated stochastic trajectories. Instead, we proceed by looking for an ordinary differential equation that gives the evolution of the covariance matrix as described in [137, 152, 153]. Differentiating

$\mathbb{C}(t)$ with respect to time and using Eq. (C.5) we get

$$\begin{aligned} \frac{d}{dt}\mathbb{C}(t) &= \mathbb{A}\mathbb{C}(t) + \mathbb{C}(t)\mathbb{A}^T \\ &\quad + \mathbb{L} \left\langle \vec{\xi}(t) \vec{r}(t)^T \right\rangle \\ &\quad + \left\langle \vec{r}(t) \vec{\xi}(t)^T \right\rangle \mathbb{L}^T. \end{aligned} \quad (\text{C.9})$$

The solution of Eq. (C.9) allows us to find the local temperatures of the masses as a function of the bath temperatures (Eq. (C.8)) at all times. In particular, we are interested in the covariance matrix in the steady state, i.e., for $t \rightarrow \infty$. According to the Novikov Theorem [133] we can write down the covariance matrix in the steady state without having to integrate the differential equation. We now show how to get the steady-state covariance matrix.

In the steady state, the covariance matrix is constant ($\frac{d}{dt}\mathbb{C}(t) = 0$), therefore it satisfies

$$\begin{aligned} \mathbb{A}\mathbb{C}^{s.s.} + \mathbb{C}^{s.s.}\mathbb{A}^T &= \\ -\mathbb{L} \left\langle \vec{\xi} \vec{r}^T \right\rangle^{s.s.} - \left\langle \vec{r} \vec{\xi}^T \right\rangle^{s.s.} \mathbb{L}^T, \end{aligned} \quad (\text{C.10})$$

with $\{\cdot\}^{s.s.} \equiv \lim_{t \rightarrow \infty} \{\cdot\}(t)$. Equation (C.10) is an algebraic equation whose solution is the steady-state covariance matrix $\mathbb{C}^{s.s.}$. However, the two terms $\left\langle \vec{\xi} \vec{r}^T \right\rangle^{s.s.}$ and $\left\langle \vec{r} \vec{\xi}^T \right\rangle^{s.s.}$ need to be calculated before working out the solution. One approach to calculate $\left\langle \vec{\xi} \vec{r}^T \right\rangle^{s.s.}$ would be to solve Eq. (C.5), but this is exactly what we are trying to avoid. It is here when the Novikov theorem comes useful, since it lets us compute $\left\langle \vec{\xi} \vec{r}^T \right\rangle^{s.s.}$ without having to integrate the equations of motion. Using this theorem and the δ -correlation of the noises, we find the ij -th component of $\left\langle \vec{\xi}(t) \vec{r}(t)^T \right\rangle$,

$$\begin{aligned} \langle \xi_i(t) r_j(t) \rangle &= \sum_{k=1}^2 \int_0^t d\tau \langle \xi_i(t) \xi_k(\tau) \rangle \left\langle \frac{\delta r_j(t)}{\delta \xi_k(\tau)} \right\rangle \\ &= \sum_{k=1}^2 \mathbb{D}_{ik} \lim_{\tau \rightarrow t^-} \left\langle \frac{\delta r_j(t)}{\delta \xi_k(\tau)} \right\rangle, \end{aligned} \quad (\text{C.11})$$

where $\lim_{\tau \rightarrow t^-}$ is the limit when τ goes to t from below. Evaluation of the functional derivative $\delta r_j(t)/\delta \xi_k(\tau)$ for the $\tau \rightarrow t^-$ limit gives

$$\left\langle \vec{\xi}(t) \vec{r}(t)^T \right\rangle = \mathbb{D}\mathbb{L}^T. \quad (\text{C.12})$$

Now, the algebraic equation that gives the steady-state covariance matrix becomes

$$\mathbb{A}\mathbb{C}^{s.s.} + \mathbb{C}^{s.s.}\mathbb{A}^T = -\mathbb{B}, \quad (\text{C.13})$$

with $\mathbb{B} = 2\mathbb{L}\mathbb{D}\mathbb{L}^T$. By definition, the covariance matrix is symmetric, but there are also additional restrictions imposed by the equations of motion and the steady-state condition, which reduce the dimensionality of the problem of solving Eq. (C.13) [154]. Since $d\langle q_i q_j \rangle/dt = 0$ in the steady state, we have

$$\begin{aligned} \langle p_1 q_1 \rangle^{s.s.} &= \langle p_2 q_2 \rangle^{s.s.} = 0, \\ \frac{\langle p_1 q_2 \rangle^{s.s.}}{m_1} &= -\frac{\langle q_1 p_2 \rangle^{s.s.}}{m_2}. \end{aligned} \quad (\text{C.14})$$

Taking (C.14) into account, the steady-state covariance matrix takes the form

$$\mathbb{C}^{s.s.} = \begin{pmatrix} \langle q_1^2 \rangle^{s.s.} & \langle q_1 q_2 \rangle^{s.s.} & 0 & \frac{\langle p_2 q_1 \rangle^{s.s.}}{m_2} \\ \langle q_1 q_2 \rangle^{s.s.} & \langle q_2^2 \rangle^{s.s.} & -\frac{\langle p_2 q_1 \rangle^{s.s.}}{m_2} & 0 \\ 0 & -\frac{\langle p_2 q_1 \rangle^{s.s.}}{m_2} & \frac{\langle p_1^2 \rangle^{s.s.}}{m_1^2} & \frac{\langle p_1 p_2 \rangle^{s.s.}}{m_1 m_2} \\ \frac{\langle p_2 q_1 \rangle^{s.s.}}{m_2} & 0 & \frac{\langle p_1 p_2 \rangle^{s.s.}}{m_1 m_2} & \frac{\langle p_2^2 \rangle^{s.s.}}{m_2^2} \end{pmatrix}. \quad (\text{C.15})$$

The explicit set of equations for the components of $\mathbb{C}^{s.s.}$ can be found in Appendix .1.

C.4 Solutions

In this section we use the solution to Eq. (C.13) to write down the temperatures and currents in the steady state. We use Mathematica to obtain analytic expressions for the temperatures,

$$\begin{aligned} T_1 &= \frac{T_L \mathcal{P}_{1,L}(k) + T_R \mathcal{P}_{1,R}(k)}{\mathcal{D}(k)}, \\ T_2 &= \frac{T_L \mathcal{P}_{2,L}(k) + T_R \mathcal{P}_{2,R}(k)}{\mathcal{D}(k)}, \end{aligned} \quad (\text{C.16})$$

where $\mathcal{D}(k) = \sum_{n=0}^2 \mathcal{D}_n k^n$ and $\mathcal{P}_{i,(L/R)}(k) = \sum_{n=0}^2 a_{i,n,(L/R)} k^n$ are polynomials in the coupling constant k with coefficients

$$\begin{aligned}\mathcal{D}_0 &= a_{1,0,L} = a_{2,0,R} = \gamma_L \gamma_R [h^{(1)} (\gamma_L k_R + \gamma_R k_L) + (m_1 k_R - m_2 k_L)^2], \\ \mathcal{D}_1 &= a_{1,1,L} = a_{2,1,R} = \gamma_L \gamma_R [h^{(0)} h^{(1)} + 2(m_1 - m_2)(m_1 k_R - m_2 k_L)], \\ \mathcal{D}_2 &= h^{(0)} h^{(2)}, \\ a_{1,2,L} &= \gamma_L (m_2 h^{(1)} + \gamma_R (m_1 - m_2)^2), \\ a_{1,2,R} &= h^{(1)} m_1 \gamma_R, \\ a_{2,2,L} &= h^{(1)} m_2 \gamma_L, \\ a_{2,2,R} &= \gamma_R (m_1 h^{(1)} + \gamma_L (m_1 - m_2)^2), \\ a_{1,0,R} &= a_{1,1,R} = a_{2,0,L} = a_{2,1,L} = 0,\end{aligned}\tag{C.17}$$

where $h^{(n)} \equiv \gamma_R m_1^n + \gamma_L m_2^n$. The currents from the baths to the masses [154] are

$$\begin{aligned}J_L &= k_B \frac{\gamma_L}{m_1} (T_L - T_1), \\ J_R &= k_B \frac{\gamma_R}{m_2} (T_R - T_2),\end{aligned}\tag{C.18}$$

with T_i given by Eq. (C.16). Since, in the steady state, $J_L = -J_R$ we will use the shorthand notation $J \equiv J_L$. Substituting Eq. (C.16) into Eq. (C.18) we get for the heat current

$$J = \kappa (T_L - T_R),\tag{C.19}$$

where $\kappa = k_B k^2 \gamma_L \gamma_R h^{(1)} / \mathcal{D}(k)$ acts as an effective thermal conductance, which depends on the parameters of the system, i.e., the masses and spring constants, and also on the friction coefficients of the baths. From Eq. (C.19) it could be thought that inverting the temperatures of the baths would only lead to an exchange of heat currents. However, since the thermal conductance κ depends on the friction coefficients, the exchange of the baths implies a change in its value. Moreover, it is possible to have temperature-dependent friction coefficients, as it happens in the physical set-up of laser-cooled trapped ions described in Section C.5.

C.5 Relation of the Model to a trapped ion set-up

As we mentioned, the parameters k , k_L and k_R can be related to the elements of the Hessian matrix of a system in a stable equilibrium position. In this section we will identify these parameters with the Hessian matrix of a pair of trapped ions. Here we consider two different set-ups: two ions in a collective trap, and two ions in individual traps. In Section C.6 we focus on two ions in individual traps to illustrate the analysis of rectification.

In both set-ups we assume strong confinement in the radial direction, making the effective dynamics one-dimensional. We will also assume that the confinement in the axial direction is purely electrostatic, which makes the effective spring constant independent of the mass of the ions [155]. Additionally, we will relate the temperatures and friction coefficients of the Langevin baths to those corresponding to Doppler cooling.

C.5.1 Collective trap

Consider two ions of unit charge with masses m_1 and m_2 trapped in a collective trap. Assuming strong radial confinement and purely electrostatic axial confinement, both ions feel the same harmonic oscillator potential with trapping constant k_{trap} [155]. The potential describing the system is

$$V_{collective} = \frac{1}{2}k_{trap}(x_1^2 + x_2^2) + \frac{\mathcal{C}}{x_2 - x_1}, \quad (\text{C.20})$$

with $\mathcal{C} = \frac{Q^2}{4\pi\varepsilon_0}$. The equilibrium positions for this potential are

$$x_2^{eq} = -x_1^{eq} = \left(\frac{1}{2}\right)^{2/3} \left(\frac{Q^2}{4\pi\varepsilon_0 k_{trap}}\right)^{1/3}. \quad (\text{C.21})$$

Assuming small oscillations of the ions around the equilibrium positions, the Hessian matrix of the system is

$$\begin{aligned}\mathbb{K}_{1,2} &= -\frac{Q^2}{2\pi\varepsilon_0} \frac{1}{(x_2^{eq} - x_1^{eq})^3} = -k_{trap}, \\ \mathbb{K}_{1,1} &= k_{trap} + \frac{Q^2}{2\pi\varepsilon_0} \frac{1}{(x_2^{eq} - x_1^{eq})^3} = 2k_{trap}, \\ \mathbb{K}_{2,2} &= k_{trap} + \frac{Q^2}{2\pi\varepsilon_0} \frac{1}{(x_2^{eq} - x_1^{eq})^3} = 2k_{trap}.\end{aligned}\quad (\text{C.22})$$

Using Eq. (C.22) we can relate the parameters of this physical set-up to those of the model described in Section C.2 to find

$$k_L = k_R = k = k_{trap}. \quad (\text{C.23})$$

C.5.2 Individual on-site traps

We can make the same assumptions for the axial confinement as in the previous subsection but now each of the ions is in an individual trap with spring constants $k_{trap,L}$ and $k_{trap,R}$ respectively. The potential of the system is

$$\begin{aligned}V_{individual} &= \frac{1}{2}k_{trap,L}(x_1 - x_L)^2 + \frac{1}{2}k_{trap,R}(x_2 - x_R)^2 \\ &\quad + \frac{\mathcal{C}}{x_2 - x_1},\end{aligned}\quad (\text{C.24})$$

where x_L and x_R are the center positions of the on-site traps. The elements of the Hessian matrix in the equilibrium position are

$$\begin{aligned}\mathbb{K}_{1,2} &= -\frac{Q^2}{2\pi\varepsilon_0} \frac{1}{(x_2^{eq} - x_1^{eq})^3}, \\ \mathbb{K}_{1,1} &= k_{trap,L} + \frac{Q^2}{2\pi\varepsilon_0} \frac{1}{(x_2^{eq} - x_1^{eq})^3}, \\ \mathbb{K}_{2,2} &= k_{trap,R} + \frac{Q^2}{2\pi\varepsilon_0} \frac{1}{(x_2^{eq} - x_1^{eq})^3}.\end{aligned}\quad (\text{C.25})$$

Comparing the parameters in Eq. (C.25) with those in the model described in Section C.2 we identify

$$\begin{aligned} k_L &= k_{trap,L}, \\ k_R &= k_{trap,R}, \\ k &= \frac{Q^2}{2\pi\varepsilon_0} \frac{1}{(x_2^{eq} - x_1^{eq})^3}. \end{aligned} \quad (\text{C.26})$$

In this case, the analytic expressions for the equilibrium positions are more complicated. We get for the distance between the equilibrium positions of the ions

$$\begin{aligned} (x_2 - x_1)^{(eq)} &= \frac{1}{3} \Delta x_{LR} \\ &- \frac{1}{6} \left[\frac{2^{2/3} \zeta}{k_{trap,L} k_{trap,R} (k_{trap,L} + k_{trap,R})} \right. \\ &\left. + \frac{2^{4/3} k_{trap,L} k_{trap,R} (k_{trap,L} + k_{trap,R}) (x_R - x_L)^2}{\zeta} \right], \end{aligned} \quad (\text{C.27})$$

where $\Delta x_{LR} = (x_R - x_L)$ and $\zeta = (Y - \eta)^{(1/3)}$, with

$$\begin{aligned} Y &= 3\sqrt{3} \left\{ \mathcal{C} k_{trap,L}^4 k_{trap,R}^4 (k_{trap,L} + k_{trap,R})^7 \times \right. \\ &\left. [4k_{trap,L} k_{trap,R} \Delta x_{LR}^3 + 27\mathcal{C} (k_{trap,L} + k_{trap,R})] \right\}^{(1/2)}, \\ \eta &= k_{trap,L}^2 k_{trap,R}^2 (k_{trap,L} + k_{trap,R})^3 \times \\ &[2k_{trap,L} k_{trap,R} \Delta x_{LR}^3 + 27\mathcal{C} (k_{trap,L} + k_{trap,R})]. \end{aligned} \quad (\text{C.28})$$

In this set-up, the coupling between the ions k can be controlled by changing the distance between the on-site traps.

C.5.3 Optical molasses and Langevin baths

Trapped ions may be cooled down by a pair of counterpropagating lasers which are red-detuned with respect to an internal atomic transition of the ions. This technique is known as Doppler cooling or optical molasses [130, 131, 156, 157]. The off-resonant absorption of laser photons by the ions exerts a damping-like force that slows them down. The spontaneous emission of the ions produces heating due to the random recoil generated by the emitted photons. Both, the friction and recoil force are in balance, and eventually the ion thermalizes to a finite temperature.

Thus the effect of the lasers on the ion is equivalent to a Langevin bath with temperature T_{molass} and friction coefficient γ_{molass} . The temperature and friction coefficients are controlled with the laser intensity I and frequency detuning δ with respect to the selected internal transition by the expressions [121, 130, 131],

$$\begin{aligned}\gamma_{molass}(I, \delta) &= -4\hbar \left(\frac{\delta + \omega_0}{c}\right)^2 \left(\frac{I}{I_0}\right) \frac{2\delta/\Gamma}{[1 + (2\delta/\Gamma)^2]^2}, \\ T_{molass}(\delta) &= -\frac{\hbar\Gamma}{4k_B} \frac{1 + (2\delta/\Gamma)^2}{(2\delta/\Gamma)},\end{aligned}\quad (\text{C.29})$$

where ω_0 is the frequency of the selected internal atomic transition, Γ is the natural width of the excited state, and I_0 is the saturation intensity.

C.6 Looking for rectification

We will say that we observe rectification whenever the heat current J for a configuration of the baths changes when we exchange the baths to \tilde{J} . The important point here is to define what is meant by *exchanging the baths*. We consider that a bath is characterized, not only by its temperature T but also by its coupling to the system by means of the friction coefficient γ , so, exchanging the baths is achieved by exchanging both the temperatures and the friction coefficients, as summarized in Table C.1.

When implementing temperatures and friction coefficients by lasers, this exchange operation is performed by changing the values of the intensities and detunings acting on each ion (Eq. (C.29)). The exchange operation is straightforward when the two ions are either of the same species or isotopes of each other, since the only required action is to exchange the values of the detunings of the lasers without modifying the intensities. However, if we deal with two different species, i.e., with two different atomic transitions, the laser wavelengths and the decay rates depend on the species. Then, exchanging the temperatures by modifying the detunings, keeping the laser intensities constant, does not necessarily imply an exchange of the friction coefficients. Nevertheless it is possible to adjust the laser intensities so that the friction coefficients get exchanged and that is the assumption hereafter. The idea of implementing a bath exchange like this follows the same line of thought as [75], since we are adding a temperature dependent feature to the system -the friction coefficients- that changes as the baths are inverted.

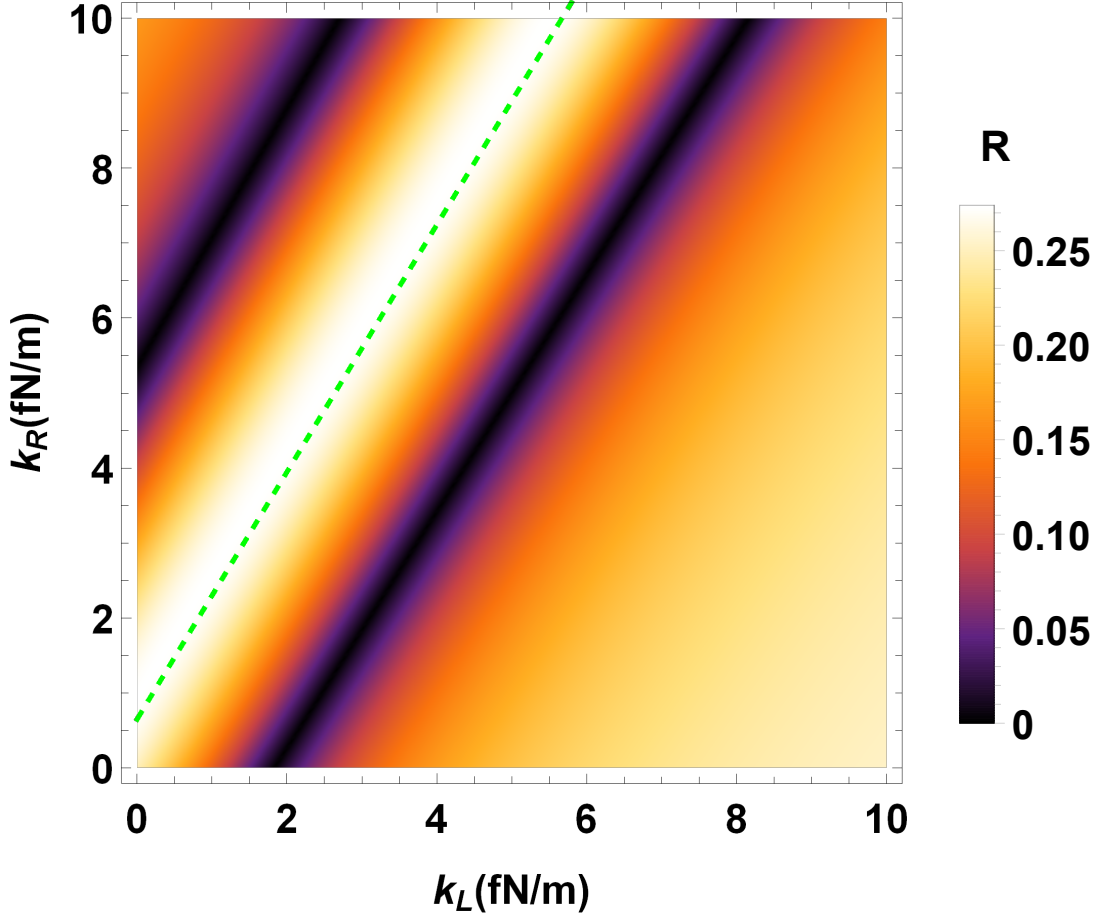


FIGURE C.2: Rectification, R , in the $k_L k_R$ plane for $k = 1.17 \times 10^{-19}$ fN/m, $\gamma_L = 6.75 \times 10^{-22}$ kg/s, and $\gamma_R = 4.64\gamma_L$.

TABLE C.1: Definition of forward and reversed (exchanged) bath configurations.

	forward	reversed
Bath Friction	γ_L, γ_R	$\tilde{\gamma}_L = \gamma_R, \tilde{\gamma}_R = \gamma_L$
Bath Temperature	T_L, T_R	$\tilde{T}_L = T_R, \tilde{T}_R = T_L$

To measure rectification, we will use the rectification coefficient R defined as

$$R = \frac{|J - \tilde{J}|}{\max(J, \tilde{J})}, \quad (\text{C.30})$$

that is, the ratio between the difference of heat currents and the largest one. As defined, $R = 0$ for no asymmetry of the heat currents and $R = 1$ when they are maximally asymmetric.

C.6.1 Parametric exploration

We have explored thoroughly the space formed by the parameters of the model to find asymmetric heat transport, namely, $m_1, m_2, k, k_L, k_R, \gamma_L, \gamma_R$. We have fixed the values of some of the parameters to realistic ones while we have varied the rest. We have set the masses to $m_1 = 24.305$ a.u. and $m_2 = 40.078$ a.u., which correspond to Mg and Ca, whose ions are broadly used in trapped-ion physics. The temperatures are also fixed and, as Eq. (C.19) shows, rectification does not formally depend on the temperature in this model, unless we set the friction coefficients as a function of temperature using Eq. (C.29) explicitly.

Figure C.2 depicts the values of the rectification after sweeping the $k_L k_R$ plane for fixed values of k, γ_L , and γ_R . A remarkable result from this figure is that parallel lines appear alternating minima and maxima of R . With a numerical fitting, we find that the line corresponding to the highest maximum value of R is determined by

$$\frac{k + k_L}{m_1} = \frac{k + k_R}{m_2}. \quad (\text{C.31})$$

In a trapped-ion context the condition (C.31) may be imposed by adjusting the distance of the traps for fixed k_L and k_R . It is also remarkable that when Eq. (C.31) is satisfied, the rectification no longer depends on the spring constants of the model. This last result can be found assuming Eq. (C.31) when calculating the currents with Eq. (C.19) and R with Eq. (C.30),

$$R = \begin{cases} 1 - \frac{a+g}{1+ag} & \text{if } (a+g) < (1+ag) \\ 1 - \frac{1+ag}{a+g} & \text{if } (a+g) > (1+ag) \\ 0 & \text{if } (a+g) = (1+ag), \end{cases} \quad (\text{C.32})$$

where a and g are the mass and friction coefficients ratios

$$\begin{aligned} a &= m_2/m_1, \\ g &= \gamma_R/\gamma_L. \end{aligned} \quad (\text{C.33})$$

The maximal rectification found does not scale with the magnitude of the masses or the friction coefficients, just with their ratios. Besides a high R , it is important to have non-vanishing heat currents [154]. Using again Eq. (C.31) in the expression

for the currents (C.19), the maximum current $J_{\max} = \max(|J|, |\tilde{J}|)$ is

$$J_{\max} = \begin{cases} \frac{k_B g \gamma_L k^2 |T_L - T_R|}{(a+g)(g\gamma_L^2(k_L+k) + k^2 m_1)} & \text{if } (a+g) < (1+ag) \\ \frac{k_B g \gamma_L k^2 |T_L - T_R|}{(1+ag)(g\gamma_L^2(k_L+k) + k^2 m_1)} & \text{if } (a+g) > (1+ag). \end{cases} \quad (\text{C.34})$$

Now we analyze how the parameters a and g affect the maximum current J_{\max} in (C.34). To do this, we can divide the ag plane in four quadrants by the axes $a = 1$ and $g = 1$ (in those axes $R = 0$). In Eq. (C.34) the parameter a appears only in the denominator, thus for a higher a , a smaller current is found. The quadrants with $a < 1$ will be better for achieving large currents. However, g appears both in the numerator and denominator so there is no obvious advantageous quadrant for this parameter.

Equation (C.32) is symmetric upon the transformations $a \leftrightarrow 1/a$ and $g \leftrightarrow 1/g$. Using a logarithmic scale for a and g , the resulting R map will be symmetric with respect to the $a = 1$ and $g = 1$ axes. We can limit ourselves to analyze the quadrant $a > 1$, $g > 1$, as the results in other quadrants will be equivalent upon transformations $a \leftrightarrow 1/a$ and $g \leftrightarrow 1/g$.

Fig. C.3 shows the rectification given by Eq. (C.32) in terms of a and g . Along any diagonal line (parallel to the solid cyan or the dashed green lines), the maximum value is at the center, that is, when $a = g$. However, if we fix a , increasing g always increases R . Although we could increase g arbitrarily to get more rectification this is not a realistic option in a trapped-ion set-up. Since g is defined as the ratio between the friction coefficients, increasing it means making either γ_L go to 0 or γ_R to infinity. Making γ_L go to 0 decouples one of the ions from the bath, so the heat current tends to vanish in any direction. Also, increasing γ_R arbitrarily is impossible since the Doppler cooling friction coefficient as a function of the laser detuning (Eq. (C.29)) is bounded. Although Eq. (C.29) suggests that boosting the laser intensity can also increase the friction coefficient, this is not an option since Eq. (C.29) is just an approximation for low laser intensities. When going to higher intensities, the emission/absorption of photons by the ion is saturated and the friction coefficient reaches a finite value proportional to the width Γ of the excited state [131]. As a compromise between feasibility and high R , we set the ratio between the friction coefficients g to be equal to the mass ratio a . As shown in Fig. C.3, along the solid-cyan and dashed-green diagonal lines the maximum R is achieved for $a = g$. Fig. C.4 shows the rectification in Eq. (C.32)

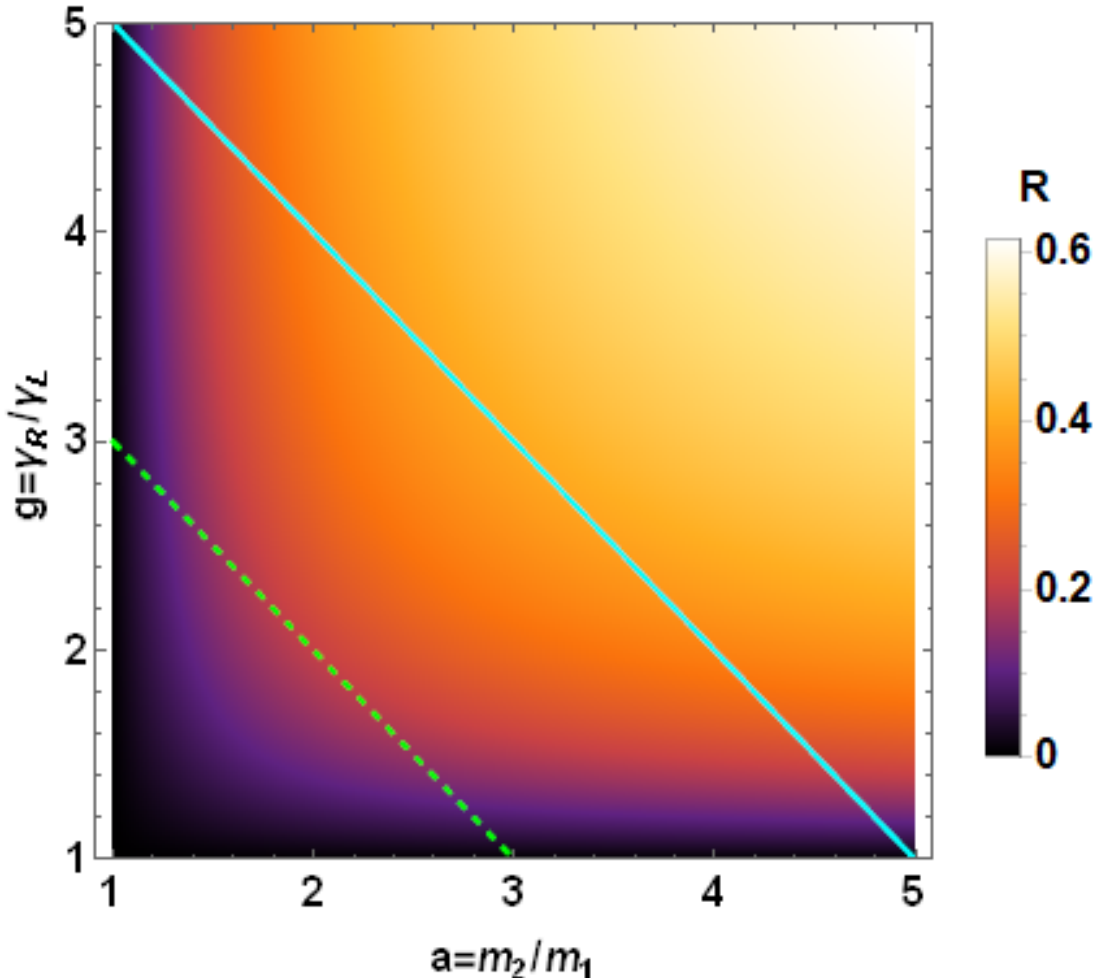


FIGURE C.3: Rectification factor, R , given by Eq. (C.32).

for the line $a = g$. When both parameters are large enough, the rectification goes to 1.

C.6.2 Spectral match/mismatch approach to rectification

The match/mismatch between the power spectra of the particles controls the heat currents in the system [71, 77]. A good match between the power spectra of the two ions in a large range of frequencies yields a higher heat current through the system while the mismatch reduces the heat current. If there is a good match between the spectra of the ions (i.e., their peaks overlap in a broad range of frequencies) for a certain baths configuration, and mismatch when the baths exchange, the system will present heat rectification.

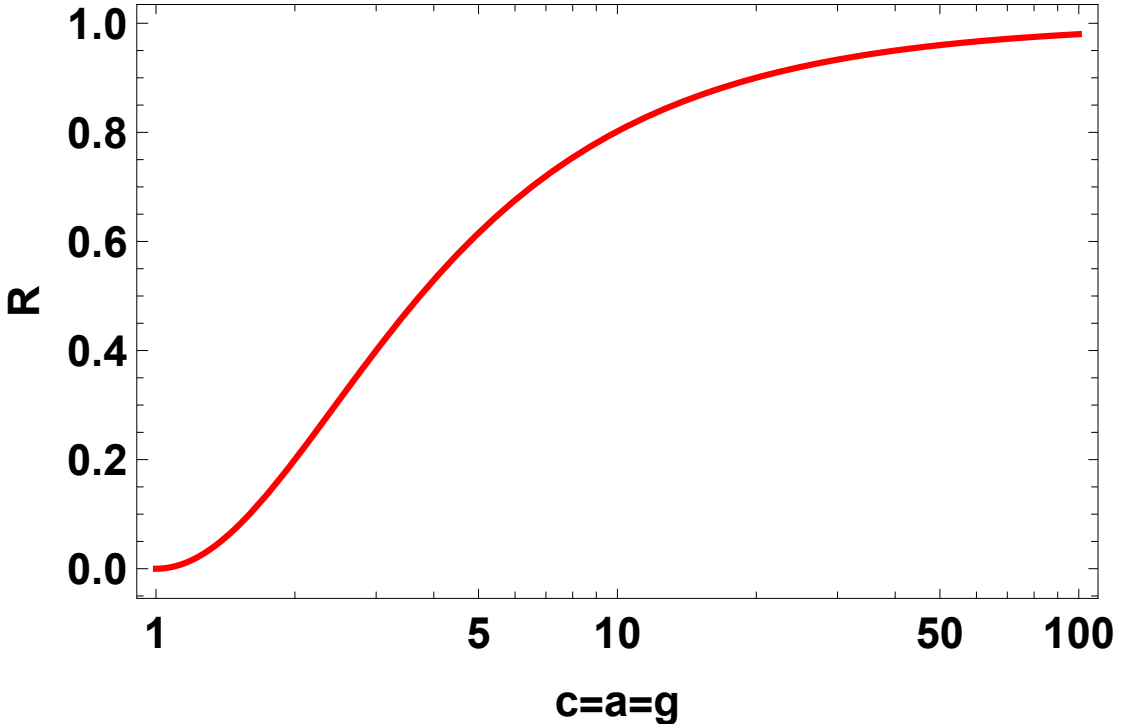


FIGURE C.4: Rectification for different values of $c = m_2/m_1 = \gamma_R/\gamma_L$ when the maximum condition in the $k_L k_R$ plane is satisfied (Eq. (C.31)).

We have studied the phonon spectra of our model for several sets of parameters exhibiting no rectification or strong rectification. The phonon spectra of the ions is calculated through the spectral density matrix. For a real-valued stochastic process $\vec{x}(t)$, its spectral density matrix is defined as [137]

$$\mathbb{S}_{\vec{x}}(\omega) \equiv \left\langle \vec{X}(\omega) \vec{X}^T(-\omega) \right\rangle, \quad (\text{C.35})$$

with $\vec{X}(\omega)$ being the Fourier transform of $\vec{x}(t)$ (we are using the convention of multiplying by a factor of 1 and $\frac{1}{2\pi}$ for the transform and its inverse operation). A justification of the use of the spectral density matrix to understand heat transport arises from the Wiener-Khinchin theorem [137], which says that the correlation matrix of a stationary stochastic process in the steady state is the inverse Fourier transform of its spectral density matrix $\langle \vec{r}(t) \vec{r}^T(t + \tau) \rangle = \mathcal{F}^{-1}[\mathbb{S}_{\vec{r}}(\omega)](\tau)$. This result allows us to write down the covariance matrix in the steady state through the spectral density as

$$\mathbb{C}^{s.s.} = \frac{1}{2\pi} \int_{-\infty}^{\infty} d\omega \mathbb{S}_{\vec{r}}(\omega). \quad (\text{C.36})$$

Eq. (C.36) directly connects the spectral density matrix to the steady-state temperature and, therefore, to the heat currents (in Section C.3 we saw that

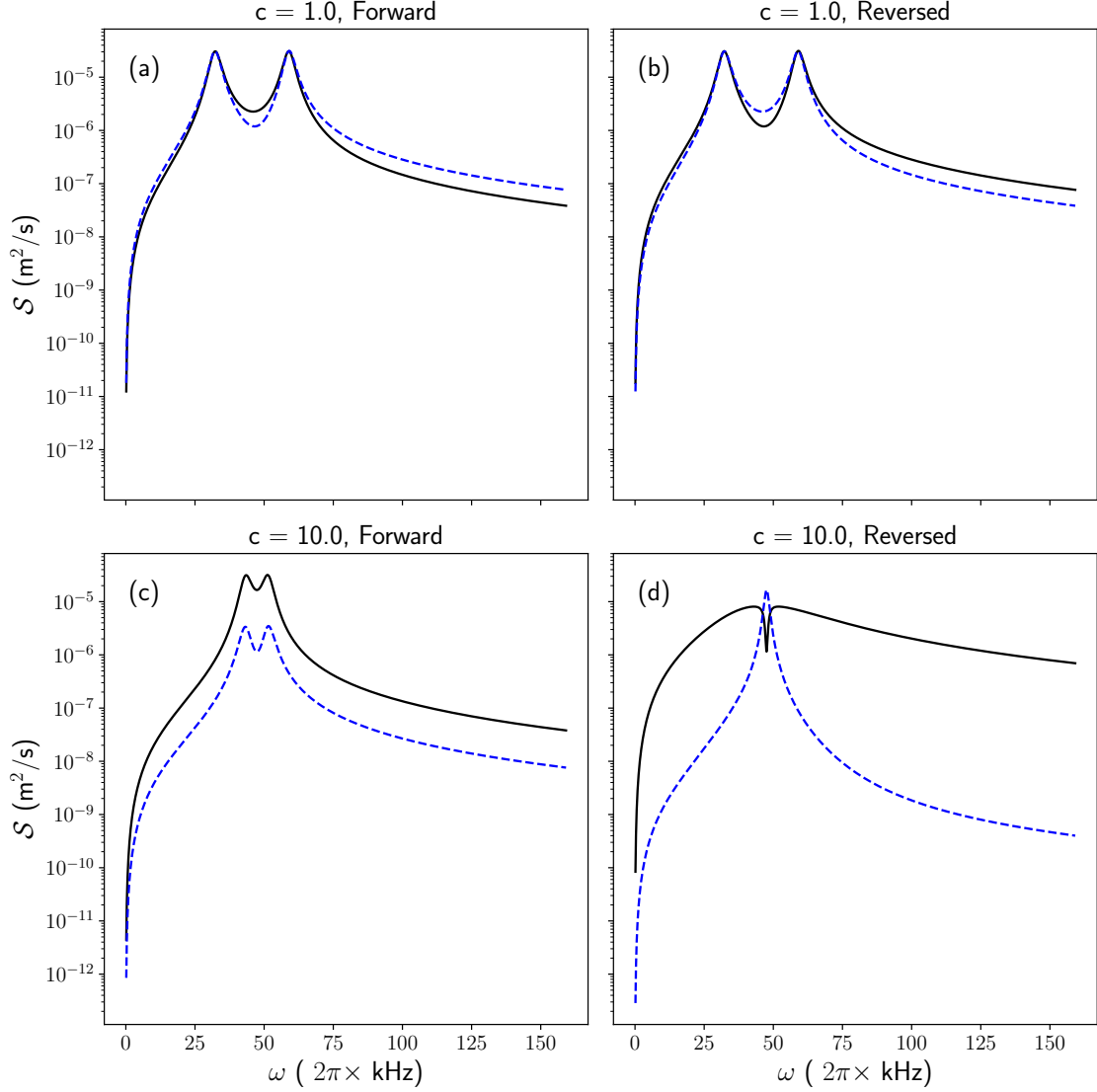


FIGURE C.5: Spectral densities of the velocities of the ions (r_3 and r_4) corresponding to different values of c in Fig. C.4: (a), (b) for $c = 1$ and (c), (d) for $c = 10$. Solid, black lines correspond to the left ion velocity spectral density $\mathbb{S}_{3,3}(\omega)$ and dashed, blue lines correspond to the right ion velocity spectral density $\mathbb{S}_{4,4}(\omega)$. (a) and (b) correspond to $R = 0$: the overlap between the phonon bands is the same in the forward and reversed configurations. (c) and (d) correspond to $R \approx 0.8$: in the forward configuration (c) the phonons match better than in the reversed configuration (d).

$$T_1^{s.s.} = m_1 C_{3,3}^{s.s.}/k_B \text{ and } T_2^{s.s.} = m_2 C_{4,4}^{s.s.}/k_B.$$

For the vector process $\vec{r}(t)$ describing the evolution of our system we have $\vec{R}(\omega) = (i\omega - \mathbb{A})^{-1} \mathbb{L} \vec{\Xi}(\omega)$ with $\vec{\Xi}(\omega)$ being the Fourier transform of the white noise $\vec{\xi}(t)$. Note that $\vec{\Xi}(\omega)$ does not strictly exist, because it is not square-integrable, however its spectral density is $\mathbb{S}_{\vec{\xi}}(\omega) = 2\mathbb{D}$ [137], which is flat as

expected for a white noise. Therefore, the spectral density matrix of the system is

$$\mathbb{S}_{\vec{r}} = 2(\mathbb{A} - i\omega)^{-1} \mathbb{L} \mathbb{D} \mathbb{L}^T (\mathbb{A} + i\omega)^{-T}. \quad (\text{C.37})$$

As we can see in Eq. (C.37), the imaginary part of the eigenvalues of the dynamical matrix \mathbb{A} correspond to the peaks in the spectrum whereas the real part dictates their width. The spectral density matrix of our model is

$$\mathbb{S}_{\vec{r}}(\omega) = 2k_B \frac{\gamma_L T_L \mathbb{S}_L(i\omega) + \gamma_R T_R \mathbb{S}_R(i\omega)}{(m_1 m_2)^2 P_{\mathbb{A}}(i\omega) P_{\mathbb{A}}(-i\omega)}, \quad (\text{C.38})$$

where $P_{\mathbb{A}}(\lambda)$ is the characteristic polynomial of the dynamical matrix \mathbb{A} and $\mathbb{S}_L(\omega)$, $\mathbb{S}_R(\omega)$ are the matrix polynomials in the angular frequency ω whose coefficients are defined in Appendix .2. Equation (C.39) gives the full expressions of the spectral densities for the velocities, $\mathbb{S}_{3,3}(\omega) = \langle R_3(\omega) R_3(-\omega) \rangle$ for the left ion, and $\mathbb{S}_{4,4}(\omega) = \langle R_4(\omega) R_4(-\omega) \rangle$ for the right ion, since they are the elements related to the calculation of the heat current using Eq. (C.36),

$$\begin{aligned} \mathbb{S}_{3,3}(\omega) &= 2k_B \frac{\gamma_R k^2 T_R \omega^2 + \gamma_L T_L [\omega^4 (\gamma_R^2 - 2km_2 - 2k_R m_2) + \omega^2 (k + k_R)^2 + m_2^2 \omega^6]}{(m_1 m_2)^2 P_{\mathbb{A}}(i\omega) P_{\mathbb{A}}(-i\omega)}, \\ \mathbb{S}_{4,4}(\omega) &= 2k_B \frac{\gamma_L k^2 T_L \omega^2 + \gamma_R T_R [\omega^4 (\gamma_L^2 - 2km_1 - 2k_L m_1) + \omega^2 (k + k_L)^2 + m_1^2 \omega^6]}{(m_1 m_2)^2 P_{\mathbb{A}}(i\omega) P_{\mathbb{A}}(-i\omega)}. \end{aligned} \quad (\text{C.39})$$

Figure C.5 depicts a series of plots of the spectra given by Eq. (C.39) that correspond to two points in Fig. C.4. For $c = 1$ (Fig. C.5(a) and (b)) there is no rectification, since the spectra match in the forward (a) and reversed (b) configurations. However, for $c = 10$ ((Fig. C.5(c) and (d))) the picture is very different: there is a good match between the spectra in the forward configuration whereas in the reversed configuration the spectra are less correlated, giving as a result higher rectification ($R \approx 0.8$). Figure C.5 only shows the elements (3,3) and (4,4) in the diagonal of \mathbb{S} but the remaining elements, including off-diagonal ones, exhibit a similar behavior.

C.7 Conclusions

We have studied heat rectification in a model composed of two coupled harmonic oscillators connected to baths. This simple model allows analytical treatment but

still has enough complexity to examine different ingredients that can produce rectification. Our results demonstrate in a simple but realistic system that harmonic systems can rectify heat current if they have features which depend on the temperature [75]. We implement this notion of temperature-dependent features by defining the baths exchange operation as an exchange of both temperatures and coupling parameters of the baths to the system. This kind of temperature-dependent features happens naturally in laser-cooled trapped ion set-ups.

We have also studied the phonon spectra of the system, comparing the match/mismatch of the phonon bands, to reach the conclusion that the band match/mismatch description for heat rectification is also valid for systems which are harmonic, as long as there are temperature-dependent features. We hope this article sheds more light into the topic of heat rectification and that encourages more research regarding its physical implementation on chains of trapped ions.

C.8 acknowledgements

We thank Daniel Alonso for fruitful discussions and comments. This work was supported by the Basque Country Government (Grant No. IT986-16), by Grants PGC2018-101355-B-I00 (MCIU/AEI/FEDER,UE) and FIS2016-80681P, and by the Spanish MICINN and European Union (FEDER) (Grant No. FIS2017-82855-P). M.A.S. acknowledges support by the Basque Government predoctoral program (Grant No. PRE-2019-2-0234).

.1 Full set of steady-state equations for the components of $\mathbb{C}^{s.s.}$

Here we present the full set of equations for the covariance matrix elements in the steady state,

$$\begin{aligned}
& \frac{2k \langle p_2 q_1 \rangle^{s.s.}}{m_1 m_2} + \frac{2\gamma_L \langle p_1^2 \rangle^{s.s.}}{m_1^3} = \frac{2D_L}{m_1^2}, \\
& -\frac{2k \langle p_2 q_1 \rangle^{s.s.}}{m_2^2} + \frac{2\gamma_R \langle p_2^2 \rangle^{s.s.}}{m_2^3} = \frac{2D_R}{m_2^2}, \\
& -\frac{(k_L + k) \langle q_1 q_2 \rangle^{s.s.}}{m_1} + \frac{k \langle q_2^2 \rangle^{s.s.}}{m_1} + \frac{\gamma_L \langle p_2 q_1 \rangle^{s.s.}}{m_1 m_2} + \frac{\langle p_1 p_2 \rangle^{s.s.}}{m_1 m_2} = 0, \\
& \frac{(k_L + k) \langle p_2 q_1 \rangle^{s.s.}}{m_1 m_2} - \frac{(k_R + k) \langle p_2 q_1 \rangle^{s.s.}}{m_2^2} + \frac{\gamma_L \langle p_1 p_2 \rangle^{s.s.}}{m_1^2 m_2} + \frac{\gamma_R \langle p_1 p_2 \rangle^{s.s.}}{m_1 m_2^2} = 0, \\
& -\frac{(k_L + k) \langle q_1^2 \rangle^{s.s.}}{m_1} + \frac{k \langle q_1 q_2 \rangle^{s.s.}}{m_1} + \frac{\langle p_1^2 \rangle^{s.s.}}{m_1^2} = 0, \\
& -\frac{(k_R + k) \langle q_2^2 \rangle^{s.s.}}{m_2} + \frac{k \langle q_1 q_2 \rangle^{s.s.}}{m_2} + \frac{\langle p_2^2 \rangle^{s.s.}}{m_2^2} = 0, \\
& -\frac{(k_R + k) \langle q_1 q_2 \rangle^{s.s.}}{m_2} + \frac{k \langle q_2^2 \rangle^{s.s.}}{m_2} - \frac{\gamma_R \langle p_2 q_1 \rangle^{s.s.}}{m_2^2} + \frac{\langle p_1 p_2 \rangle^{s.s.}}{m_1 m_2} = 0
\end{aligned} \tag{40}$$

.2 Complete expressions for the Spectral Density Matrix

In Section C.6 we used the characteristic polynomial $P_{\mathbb{A}}(\lambda)$ of the dynamical matrix \mathbb{A} for the calculation of the spectral density matrix. $P_{\mathbb{A}}(\lambda)$ is defined as

$$\begin{aligned}
\det(\mathbb{A} - \lambda) &= \lambda^4 \\
&+ \lambda^3 \left(\frac{\gamma_L}{m_1} + \frac{\gamma_R}{m_2} \right) \\
&+ \lambda^2 \frac{(\gamma_L \gamma_R + m_2(k + k_L) + m_1(k + k_R))}{m_1 m_2} \\
&+ \lambda \frac{(\gamma_R(k + k_L) + \gamma_L(k + k_R))}{m_1 m_2} \\
&+ \frac{k(k_L + k_R) + k_L k_R}{m_1 m_2}.
\end{aligned} \tag{41}$$

We also used the polynomials $\mathbb{S}_L(\lambda)$ and $\mathbb{S}_R(\lambda)$, which are defined as $\mathbb{S}_L(\lambda) = \sum_{n=0}^6 \lambda^n \sim_{L,n}$ and $\mathbb{S}_R(\lambda) = \sum_{n=0}^6 \lambda^n \sim_{R,n}$. There are 14 different polynomial coefficients, which are 4×4 matrices, which makes very cumbersome to include them in the main text. This is the full list of coefficients,

$$\begin{aligned}
\sim_{L,0} &= \begin{pmatrix} (k+k_R)^2 & k(k+k_R) & 0 & 0 \\ k(k+k_R) & k^2 & 0 & 0 \\ 0 & 0 & 0 & 0 \\ 0 & 0 & 0 & 0 \end{pmatrix}, & \sim_{R,0} &= \begin{pmatrix} k^2 & k(k+k_L) & 0 & 0 \\ k(k+k_L) & (k+k_L)^2 & 0 & 0 \\ 0 & 0 & 0 & 0 \\ 0 & 0 & 0 & 0 \end{pmatrix} \\
\sim_{L,1} &= \begin{pmatrix} 0 & k\gamma_R & -(k+k_R)^2 & -k(k+k_R) \\ -k\gamma_R & 0 & -k(k+k_R) & -k^2 \\ (k+k_R)^2 & k(k+k_R) & 0 & 0 \\ k(k+k_R) & k^2 & 0 & 0 \end{pmatrix}, & \sim_{R,1} &= \begin{pmatrix} 0 & -k\gamma_L & 0 & 0 \\ k\gamma_L & 0 & 0 & 0 \\ k^2 & k(k+k_L) & 0 & 0 \\ k(k+k_L) & (k+k_L)^2 & 0 & 0 \end{pmatrix} \\
\sim_{L,2} &= \begin{pmatrix} 2(k+k_R)m_2 - \gamma_R^2 & km_2 & 0 & -k\gamma_R \\ km_2 & 0 & k\gamma_R & 0 \\ 0 & k\gamma_R & -(k+k_R)^2 & -k(k+k_R) \\ -k\gamma_R & 0 & -k(k+k_R) & -k^2 \end{pmatrix}, & \sim_{R,2} &= \begin{pmatrix} 0 & km_1 & 0 & 0 \\ km_1 & 2(k+k_L)m_1 - \gamma_L^2 & 0 & 0 \\ 0 & -k\gamma_L & 0 & 0 \\ k\gamma_L & 0 & 0 & 0 \end{pmatrix} \\
\sim_{L,3} &= \begin{pmatrix} 0 & 0 & \gamma_R^2 - 2(k+k_R)m_2 & -km_2 \\ 0 & 0 & -km_2 & 0 \\ 2(k+k_R)m_2 - \gamma_R^2 & km_2 & 0 & -k\gamma_R \\ km_2 & 0 & k\gamma_R & 0 \end{pmatrix}, & \sim_{R,3} &= \begin{pmatrix} 0 & 0 & 0 & 0 \\ 0 & 0 & 0 & 0 \\ 0 & km_1 & 0 & 0 \\ km_1 & 2(k+k_L)m_1 - \gamma_L^2 & 0 & 0 \end{pmatrix} \\
\sim_{L,4} &= \begin{pmatrix} m_2^2 & 0 & 0 & 0 \\ 0 & 0 & 0 & 0 \\ 0 & 0 & \gamma_R^2 - 2(k+k_R)m_2 & -km_2 \\ 0 & 0 & -km_2 & 0 \end{pmatrix}, & \sim_{R,4} &= \begin{pmatrix} 0 & 0 & 0 & 0 \\ 0 & m_1^2 & 0 & 0 \\ 0 & 0 & 0 & 0 \\ 0 & 0 & -km_1 & \gamma_L^2 - 2(k+k_L)m_1 \end{pmatrix} \\
\sim_{L,5} &= \begin{pmatrix} 0 & 0 & -m_2^2 & 0 \\ 0 & 0 & 0 & 0 \\ m_2^2 & 0 & 0 & 0 \\ 0 & 0 & 0 & 0 \end{pmatrix}, & \sim_{R,5} &= \begin{pmatrix} 0 & 0 & 0 & 0 \\ 0 & 0 & 0 & -m_1^2 \\ 0 & 0 & 0 & 0 \\ 0 & m_1^2 & 0 & 0 \end{pmatrix}, \\
\sim_{L,6} &= \begin{pmatrix} 0 & 0 & 0 & 0 \\ 0 & 0 & 0 & 0 \\ 0 & 0 & -m_2^2 & 0 \\ 0 & 0 & 0 & 0 \end{pmatrix}, & \sim_{R,6} &= \begin{pmatrix} 0 & 0 & 0 & 0 \\ 0 & 0 & 0 & 0 \\ 0 & 0 & 0 & 0 \\ 0 & 0 & 0 & -m_1^2 \end{pmatrix}.
\end{aligned}
\tag{42}$$

Conclusions

My pleasure.

Appendix

Appendix A

Interaction versus asymmetry for adiabatic following

Extra information to add to your thesis.

Bibliography

- [1] J. Muga, J. Palao, B. Navarro, and I. Egusquiza, “*Complex absorbing potentials*”, [Physics Reports](#) **395**, 357 - 426 (2004).
- [2] A. Ruschhaupt, F. Delgado, and J. G. Muga, “*Physical realization of -symmetric potential scattering in a planar slab waveguide*”, [Journal of Physics A: Mathematical and General](#) **38**, L171–L176 (2005).
- [3] J. Taylor, *Scattering Theory: Quantum Theory on Nonrelativistic Collisions*. Wiley, 1972.
- [4] A. Mostafazadeh, “*Pseudo-Hermitian Representation of Quantum Mechanics*”, [International Journal of Geometric Methods in Modern Physics](#) **07**, 1191 (2010).
- [5] M. Znojil, *Non-self-adjoint operators in quantum physics: ideas, people, and trends*, ch. 1, pp. 7–58. Wiley, 2015.
- [6] S. Nixon and J. Yang, “*All-real spectra in optical systems with arbitrary gain-and-loss distributions*”, [Phys. Rev. A](#) **93**, 031802 (2016).
- [7] S. Nixon and J. Yang, “*Nonlinear light behaviors near phase transition in non-parity-time-symmetric complex waveguides*”, [Opt. Lett.](#) **41**, 2747–2750 (2016).
- [8] Y. Xu, L. Feng, M. Lu, and Y. Chen, “*Unidirectional Transmission Based on a Passive PT Symmetric Grating With a Nonlinear Silicon Distributed Bragg Reflector Cavity*”, [IEEE Photonics Journal](#) **6**, 1-7 (2014).
- [9] Y. Huang, C. Min, and G. Veronis, “*Broadband near total light absorption in non-PT-symmetric waveguide-cavity systems*”, [Opt. Express](#) **24**, 22219–22231 (2016).

- [10] Z. Lin, H. Ramezani, T. Eichelkraut, T. Kottos, H. Cao, and D. N. Christodoulides, “*Unidirectional Invisibility Induced by \mathcal{PT} -Symmetric Periodic Structures*”, *Phys. Rev. Lett.* **106**, 213901 (2011).
- [11] X. Yin and X. Zhang, “*Unidirectional light propagation at exceptional points*”, *Nature Materials* **12**, 175–177 (2013).
- [12] J. P. Palao, J. G. Muga, and R. Sala, “*Composite Absorbing Potentials*”, *Phys. Rev. Lett.* **80**, 5469–5472 (1998).
- [13] S. Brouard, D. Macias, and J. G. Muga, “*Perfect absorbers for stationary and wavepacket scattering*”, *Journal of Physics A: Mathematical and General* **27**, L439–L445 (1994).
- [14] J. Palao and J. Muga, “*A simple construction procedure of absorbing potentials*”, *Chemical Physics Letters* **292**, 1 - 6 (1998).
- [15] R. Snieder, “*The role of the Born approximation in nonlinear inversion*”, *Inverse Problems* **6**, 247–266 (1990).
- [16] A. Mostafazadeh, “*Transfer matrices as nonunitary S matrices, multimode unidirectional invisibility, and perturbative inverse scattering*”, *Phys. Rev. A* **89**, 012709 (2014).
- [17] S. A. R. Horsley, M. Artoni, and G. C. La Rocca, “*Spatial Kramers–Kronig relations and the reflection of waves*”, *Nature Photonics* **9**, 436–439 (2015).
- [18] S. Longhi, “*A unidirectionally invisible $\mathcal{P}\mathcal{T}$ -symmetric complex crystal with arbitrary thickness*”, *Journal of Physics A: Mathematical and Theoretical* **47**, 485302 (2014).
- [19] V. V. Konotop, J. Yang, and D. A. Zezyulin, “*Nonlinear waves in \mathcal{PT} -symmetric systems*”, *Rev. Mod. Phys.* **88**, 035002 (2016).
- [20] Z. Yu and S. Fan, “*Complete optical isolation created by indirect interband photonic transitions*”, *Nature Photonics* **3**, 91–94 (2009).
- [21] S. Longhi, “*Rapidly oscillating scatteringless non-Hermitian potentials and the absence of Kapitza stabilization*”, *EPL (Europhysics Letters)* **118**, 20004 (2017).

- [22] V. V. Konotop and D. A. Zezyulin, “*Phase transition through the splitting of self-dual spectral singularity in optical potentials*”, Opt. Lett. **42**, 5206–5209 (2017).
- [23] Y. V. Kartashov, V. V. Konotop, and D. A. Zezyulin, “*CPT-symmetric spin-orbit-coupled condensate*”,.
- [24] D. A. Zezyulin, Y. V. Kartashov, and V. V. Konotop, “*CPT-symmetric coupler with intermodal dispersion*”, Opt. Lett. **42**, 1273–1276 (2017).
- [25] A. Ruschhaupt, J. A. Damborenea, B. Navarro, J. G. Muga, and G. C. Hegerfeldt, “*Exact and approximate complex potentials for modelling time observables*”, Europhysics Letters (EPL) **67**, 1–7 (2004).
- [26] H. Feshbach, “*Unified theory of nuclear reactions*”, Annals of Physics **5**, 357 - 390 (1958).
- [27] H. Feshbach, “*A unified theory of nuclear reactions. II*”, Annals of Physics **19**, 287 - 313 (1962).
- [28] C. M. Bender and S. Boettcher, “*Real Spectra in Non-Hermitian Hamiltonians Having PT Symmetry*”, Phys. Rev. Lett. **80**, 5243–5246 (1998).
- [29] A. Guo, G. J. Salamo, D. Duchesne, R. Morandotti, M. Volatier-Ravat, V. Aimez, G. A. Siviloglou, and D. N. Christodoulides, “*Observation of PT-Symmetry Breaking in Complex Optical Potentials*”, Phys. Rev. Lett. **103**, 093902 (2009).
- [30] A. Ruschhaupt, T. Dowdall, M. A. Simón, and J. G. Muga, “*Asymmetric scattering by non-Hermitian potentials*”, EPL (Europhysics Letters) **120**, 20001 (2017).
- [31] A. Mostafazadeh, “*Pseudo-Hermiticity versus PT symmetry: The necessary condition for the reality of the spectrum of a non-Hermitian Hamiltonian*”, Journal of Mathematical Physics **43**, 205-214 (2002), <https://doi.org/10.1063/1.1418246>.
- [32] L. S. Simeonov and N. V. Vitanov, “*Dynamical invariants for pseudo-Hermitian Hamiltonians*”, Phys. Rev. A **93**, 012123 (2016).

- [33] B. BAGCHI, C. QUESNE, and M. ZNOJIL, “GENERALIZED CONTINUITY EQUATION AND MODIFIED NORMALIZATION IN PT -SYMMETRIC QUANTUM MECHANICS”, *Modern Physics Letters A* **16**, 2047-2057 (2001), <https://doi.org/10.1142/S0217732301005333>.
- [34] D. A. Zezyulin and V. V. Konotop, “Stationary modes and integrals of motion in nonlinear lattices with a \mathcal{PT} -symmetric linear part”, *Journal of Physics A: Mathematical and Theoretical* **46**, 415301 (2013).
- [35] E. P. Wigner, *Group theory and its application to the quantum mechanics of atomic spectra*. Pure Appl. Phys. Academic Press, New York, NY, 1959. <https://cds.cern.ch/record/102713>. Trans. from the German.
- [36] H. Rose, “A course on finite groups”,.
- [37] A. Ruschhaupt and J. G. Muga, “Atom diode: A laser device for a unidirectional transmission of ground-state atoms”, *Phys. Rev. A* **70**, 061604 (2004).
- [38] H. R. Lewis and W. B. Riesenfeld, “An Exact Quantum Theory of the Time-Dependent Harmonic Oscillator and of a Charged Particle in a Time-Dependent Electromagnetic Field”, *Journal of Mathematical Physics* **10**, 1458-1473 (1969), <https://doi.org/10.1063/1.1664991>.
- [39] S. Ibáñez, S. Martínez-Garaot, X. Chen, E. Torrontegui, and J. G. Muga, “Shortcuts to adiabaticity for non-Hermitian systems”, *Phys. Rev. A* **84**, 023415 (2011).
- [40] E. Torrontegui, S. Ibáñez, S. Martínez-Garaot, M. Modugno, A. del Campo, D. Guéry-Odelin, A. Ruschhaupt, X. Chen, and J. G. Muga, “Chapter 2 - Shortcuts to Adiabaticity”, in *Advances in Atomic, Molecular, and Optical Physics*, E. Arimondo, P. R. Berman, and C. C. Lin, eds., volume 62 of *Advances In Atomic, Molecular, and Optical Physics*, pp. 117 – 169. Academic Press, 2013. <http://www.sciencedirect.com/science/article/pii/B9780124080904000025>.
- [41] J. Alexandre, P. Millington, and D. Seynaeve, “Symmetries and conservation laws in non-Hermitian field theories”, *Phys. Rev. D* **96**, 065027 (2017).

- [42] F. Correa, V. Jakubský, and M. S. Plyushchay, “ *PT -symmetric invisible defects and confluent Darboux-Crum transformations*”, *Phys. Rev. A* **92**, 023839 (2015).
- [43] J. M. Guilarte and M. S. Plyushchay, “*Perfectly invisible PT -\$\mathcal{P}\mathcal{T}-symmetric zero-gap systems, conformal field theoretical kinks, and exotic nonlinear supersymmetry*”, *Journal of High Energy Physics* **2017**, 61 (2017).
- [44] L. Deák and T. Fülöp, “*Reciprocity in quantum, electromagnetic and other wave scattering*”, *Annals of Physics* **327**, 1050 - 1077 (2012).
- [45] P. Chen and Y. D. Chong, “*Pseudo-Hermitian Hamiltonians generating waveguide mode evolution*”, *Phys. Rev. A* **95**, 062113 (2017).
- [46] S. Longhi, “*Parity-time symmetry meets photonics: A new twist in non-Hermitian optics*”, *EPL (Europhysics Letters)* **120**, 64001 (2017).
- [47] L. Feng, R. El-Ganainy, and L. Ge *Nature Photonics* **11**, 752–762 (2017).
- [48] R. El-Ganainy, K. G. Makris, M. Khajavikhan, Z. H. Musslimani, S. Rotter, and D. N. Christodoulides, “*Non-Hermitian physics and PT symmetry*”, *Nature Physics* **14**, 11–19 (2018).
- [49] N. Moiseyev, *Non-Hermitian Quantum Mechanics*. Cambridge University Press, Cambridge, UK, 2011.
- [50] J. Aguilar and J.-M. Combes, “*A class of analytic perturbations for one-body Schrödinger Hamiltonians*”, *Communications in Mathematical Physics* **22**, 269–279 (1971).
- [51] E. Balslev and J.-M. Combes, “*Spectral properties of many-body Schrödinger operators with dilatation-analytic interactions*”, *Communications in Mathematical Physics* **22**, 280–294 (1971).
- [52] I. Rotter, “*A non-Hermitian Hamilton operator and the physics of open quantum systems*”, *Journal of Physics A: Mathematical and Theoretical* **42**, 153001 (2009).
- [53] V. M. Martinez Alvarez, J. E. Barrios Vargas, M. Berdakin, and L. E. F. Foa Torres, “*Topological states of non-Hermitian systems*”, *Eur. Phys. J. Special Topics* (2018).

- [54] J. Yang, “*Classes of non-parity-time-symmetric optical potentials with exceptional-point-free phase transitions*”, Optics letters **42**, 4067–4070 (2017).
- [55] F. Cannata, J.-P. Dedonder, and A. Ventura, “*Scattering in PT-symmetric quantum mechanics*”, Annals of Physics **322**, 397 - 433 (2007).
- [56] A. Mostafazadeh, “*Spectral Singularities of Complex Scattering Potentials and Infinite Reflection and Transmission Coefficients at Real Energies*”, Phys. Rev. Lett. **102**, 220402 (2009).
- [57] A. Mostafazadeh, “*Invisibility and \mathcal{PT} symmetry*”, Phys. Rev. A **87**, 012103 (2013).
- [58] A. Mostafazadeh, “*Pseudo-Hermiticity versus PT-symmetry III: Equivalence of pseudo-Hermiticity and the presence of antilinear symmetries*”, Journal of Mathematical Physics **43**, 3944–3951 (2002).
- [59] M. Hiller, T. Kottos, and A. Ossipov, “*Bifurcations in resonance widths of an open Bose-Hubbard dimer*”, Phys. Rev. A **73**, 063625 (2006).
- [60] H. Zhong, W. Hai, G. Lu, and Z. Li, “*Incoherent control in a non-Hermitian Bose-Hubbard dimer*”, Phys. Rev. A **84**, 013410 (2011).
- [61] C. M. Bender and P. D. Mannheim, “*PT symmetry and necessary and sufficient conditions for the reality of energy eigenvalues*”, Physics Letters A **374**, 1616–1620 (2010).
- [62] M. A. Simón, A. Buendía, and J. G. Muga, “*Symmetries and Invariants for Non-Hermitian Hamiltonians*”, Mathematics **6**, 111 (2018).
- [63] Y. V. Popov, A. Galstyan, B. Piraux, P. F. O Mahony, F. Mota-Furtado, P. Decleva, and O. Chuluunbaatar, “*Separable Potentials Model for Atoms and Molecules in Strong UltrashortLaserPulses*”, in *Progress in Photon Science*, K. Yamanouchi, S. Tunik, and V. Makarov, eds., ch. 11, pp. 221–242. Springer, Cham, Switzerland, 2019.
- [64] J. G. Muga and R. F. Snider, “*SCATTERING BY A SEPARABLE POTENTIAL IN ONE DIMENSION*”, Canadian Journal of Physics **68**, 403-410 (1990).

- [65] J. G. Muga, G. W. Wei, and R. F. Snider, “*Survival probability for the Yamaguchi potential*”, Annals of Physics **252**, 336–356 (1996).
- [66] J. G. Muga, G. W. Wei, and R. F. Snider, “*Short-time behaviour of the quantum survival probability*”, EPL (Europhysics Letters) **35**, 247 (1996).
- [67] J. G. Muga and J. P. Palao, “*Solvable model for quantum wavepacket scattering in one dimension*”, Journal of Physics A: Mathematical and General **31**, 9519 (1998).
- [68] J. G. Muga and J. P. Palao, “*Negative time delays in one dimensional absorptive collisions*”, Annalen der Physik **7**, 671–678 (1998).
- [69] L. Hlophe and C. Elster, “*Separable representation of multichannel nucleon-nucleus optical potentials*”, Phys. Rev. C **95**, 054617 (2017).
- [70] A. Mostafazadeh, “*Pseudo-Hermiticity versus PT-symmetry. II. A complete characterization of non-Hermitian Hamiltonians with a real spectrum*”, Journal of Mathematical Physics **43**, 2814–2816 (2002).
- [71] M. Terraneo, M. Peyrard, and G. Casati, “*Controlling the Energy Flow in Nonlinear Lattices: A Model for a Thermal Rectifier*”, Phys. Rev. Lett. **88**, 094302 (2002).
- [72] N. Roberts and D. Walker, “*A review of thermal rectification observations and models in solid materials*”, International Journal of Thermal Sciences **50**, 648 - 662 (2011).
- [73] N. Li, J. Ren, L. Wang, G. Zhang, P. Hänggi, and B. Li, “*Colloquium: Phononics: Manipulating heat flow with electronic analogs and beyond*”, Rev. Mod. Phys. **84**, 1045–1066 (2012).
- [74] S. Chen, E. Pereira, and G. Casati, “*Ingredients for an efficient thermal diode*”, EPL (Europhysics Letters) **111**, 30004 (2015).
- [75] E. Pereira, “*Requisite ingredients for thermal rectification*”, Phys. Rev. E **96**, 012114 (2017).
- [76] M. G. Raizen, A. M. Dudarev, Q. Niu, and N. J. Fisch, “*Compression of Atomic Phase Space Using an Asymmetric One-Way Barrier*”, Phys. Rev. Lett. **94**, 053003 (2005).

- [77] B. Li, L. Wang, and G. Casati, “*Thermal Diode: Rectification of Heat Flux*”, *Phys. Rev. Lett.* **93**, 184301 (2004).
- [78] B. Hu, L. Yang, and Y. Zhang, “*Asymmetric Heat Conduction in Nonlinear Lattices*”, *Phys. Rev. Lett.* **97**, 124302 (2006).
- [79] M. Peyrard, “*The design of a thermal rectifier*”, *Europhysics Letters (EPL)* **76**, 49–55 (2006).
- [80] G. Benenti, G. Casati, C. Mejía-Monasterio, and M. Peyrard, *From Thermal Rectifiers to Thermoelectric Devices*, pp. 365–407. Springer International Publishing, Cham, 2016.
https://doi.org/10.1007/978-3-319-29261-8_10.
- [81] B. Hu, D. He, L. Yang, and Y. Zhang, “*Thermal rectifying effect in macroscopic size*”, *Phys. Rev. E* **74**, 060201 (2006).
- [82] N. Zeng and J.-S. Wang, “*Mechanisms causing thermal rectification: The influence of phonon frequency, asymmetry, and nonlinear interactions*”, *Phys. Rev. B* **78**, 024305 (2008).
- [83] C. W. Chang, D. Okawa, A. Majumdar, and A. Zettl, “*Solid-State Thermal Rectifier*”, *Science* **314**, 1121–1124 (2006).
- [84] E. Pereira and R. R. Ávila, “*Increasing thermal rectification: Effects of long-range interactions*”, *Phys. Rev. E* **88**, 032139 (2013).
- [85] Y. Wang, A. Vallabhaneni, J. Hu, B. Qiu, Y. P. Chen, and X. Ruan, “*Phonon Lateral Confinement Enables Thermal Rectification in Asymmetric Single-Material Nanostructures*”, *Nano Letters* **14**, 592–596 (2014), <http://dx.doi.org/10.1021/nl403773f>.
- [86] H. Wang, S. Hu, K. Takahashi, X. Zhang, H. Takamatsu, and J. Chen, “*Suspended Monolayer Graphene*”, *Nature Comm.* **8**, 15483 (2016).
- [87] K. Joulain, J. Drevillon, Y. Ezzahri, and J. Ordonez-Miranda, “*Quantum Thermal Transistor*”, *Phys. Rev. Lett.* **116**, 200601 (2016).
- [88] G. Katz and R. Kosloff, “*Quantum Thermodynamics in Strong Coupling: Heat Transport and Refrigeration*”, *Entropy* **18**, (2016).
- [89] L. Wang, Z. Wu, and L. Xu, “*Super heat diffusion in one-dimensional momentum-conserving nonlinear lattices*”, *Phys. Rev. E* **91**, 062130 (2015).

- [90] G. J. Martyna, M. L. Klein, and M. Tuckerman, “*Nosé–Hoover chains: The canonical ensemble via continuous dynamics*”, *The Journal of Chemical Physics* **97**, 2635–2643 (1992), <http://dx.doi.org/10.1063/1.463940>.
- [91] G. Casati, J. Ford, F. Vivaldi, and W. M. Visscher, “*One-Dimensional Classical Many-Body System Having a Normal Thermal Conductivity*”, *Phys. Rev. Lett.* **52**, 1861–1864 (1984).
- [92] B. Hu, B. Li, and H. Zhao, “*Heat conduction in one-dimensional chains*”, *Phys. Rev. E* **57**, 2992–2995 (1998).
- [93] S. Lepri, R. Livi, and A. Politi, “*Heat Conduction in Chains of Nonlinear Oscillators*”, *Phys. Rev. Lett.* **78**, 1896–1899 (1997).
- [94] S. Lepri, R. Livi, and A. Politi, “*Thermal conduction in classical low-dimensional lattices*”, *Physics Reports* **377**, 1 - 80 (2003).
- [95] P. A. Skordos and W. H. Zurek, “*Maxwell’s demon, rectifiers, and the second law: Computer simulation of Smoluchowski’s trapdoor*”, *American Journal of Physics* **60**, 876-882 (1992),
<http://dx.doi.org/10.1119/1.17007>.
- [96] A. Ruschhaupt, J. G. Muga, and M. G. Raizen, “*Improvement by laser quenching of an ‘atom diode’: a one-way barrier for ultra-cold atoms*”, *Journal of Physics B: Atomic, Molecular and Optical Physics* **39**, L133 (2006).
- [97] I. Bloch, “*Ultracold Quantum Gases in Optical Lattices*”, *Nature Physics* **1**, 23 (2005).
- [98] W. S. Bakr, J. I. Gillen, A. Peng, S. Fölling, and M. Greiner, “*A quantum gas microscope for detecting single atoms in a Hubbard-regime optical lattice*”, *Nature* **462**, 74 (2009).
- [99] C. Gollub, P. V. D. Hoff, M. Kowalewski, U. Troppmann, and R. D. Vivie-Riedle, *Vibrational Energy Transfer Through Molecular Chains: An Approach Toward Scalable Information Processing*, ch. 13, pp. 371–402. John Wiley & Sons, Inc., 2014.
- [100] C. Starr, “*The Copper Oxide Rectifier*”, *Physics* **7**, 15-19 (1936),
<https://doi.org/10.1063/1.1745338>.

- [101] E. Pereira, “*Thermal rectification in classical and quantum systems: Searching for efficient thermal diodes*”, *EPL (Europhysics Letters)* **126**, 14001 (2019).
- [102] Z.-Q. Ye and B.-Y. Cao, “*Thermal rectification at the bimaterial nanocontact interface*”, *Nanoscale* **9**, 11480-11487 (2017).
- [103] L. Wang and B. Li, “*Thermal Memory: A Storage of Phononic Information*”, *Phys. Rev. Lett.* **101**, 267203 (2008).
- [104] L. Wang and B. Li, “*Thermal Logic Gates: Computation with Phonons*”, *Phys. Rev. Lett.* **99**, 177208 (2007).
- [105] B. Li, L. Wang, and G. Casati, “*Negative differential thermal resistance and thermal transistor*”, *Applied Physics Letters* **88**, 143501 (2006).
- [106] W. Kobayashi, Y. Teraoka, and I. Terasaki, “*An oxide thermal rectifier*”, *Applied Physics Letters* **95**, 171905 (2009).
- [107] D. M. Leitner, “*Thermal Boundary Conductance and Thermal Rectification in Molecules*”, *The Journal of Physical Chemistry B* **117**, 12820-12828 (2013).
- [108] M. Elzouka and S. Ndao, “*High Temperature Near-Field NanoThermoMechanical Rectification*”, *Scientific Reports* **7**, 44901 (2017).
- [109] N. Li, P. Hänggi, and B. Li, “*Ratcheting heat flux against a thermal bias*”, *EPL (Europhysics Letters)* **84**, 40009 (2008).
- [110] M. Pons, Y. Y. Cui, A. Ruschhaupt, M. A. Simón, and J. G. Muga, “*Local rectification of heat flux*”, *EPL (Europhysics Letters)* **119**, 64001 (2017).
- [111] J. Wang, E. Pereira, and G. Casati, “*Thermal rectification in graded materials*”, *Phys. Rev. E* **86**, 010101 (2012).
- [112] M. Romero-Bastida, J. O. Miranda-Peña, and J. M. López, “*Thermal rectification in mass-graded next-nearest-neighbor Fermi-Pasta-Ulam lattices*”, *Phys. Rev. E* **95**, 032146 (2017).
- [113] N. Yang, N. Li, L. Wang, and B. Li, “*Thermal rectification and negative differential thermal resistance in lattices with mass gradient*”, *Phys. Rev. B* **76**, 020301 (2007).

- [114] M. Romero-Bastida and J. M. Arizmendi-Carvajal, “*Structural influences on thermal rectification of one-dimensional mass-graded lattices*”, *Journal of Physics A: Mathematical and Theoretical* **46**, 115006 (2013).
- [115] R. Dettori, C. Melis, R. Rurali, and L. Colombo, “*Thermal rectification in silicon by a graded distribution of defects*”, *Journal of Applied Physics* **119**, 215102 (2016).
- [116] E. Pereira, “*Graded anharmonic crystals as genuine thermal diodes: Analytical description of rectification and negative differential thermal resistance*”, *Phys. Rev. E* **82**, 040101 (2010).
- [117] E. Pereira, “*Sufficient conditions for thermal rectification in general graded materials*”, *Phys. Rev. E* **83**, 031106 (2011).
- [118] R. R. Ávila and E. Pereira, “*Thermal rectification features: a study starting from local assumptions*”, *Journal of Physics A: Mathematical and Theoretical* **46**, 055002 (2013).
- [119] D. Bagchi, “*Thermal transport in the Fermi-Pasta-Ulam model with long-range interactions*”, *Phys. Rev. E* **95**, 032102 (2017).
- [120] N. Freitas, E. A. Martinez, and J. P. Paz, “*Heat transport through ion crystals*”, *Physica Scripta* **91**, 013007 (2015).
- [121] A. Ruiz, D. Alonso, M. B. Plenio, and A. del Campo, “*Tuning heat transport in trapped-ion chains across a structural phase transition*”, *Phys. Rev. B* **89**, 214305 (2014).
- [122] A. Ruiz-García, J. J. Fernández, and D. Alonso, “*Delocalization and heat transport in multidimensional trapped ion systems*”, *Phys. Rev. E* **99**, 062105 (2019).
- [123] T. Pruttivarasin, M. Ramm, I. Talukdar, A. Kreuter, and H. Häffner, “*Trapped ions in optical lattices for probing oscillator chain models*”, *New Journal of Physics* **13**, 075012 (2011).
- [124] M. Ramm, T. Pruttivarasin, and H. Häffner, “*Energy transport in trapped ion chains*”, *New Journal of Physics* **16**, 063062 (2014).
- [125] J. I. Cirac and P. Zoller, “*A scalable quantum computer with ions in an array of microtraps*”, *Nature* **404**, 579–581 (2000).

- [126] F. N. Krauth, J. Alonso, and J. P. Home, “Optimal electrode geometries for 2-dimensional ion arrays with bi-layer ion traps”, *Journal of Physics B: Atomic, Molecular and Optical Physics* **48**, 015001 (2014).
- [127] R. Schmied, J. H. Wesenberg, and D. Leibfried, “Optimal Surface-Electrode Trap Lattices for Quantum Simulation with Trapped Ions”, *Phys. Rev. Lett.* **102**, 233002 (2009).
- [128] A. Dhar, “Heat transport in low-dimensional systems”, *Advances in Physics* **57**, 457-537 (2008).
- [129] R. Toral and P. Colet, *Stochastic numerical methods: an introduction for students and scientists*. John Wiley & Sons, 2014. <https://onlinelibrary.wiley.com/doi/abs/10.1002/9783527683147.ch6>.
- [130] C. Cohen-Tannoudji, “Atomic motion in laser light”, in *Fundamental systems in quantum optics*, J. Dalibard, J. M. Raimond, and J. Zinn-Justin, eds. Elsevier, 1992.
- [131] H. J. Metcalf and P. van der Straten, “Laser cooling and trapping of atoms”, *J. Opt. Soc. Am. B* **20**, 887–908 (2003).
- [132] L. Chee Kong, “Study of Classical and Quantum Open Systems”, [arXiv:1008.0491](https://arxiv.org/abs/1008.0491).
- [133] E. A. Novikov, “Functionals and the random-force method in turbulence theory”, *Soviet Journal of Experimental and Theoretical Physics* **20**, 1290-1294 (1965).
- [134] P.-W. Ma and S. L. Dudarev, “Langevin spin dynamics”, *Phys. Rev. B* **83**, 134418 (2011).
- [135] G. D. Chiara, G. Landi, A. Hewgill, B. Reid, A. Ferraro, A. J. Roncaglia, and M. Antezza, “Reconciliation of quantum local master equations with thermodynamics”, *New Journal of Physics* **20**, 113024 (2018).
- [136] A. Levy and R. Kosloff, “The local approach to quantum transport may violate the second law of thermodynamics”, *EPL (Europhysics Letters)* **107**, 20004 (2014).
- [137] S. Särkkä and A. Solin, *Applied Stochastic Differential Equations*. Institute of Mathematical Statistics Textbooks. Cambridge University Press, 2019.

- [138] D. F. V. James, “*Quantum dynamics of cold trapped ions with application to quantum computation*”, *Applied Physics B* **66**, 181–190 (1998).
- [139] J. Bezanson, S. Karpinski, V. B. Shah, and A. Edelman, “*Julia: A Fast Dynamic Language for Technical Computing*”, [arXiv:1209.5145](https://arxiv.org/abs/1209.5145).
- [140] J. Bezanson, A. Edelman, S. Karpinski, and V. Shah, “*Julia: A Fresh Approach to Numerical Computing*”, *SIAM Review* **59**, 65-98 (2017).
- [141] C. Rackauckas and Q. Nie, “*Adaptive methods for stochastic differential equations via natural embeddings and rejection sampling with memory*”, *Discrete and Continuous Dynamical Systems Series B* **22**, 2731-2761 (2017).
- [142] F. M. Leupold, *Bang-bang Control of a Trapped-Ion Oscillator*. PhD thesis, ETH Zurich, 2015. <https://doi.org/10.3929/ethz-a-010616440>.
- [143] H.-Y. Lo, *Creation of Squeezed Schrödinger’s Cat States in a Mixed-Species Ion Trap*. PhD thesis, ETH Zurich, 2015.
<https://doi.org/10.3929/ethz-a-010592649>.
- [144] T. Zhang and T. Luo, “*Giant Thermal Rectification from Polyethylene Nanofiber Thermal Diodes*”, *Small* **11**, 4657-4665 (2015).
- [145] M. Enderlein, T. Huber, C. Schneider, and T. Schaetz, “*Single Ions Trapped in a One-Dimensional Optical Lattice*”, *Phys. Rev. Lett.* **109**, 233004 (2012).
- [146] A. Bermudez, M. Bruderer, and M. B. Plenio, “*Controlling and Measuring Quantum Transport of Heat in Trapped-Ion Crystals*”, *Phys. Rev. Lett.* **111**, 040601 (2013).
- [147] C. Schneider, M. Enderlein, T. Huber, and T. Schaetz, “*Optical trapping of an ion*”, *Nature Photonics* **4**, 772–775 (2010).
- [148] A. Riera-Campeny, M. Mehboudi, M. Pons, and A. Sanpera, “*Dynamically induced heat rectification in quantum systems*”, *Phys. Rev. E* **99**, 032126 (2019).
- [149] H. Ma and Z. Tian, “*Significantly High Thermal Rectification in an Asymmetric Polymer Molecule Driven by Diffusive versus Ballistic Transport*”, *Nano Letters* **18**, 43–48 (2018).

- [150] K. M. Reid, H. D. Pandey, and D. M. Leitner, “*Elastic and Inelastic Contributions to Thermal Transport between Chemical Groups and Thermal Rectification in Molecules*”, *The Journal of Physical Chemistry C* **123**, 6256-6264 (2019).
- [151] T. J. Alexander, “*High-heat-flux rectification due to a localized thermal diode*”, *Phys. Rev. E* **101**, 062122 (2020).
- [152] Z. Rieder, J. L. Lebowitz, and E. Lieb, “*Properties of a Harmonic Crystal in a Stationary Nonequilibrium State*”, *Journal of Mathematical Physics* **8**, 1073-1078 (1967).
- [153] A. Casher and J. L. Lebowitz, “*Heat Flow in Regular and Disordered Harmonic Chains*”, *Journal of Mathematical Physics* **12**, 1701-1711 (1971), <https://doi.org/10.1063/1.1665794>.
- [154] M. A. Simón, S. Martínez-Garaot, M. Pons, and J. G. Muga, “*Asymmetric heat transport in ion crystals*”, *Phys. Rev. E* **100**, 032109 (2019).
- [155] D. Leibfried, R. Blatt, C. Monroe, and D. Wineland, “*Quantum dynamics of single trapped ions*”, *Rev. Mod. Phys.* **75**, 281–324 (2003).
- [156] S. Chu, L. Hollberg, J. E. Bjorkholm, A. Cable, and A. Ashkin, “*Three-dimensional viscous confinement and cooling of atoms by resonance radiation pressure*”, *Phys. Rev. Lett.* **55**, 48–51 (1985).
- [157] H. Metcalf and P. Van der Straten, *Laser Cooling and Trapping*. Graduate texts in contemporary physics. Springer-Verlag, New York, 1999.